

# EFFECT OF THERMAL - CYCLING ON THE STRUCTURE, MECHANICAL PROPERTIES AND TEXTURE OF A DUAL - PHASE STEEL

By

MOUSUMI KAR

ME

1991

M

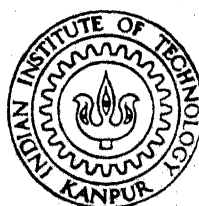
KAR

EFF

TH

ME/1991/M

K143c



DEPARTMENT OF METALLURGICAL ENGINEERING

INDIAN INSTITUTE OF TECHNOLOGY KANPUR

JANUARY, 1991

# **EFFECT OF THERMAL - CYCLING ON THE STRUCTURE, MECHANICAL PROPERTIES AND TEXTURE OF A DUAL - PHASE STEEL**

*A Thesis Submitted*  
In Partial Fulfilment of the Requirements  
for the Degree of  
MASTER OF TECHNOLOGY

By  
MOUSUMI KAR

*to the*  
DEPARTMENT OF METALLURGICAL ENGINEERING  
INDIAN INSTITUTE OF TECHNOLOGY KANPUR  
JANUARY, 1991

TH  
669.96142  
K143e

1 2 APR 1991

CENTRAL LIBRARY  
I. I. T., KANPUR

Acc. No. A. 110760

ME-1881-M-KAR-EFF

*Dedicated to  
My Parents*



Certificate

Certified that the work reported in this thesis entitled 'Effect of Thermal-Cycling On the Structure, Mechanical Properties and Texture of a Dual-Phase Steel' by Ms. Mousumi Kar has been carried out under my supervision and has not been submitted elsewhere for the award of a degree.



( R. K. Ray )  
Professor

January, 1991.

Department of Metallurgical Engineering  
Indian Institute of Technology  
Kanpur.

### Acknowledgements

I take this opportunity to express my sincere gratitude and indebtedness to my supervisor, Professor R.K. Ray for brilliant guidance and active co-operation throughout the course of this work.

I would like to thank M/s. K.P. Mukherjee, H.C. Srivastava, P.K. Paul, U.S. Lal and B.K. Jain for assisting me at various stages of this work. Special thanks are due to Mr. A.K. Ganguli for tracing the figures and Mr. R.N. Srivastava for the excellent typing.

My acknowledgements are also due to Ms. Martha Patricia Butron-Guillen for drawing the pole-figures and O.D.F.'s presented in this thesis.

## SYNOPSIS

Studies have been carried out to find the effect of thermal-cycling on the structure, mechanical properties and texture of a dual-phase steel. For this purpose, a C-Mn-Si-V dual-phase steel was melted, forged and homogenised, followed by 60% deformation at room temperature. Some of the cold-deformed materials were given intercritical annealing at 810°C for 5 minutes and 30 minutes to generate dual-phase structures. The two dual-phase structures and the cold-worked materials were then thermally cycled using two different routes - Type-I and Type-II. Crystallographic textures of the cold-deformed and thermally-cycled materials were measured using the conventional pole figure as well as the orientation distribution function (O.D.F.) methods. In addition, structural characterization of the initial and thermally cycled steel samples was carried out using optical and scanning electron microscopy. Limited mechanical property measurements were also done.

The best grain refinement has been obtained by subjecting the dual-phase structure (produced by annealing at 810°C for 5 minutes) to the Type-I cycle. The optimum number of cycles has been found to be ten. The U.T.S. and percentage elongations are found to be not much different for all the thermally cycled materials. Increasing the number of cycles leads to a higher 'n'-value in case of Type-I thermal-cycling treatment. The general intensity of the texture of the

cold-worked materials is low and is found to consist of two weak components  $\{111\} \langle 112 \rangle$  and  $\{111\} \langle 110 \rangle$ . The textures of the cold-worked and thermally cycled materials are found to be remarkably similar and this suggests that recrystallization during thermal-cycling takes place by an in-situ mechanism. The materials, on thermal-cycling by either of the two processes, seem to possess some kind of texture memory. The results have been critically analysed and an attempt has been made to explain the various phenomena.

## Contents

	Page
Chapter I      Introduction	1
Chapter II     Literature Review	5
2.1   Historical Development	5
2.2   Composition and Heat Treatment of Dual-Phase Steels	8
2.2.1   Typical Compositions	8
2.2.2   Selection of Alloying Elements	8
2.2.3   Heat Treatment Cycles	11
2.3   Structure of Dual-Phase Steels	14
2.3.1   Distribution of Phases	14
2.3.2   Effect of Heat Treatment on Micro-structure	15
2.4   Mechanical Properties of Dual-Phase Steels	16
2.4.1   Typical Stress-Strain Curves for Dual-Phase Steels	16
2.4.2   Strength and Ductility	17
2.4.3   Deformation Behaviour	19
2.4.4   Sheet Formability	20
2.5   Thermal-Cycling of Dual-Phase Steels	23
2.6   Representation of Texture	24
2.7   Textures in Dual-Phase Steels	25
Chapter III    Experimental Procedure	33
3.1   Materials and Their Preparation	33
3.2   Heat Treatment, Cold-Rolling and Production of the Dual-Phase Structure	34
3.3   Thermal-Cycling of the Cold-Rolled as well as Dual-Phase Structures	35
3.4   Tensile Testing	37
3.5   Optical Metallography	40
3.5.1   Specimen Preparation and Examination	40
3.5.2   Quantitative Metallography	41
3.6   Scanning Electron Microscopy	42
3.7   Hardness Measurements	42
3.7.1   Macrohardness Measurements	42
3.7.2   Microhardness Measurements	42
3.8   Determination of Texture	43
Chapter IV    Experimental Results	47
4.1   Microstructures	47
4.1.1   Microstructures of As-received and Homogeneous Materials	47
4.1.2   Microstructures of Initial Starting Materials	47

4.1.3	Microstructures of Thermally Cycled Materials	49
4.1.4	Results of Grain-Size Measurements	56
4.2	Mechanical Properties	60
4.2.1	Hardness and Microhardness	60
4.2.2	Tensile Properties	63
4.2.3	Study of Fractured Surfaces	69
4.3	Results of Texture Analysis	76
Chapter V	Discussions	95
Chapter VI	Conclusions	102
References		104

## CHAPTER I

### Introduction

Over the past few decades, the automobile manufacturers' target has been weight saving and energy conservation. This has resulted in the development of a number of routes to manufacture low-cost, high strength steels with good formability.

Earlier, plain, low-carbon steels cold-rolled to thicknesses upto 2 mm or hot-rolled to thicker gauges were used. Nowadays, with the use of higher strength steels, the usable sheet metal thicknesses could be reduced and there would be significant reduction in the weight of the automobile.

In order to meet these requirements the effort previously was to develop high strength steels, like microalloyed controlled-rolled steels, high strength low alloy i.e. (H.S.L.A.) steels or some other variety. But these steels suffered from two major problems - they lacked dynamic stiffness and had a poor formability. Among these, the H.S.L.A. steels have a high yield strength and in spite of their not so good formability characteristics, they are used in significant quantities in the current models of many automobiles. The problem of poor formability of H.S.L.A. steels has recently been overcome by the use of dual-phase steels, discovered around 1975 [1].

The dual-phase steels consist essentially of about 80-90% low C ferrite and 10-20% of a hard second phase, mostly martensite, dispersed in the ferritic matrix. Little amounts of retained austenite and some low carbon bainite may also be

present as minor constituents. Compared to the conventional A.S.L.N. steels, the dual-phase steels were expected to have better formability characteristics due to their low initial yield strength, continuous yielding behaviour, high work-hardening rate at the early stages of straining and a rather large total elongation before fracture.

The dual-phase structure in steels may be produced by annealing either hot or cold-rolled strips at a temperature in the two phase ( $\alpha + \gamma$ ) region of the Fe-Fe<sub>3</sub>C equilibrium diagram, followed by cooling at a rate which ensures that the  $\gamma$  phase transforms to martensite. The one most important property of dual-phase steels that has been found to be inferior to that of conventional steels used in the automotive industry is the deep drawability. The  $\bar{r}$  values (which give an indication of the deep drawability characteristics) of dual-phase steels produced by intercritical annealing, have been found to be around 1.0 whereas for some killed steels it can be as high as 1.6 to 1.8 or even more.

The aim of the present investigation is to develop dual-phase steels with improved  $\bar{r}$  values so that the superior mechanical properties of these steels such as high strength and large uniform and total elongation can be taken advantage of. It is known that the  $\bar{r}$  values in a sheet steel can always be associated with the presence of a strong {111} fibre texture in the material [2]. Hence, attainment of high  $\bar{r}$  values in sheet steels can ultimately be linked to the ease of nucleation and growth of {111} oriented grains in the sheet material. In the



past a number of dual-phase steels have been thermomechanically processed and their microstructures and textures developed through cold-work and subsequent recrystallization [3]. This has led to some improvement of the  $\{111\}$  texture and hence improvement of  $\bar{r}$  values. However, this improvement is not very significant and, therefore, other ways and means need to be looked into, in order to produce even better results. It has been quite well known [4] that thermal cycling of steels produces a finer grain size leading to improved mechanical properties. It can be assumed that if the starting material is in the cold-deformed condition, subsequent thermal cycling may produce even finer grain size than otherwise obtainable. In addition, thermal cycling, in this case, is also expected to have an important effect on the texture of the starting cold-rolled material. Since some amount of  $\{111\}$  texture is always produced in steels by cold-rolling, it may be worthwhile to study the effect of thermal cycling on these steels from the point of view of producing desirable textures in them. It was with this idea that the present work was undertaken.

For this purpose a C-Mn-Si-V dual phase steel was melted, forged and homogenised, followed by 60% deformation at room temperature. Some of the cold-deformed materials were given intercritical annealing at  $810^{\circ}\text{C}$  for 5 minutes and 30 minutes to generate dual-phase structures. The two dual-phase structures and the cold-worked materials were then thermally cycled using two different routes. Crystallographic textures of the cold-deformed and thermally cycled materials were measured

using the conventional pole figure as well as the orientation distribution function (O.D.F.) methods. In addition, structural characterization of the initial and thermally cycled steel samples was carried out using optical and scanning electron microscopy. Limited mechanical property measurements were also done.

## CHAPTER II

### Literature Review

#### 2.1 Historical Development

Performance requirements resulting from the car manufacturer's targets of weight saving and energy conservation resulted in a number of routes to develop low-cost, high-strength steels with good formability. Previously, high strength steels, such as microalloyed controlled-rolled, high strength low alloy i.e. (H.S.L.A.) steels [1, 5, 6] or some other variety were developed to cater the above requirements. But these high strength steels suffered from two major problems of dynamic stiffness and poor formability and so the formability problem of the H.S.L.A. steels was tried to be overcome by the development of 'dual-phase' steels. The major constituents of dual-phase steels are 80-90% low carbon ferrite and 10-20% of a hard second phase, mostly martensite while the minor constituents that may also be present are little amounts of retained austenite and some low-carbon bainite. The characteristic properties of the dual-phase steels are continuous yielding behaviour, relatively low initial flow stress, a high ultimate tensile strength and very rapid and sustained work-hardening, giving rise to high uniform elongation. Hot-rolled or cold-rolled steel strips when annealed at temperatures in the two-phase ( $\alpha + \gamma$ ) region on the Fe-C equilibrium diagram, followed by cooling at rates which ensure that the remaining  $\gamma$ -phase transforms to martensite, give a dual-phase structure. Hayami and Furukawa [1], were the first to demonstrate superior

formability properties of the dual-phase steels by performing deep drawing tests. At this time several parallel developments [5-10] produced D.P. microstructures in steels where manganese is the main element retarding diffusion-controlled transformation of austenite. Silicon and chromium were found to control hardenability so that addition of silicon, chromium and manganese produced dual-phase structures by box-annealing. With the idea of restricting ferrite grain growth and having sufficient hardenability of austenite formed during intercritical annealing, the controlled-rolled microalloyed H.S.L.A. steels have been considered to be suitable starting materials in producing dual-phase steels. Rashid [9, 11] found that the required hardenability was furnished by adding a small concentration of vanadium while Morrow and co-workers [10-12] observed the same effect with the addition of a very small amount of molybdenum. Demonstration, that a high strength dual-phase steel with a total elongation as high as 30% can be obtained in GM-980X-V [9, 11] containing very small amount of V in addition to substantial amounts of the solution strengtheners like Mn (1.5%) and Si (0.5%) was demonstrated by Rashid [11]. With similar concentrations of Mn and Si, Morrow and co-workers successfully developed micro-alloyed dual-phase steels containing Mo. But it has been found that steels containing V have superior mechanical properties as compared to those containing Nb and/or Mo [10]. High work-hardening rate, good press formability and spot weldability have been reported by Matsuoka and Yamamori [13] in a manganese-bearing steel with similar dual-phase properties. The cyclic austenitisation technique of Grange [14] for grain refinement

was used by Koo and Thomas [15-17] to produce dual-phase properties in a few Mn-Si-Cr steels. The dependence of the strength of dual-phase steels on the ferrite grain size and the volume fraction of martensite was found by Davies [18-22] while studying the properties of dual-phase structures in a variety of Fe-Mn-C alloys.

Alternatively, dual-phase steels can be produced by controlling the cooling rate after hot rolling in the mills. But the elements added to control hardenability need to be more selective in their effects. Coldren and Tither [23] have considered the production of dual-phase structure in a steel containing 0.6% Cr, 0.4% Mo, 1% C by hot rolling and subsequent cooling. By controlling the coiling temperature so that it falls within a specific region called the "coil window" [Figure 2.1] the austenite transforms to tempered martensite at a very slow cooling rate and the product is found to have excellent tensile strength and good formability. The total elongation is not so large as that of the intercritically annealed dual-phase steels. By a similar development in Japan [24], a low carbon steel with 0.4% Si and 1.4% Mn has been coiled at a very low temperature (below  $M_s$  temperature of the austenite) to transform the austenite before coiling. This is known as dual-phase rolling and gives rise to inferior tensile strength properties when compared to that described by Coldren and Tither [23]. But the total elongation remains same.

## 2.1 Composition and Heat Treatment of Dual-Phase Steels

### 2.2.1 Typical Compositions

The composition of all dual-phase steels is based primarily on low carbon and low alloy content. Formation of ferrite-carbide transformation products during cooling from ( $\alpha + \gamma$ ) intercritical range, due to lack of hardenability can be overcome by minor addition of vanadium, niobium, chromium, molybdenum, etc. Aluminium-killed steels are commonly used in practice, although the Japanese steels high in silicon are deoxidized with silicon. All dual-phase steels are given a sulphide particle shape-control treatment usually with rare earths and zirconium and they maintain a low sulphur content. Typical compositions of some dual-phase steels either in production or at an advanced stage of development are given in Table 2.1.

### 2.2.2 Selection of Alloying Elements

Dual-phase steels have superior properties from their essential structural features. Dispersion of a strong martensite in a high strength, highly ductile ferrite matrix gives rise to enhanced ductility at a given tensile strength. Many combinations of alloying elements such as Mn, Si, C, Mo and V can be added to low carbon iron to obtain austenite with desired hardenability [25, 26], for transformation to martensite even at a mild cooling rate. The selection of alloying elements depends on the properties required and also the available facilities. The combination of various alloying elements can give rise to a family of dual-phase steels whose strength depends on the strength of both the phases present. Besides increasing the

Table 2.1  
Compositions of some common dual-phase steels

	Composition, wt. %							
	C	Mn	Si	Ni	Cr	Mo	V	Nb
A. Carbon-manganese series	0.01	1.45	-	-	-	-	-	-
	0.06	0.33	-	-	-	-	-	-
	0.052	0.90	-	-	-	-	-	-
	0.11	0.78	-	-	-	-	-	-
B. Carbon-silicon series	0.10	-	2.00	-	-	-	-	-
C. Carbon-manganese-silicon series	0.15	1.50	0.01	-	-	-	-	-
	0.22	1.55	0.01	-	-	-	-	-
	0.10	1.45	1.20	-	-	-	-	-
	0.06	1.47	0.23	-	-	-	-	-
	0.12	1.47	0.24	-	-	-	-	-
	0.16	1.53	0.24	-	-	-	-	-
	0.20	1.53	0.25	-	-	-	-	-
	0.29	1.51	0.24	-	-	-	-	-
D. Carbon-manganese-silicon-vanadium series	0.21	2.00	1.03	-	-	-	0.20	-
	0.10	1.45	1.20	-	-	-	0.15	-
	0.10	1.44	0.49	-	-	-	0.075	-
E. Carbon-manganese-silicon-nickel-chromium-vanadium series	0.072	1.26	0.30	0.02	0.02	-	0.08	-
	0.11	1.29	0.29	0.02	0.03	-	0.065	-
F. Carbon-manganese-silicon-chromium-molybdenum series	0.062	1.19	0.02	-	0.49	0.03	-	-
	0.07	0.90	1.20	-	0.57	0.29	-	-

hardenability of austenite, silicon reduces the interstitial carbon content of ferrite which ultimately leads to a cleaner and more ductile ferrite. This has been shown by the results of some silicon-containing steels [27]. Si and P are very effective in strengthening ferrite by substitutional solute elements [28]. Strengthening by silicon and manganese resulted in the best combination of strength and ductility as shown by Masui and Takechi [29].

In order to produce lath instead of twinned martensite to avoid brittleness in the product [30], the carbon content has to be kept maintained at  $\approx 0.3$  wt %. For this the initial alloy composition and the volume percent martensite have to be controlled as this is a more or less accepted principle of the duplex ferrite-martensite alloy development. However, while choosing a favourable overall composition the effect of substitutional elements should be kept in mind. Though the primary function of Mn and other alloying elements like V, Mo, Cr, etc. is to increase the hardenability of austenite, Si and sometimes manganese are added to improve the drawing properties of the ferrite. These alloying elements partition to a significant extent in the austenite. Due to higher equilibrium concentration of V in austenite than Nb, many investigators [10, 11] have considered vanadium addition to be much more effective than Nb in this respect. Severe chemical heterogeneity within individual austenite islands may arise due to very slow diffusion of all substitutional elements at the intercritical annealing temperature giving rise to lack of equilibrium partitioning [31]. Hence severe carbon-concentration gradients may also be set up



within individual austenite islands as the local equilibrium concentration of carbon is determined by the type and concentration of substitutional elements present. This type of segregation can lead to formation of a mixture of transformation products within a single island which can be averted to a certain extent by annealing the steel in the single  $\gamma$ -phase before cooling to the intercritical annealing temperature [32].

Chromium retards the process of bainite formation besides increasing the hardenability. According to Tanaka et al [33] Cr is the most favourable alloying element for dual-phase steel production since it decreases the dissolved carbon content by promoting partition of carbon between austenite and pearlite. Cr does not cause solid solution hardening in ferrite [34]. Mn has an effect similar to that of Cr except that it causes solid-solution hardening of ferrite. Molybdenum also increases the hardenability of austenite. As it is a ferrite former, it does not decrease carbon solubility in ferrite and moreover it causes a large solid-solution hardening effect [35]. There is precipitation of carbonitrides and grain refinement with the addition of niobium to the steel. This precipitation in turn leads to the formation of a substructure in the ferrite and as a consequence the tensile strength is increased. To produce a simple, economical steel with favourable structure and required properties the desirability of various alloying elements must be properly assessed.

### 2.2.3 Heat Treatment Cycles

By cooling from the intercritical annealing temperature

at any rate between batch annealing and water quenching, dual-phase steels can be produced. The cooling rate depends upon the chemical composition of the steel. Dual-phase steels with a variety of chemical compositions and considerably varying physical properties have been developed by adding small quantities of alloying elements in order to decrease the cooling rate. The heat treatment cycle is comprised of the starting structure prior to intercritical annealing, the annealing temperature and the cooling rate and the dual-phase microstructure is a function of these variables. The different types of heat-treatment cycles used for the production of dual-phase structures may be classified as:

- (i) Intermediate annealing (I.A.)
- (ii) Intermediate normalising (I.N.)
- (iii) Intermediate quenching (I.Q.)
- (iv) Step quenching (S.Q.)
- (v) Continuous annealing (C.A.).

In intermediate annealing and intermediate normalising cycles, steels containing coarse and fine ferrite and pearlite respectively, are used for intercritical annealing. If the structure of the steel before intercritical annealing is fully martensitic, the process then used is intermediate quenching. In step quenching, the steel is transferred from the austenitisation temperature to the intercritical annealing temperature. In all heat treatment cycles, the steel is soaked at the intercritical annealing temperature for a specified length of time and then cooled at a suitable rate to the room temperature.

In continuous annealing, dual-phase structures in steels are obtained in the as hot-rolled condition. The steel sheets are coiled after adequate hot rolling and the cooling rate during coiling is controlled in order to get the required dual-phase structures. The coiling conditions have been simulated by many investigators [23, 32, 36] in order to get a dual-phase structure similar to that obtainable on continuous annealing.

The intercritical annealing has to be carried out at a temperature which is between  $Ae_3$  (upper limit of the critical range) and  $Ae_1$  (beginning of transformation range), regardless of the heat-treatment cycle. Since equilibrium conditions are rarely maintained in steels of commercial purity, the temperatures of practical utility are  $AC_1$  and  $AC_3$ . These critical temperatures can be related to the chemical composition of the steel as follows [37]:

$$AC_1 = 723 - 10.7 \text{ Mn} - 16.9 \text{ Ni} + 29.1 \text{ Si} + 16.9 \text{ Cr} + 290 \text{ As} \\ + 6.38 \text{ W}$$

$$AC_3 = 910 - 203 \sqrt{C} - 15.2 \text{ Ni} + 44.7 \text{ Si} + 104 \text{ V} + 31.5 \text{ Mo} \\ + 13.1 \text{ W}$$

The annealing temperature in the  $(\alpha + \gamma)$  phase field controls the volume percent of austenite and establishes the austenitic carbon content, thus affecting the hardenability of austenite pools. The hardenability of austenite [38-40] during intercritical annealing decreases with increasing annealing temperature.

## 2.3 Structure of Dual-Phase Steels

### 2.3.1 Distribution of Phases

The distribution and morphology of constituent phases in dual-phase steels is pronouncedly affected by the various heat treatments and processing schedules [38]. Thus, intermediate quenching results in a distribution of fine fibrous martensite in the ferrite matrix, while intermediate annealing or intermediate normalizing gives rise to a distribution of fine globular martensite along the ferrite boundaries. In step quenching the resulting structure is of coarse martensite surrounded by a ferrite matrix. Evidently the dual-phase microstructure depends on the prior austenite grain size. Due to this the distribution of phases tends to be coarser during step quenching than those obtained from original martensitic and hypoeutectoid structures as the initial grain size is coarser there.

The ferrite grain size in dual-phase steels is very fine ( $\sim 10$   $\mu\text{m}$  dia) as the ferrite is got by intercritical annealing of either cold-rolled sheets for very short times or micro-allyed controlled-rolled sheets for somewhat longer times. Because most of the dispersed carbides present in the as-rolled pearlitic steel dissolve readily on intercritical annealing, the ferrite is remarkably clean [7, 9, 10, 11, 12] containing insignificant amounts of fine carbides. Transmission electron microscopy of ferrite usually reveals high density of dislocations, particularly in the vicinity of the martensite islands. On cooling from the intercritical annealing temperature, usually

some ferrite separates out from the austenite producing an extra carbon concentration in the then untransformed austenite. The new ferrite forms epitaxially on the old ferrite and has very little or no partitioning of alloying elements except carbon, during separation. The extent of ferrite separation is greatly influenced by the balance between ferrite stabilisers (e.g. Si) and austenite stabilisers (e.g. Mn, C, V and Nb). Further cooling transforms the remaining austenite to dislocated (lath) martensite or to twinned (acicular) martensite depending on whether the carbon concentration is below or above about 0.35%. This limiting carbon content is greatly influenced by the presence of alloying elements.

### 2.3.2 Effect of Heat-Treatment on Microstructure

Literature survey reveals that hardly any systematic study has yet been made to determine the effect of heat-treatment on the fine structure of dual-phase steels. Some T.E.M. studies done on different intercritically-annealed dual-phase steels have shown that the fine structure is characterized by regions of high dislocation density close to the ferrite-martensite interfaces and regions of low dislocation density in ferrite grain interiors [33].

T.E.M. studies [38] on dual-phase structures produced in a Fe-2 Si-0.1 C alloy by intermediate quenching, intermediate annealing and step quenching, have shown no remarkable difference in their structure. The substructure of martensite was found to be similar in all cases. The ferrite regions showed formation of subgrains in the intermediate quenched and intercritically annealed structures but not in the step quenched structure.

Earlier investigators have reported [36, 39, 40] that small quantities (~5%) of retained austenite may be present in slowly cooled dual-phase steels, especially those containing carbide forming elements. The retained austenite stabilised at room temperature is believed to exist in the form of small equiaxed islands rather than thin films as typically observed in lath martensite structures [8].

## 2.4 Mechanical Properties of Dual-Phase Steels

### 2.4.1 Typical Stress-Strain Curves for Dual-Phase Steels

The characteristics of dual-phase steels which distinguish them from plain carbon and H.S.L.A. steels are:

- (i) low yield strength
- (ii) continuous yielding
- (iii) high initial work hardening
- and (iv) large uniform and total elongations.

Figure 2.2 [41] shows typical stress-strain curves for plain-carbon steel, a high strength low alloy SAE 980X steel and an intercritically annealed dual-phase SAE 980X steel.

The  $\log \sigma$  vs.  $\log \epsilon$  plots show a linear behaviour and from the slope of this curve the strain hardening exponent 'n' can be determined for low carbon and micro-alloyed steels. The true stress  $\sigma$  and the true strain  $\epsilon$  obey the power law of Hollomon [42]:

$$\sigma = K\epsilon^n$$

where n is the work-hardening exponent and K is the strengthening co-efficient. Many dual-phase steels have also been found

to behave similarly [41, 43]. But in some dual phase steels the  $\ln \sigma$  vs.  $\ln \epsilon$  curve deviates from linearity indicating that the power law relation may not be valid there [44]. In such cases the work hardening exponent is evaluated at any specified strain level from the slope of the curve at that point [9]. The analysis suggested by Crussard [45] and Jaoult [46] is found more suitable than the Hollomon's analysis for alloys exhibiting multiple 'n' behaviour. In these cases the Ludwik equation is used [47]:

$$\sigma = \sigma_y + K\epsilon^n$$

where  $\sigma_y$  is the yield strength and  $K$  and  $n$  are constants. According to the Jaoult-Crussard analysis, the Ludwik equation was re-written as:

$$\ln\left(\frac{d\sigma}{d\epsilon}\right) = \ln(Kn) + (n-1) \ln \epsilon$$

The plot of  $\ln\left(\frac{d\sigma}{d\epsilon}\right)$  versus  $\ln \epsilon$  differentiates several distinct stages of strain-hardening during deformation, particularly at low strains.

#### 2.4.2 Strength and Ductility

The two important mechanical properties, namely, high tensile strength (roughly proportional to both fatigue and crush resistance) and large total elongation (may be taken as a measure of formability) must be essentially possessed by high strength steels [48] to be used for making automobile components. The yield strength is relatively unimportant from an engineering or application viewpoint. Figure 2.3 [49] shows a plot of total elongation as a function of ultimate tensile strength for some

commercially available high strength steels. The much superior performance of the dual-phase steels as compared to the conventional high strength steels is quite apparent from this figure.

Nowadays, it is generally agreed that the strength of dual-phase steels is linearly proportional to the volume fraction of martensite present in the structure. This is supported by Figure 2.4 [20] which shows the variation of the 0.2% flow stress and tensile strength as a function of percent martensite for a series of Fe-Mn-C dual-phase steels. It also appears that the strength of these dual-phase steels is independent of the carbon content of the martensite.

It has been found that the tensile strength of dual-phase steels increases with the increase in the strength and hardness of the constituent ferrite phase. It has been suggested that the ferrite should be very fine grained ( $\sim 3 \mu$  size), free of fine precipitates and strengthened by substitutional alloying elements (e.g. Si, which do not have much effect on ductility) for the steel to have optimum mechanical properties.

Studies [20, 21] have shown that for dual-phase steels with upto about 30% martensite, the ductility of the composite is sensitive to the strength and ductility of the matrix. So the ferrite should be as strong as possible and maintain a high ductility at the same time. But common knowledge tells us that higher the strength of the ferrite, the lower will be its ductility. So the only way to get a good combination of strength and ductility is by adding some substitutional solute atoms which may increase the strength of the ferrite proportionally more than the decrement they cause in ductility values [21].



Superior strength-ductility combinations are associated with a superior work-hardening behaviour [49]. The significantly high work-hardening rates at all strains in case of dual-phase steels is obvious from the plot of the work-hardening rate as a function of strain for a number of conventional and dual-phase steels (Figure 2.5). Thus to understand the superior strength and ductility behaviour of dual-phase steels, a study of the work-hardening mechanisms of these steels is essential.

### 2.4.3 Deformation Behaviour

The deformation behaviour in dual-phase steels has been tried to be explained by using models [50] developed for composites. The dual-phase steels were considered to be composites of a strong martensitic phase and a soft and ductile ferrite phase. The two limiting models available for two-phase composites and applicable for dual-phase steels are equal strain [51] and equal stress [52] models. When the dual-phase steel contains a hard phase distributed in a soft matrix, an intermediate situation seems to be valid [53]. But, all these models completely overlook the size, shape, number and distribution of martensitic islands which affect the deformation behaviour of dual-phase steels. In order to develop a realistic model which will explain the mechanical and mechanical properties of these steels correctly, these aspects should be considered.

Fracture behaviour of dual-phase steels has also been studied by a few workers [54, 55] and a number of mechanisms thus proposed in case of tensile and other kinds of loads

applied. It was found that no single fracture mechanism is operative and the following mechanisms could be operating simultaneously. These are: (i) decohesion at ferrite-martensite interface, (ii) fracture of martensite, (iii) crack formation in ferrite with localised high stresses, and (iv) void formation around inclusions. It has been suggested [56] that the tensile load applied is transferred to the harder martensitic phase via the softer ferrite and thus the hard phase is subjected to excess load. During later stages decohesion of the martensite-ferrite interfaces occur and nearing the end of the uniform elongation stage, martensitic areas with sufficient stress build up, fracture. Simultaneously, voids may be formed around the larger inclusions due to tensile stress and the large voids may be linked up by microvoids initiated at smaller inclusions. As a result, necking takes place due to very fast decrease of the cross-sectional area of the specimen. When such a situation is prevalent, the ruptured martensitic regions may act as sharp notches and may lead to cleavage cracks in the ferrite which ultimately cause cleavage fracture of the ferritic grains.

#### 2.4.4 Sheet Formability

The mechanical properties, particularly the ability to distribute strain affects the formability of sheet metals, mostly. The formability is characterised by the dimensionless parameter  $\frac{1}{\sigma} \frac{d\sigma}{d\epsilon}$ , where  $\sigma$  is the current value of the flow stress and  $\frac{d\sigma}{d\epsilon}$  is the current rate of work-hardening. As the strain increases, this parameter decreases in successive stages and with this the material becomes less able to spread the strain

to less deformed parts. Hence ductile fracture occurs by void growth and coalescence as the strain concentrates into a diminishing volume [43]. Thus, the property requirements strongly influencing sheet formability are:

- (a) work-hardening behaviour which may be estimated from the work-hardening co-efficient,
- (b) plastic anisotropy, and
- (c) strain-rate sensitivity, ductility and also the temperature of forming.

To improve or control the sheet formability, all metallurgical factors influencing these properties can be taken advantage of.

To know the degree to which a material can distribute strain or work-harden effectively, the work-hardening co-efficient 'n' is used. High 'n'-value materials are able to sustain more work-hardening and prevent localized strain concentration within them.

'Normal anisotropy' can be defined as the property of having different strengths in the plane of the sheet and normal to the sheet. While 'planar anisotropy' is the property of having different strengths along different directions on the plane of the sheet. The normal and planar anisotropy are usually combined together as 'Lankford anisotropy'. The plastic strain ratio ('r'), originally suggested by Lankford characterises the directionality properties of materials. This 'r' is given as:

$$r = \frac{\epsilon_t}{\epsilon_n} = \frac{\ln \frac{w_0}{w_f}}{\ln \frac{t_0}{t_f}}$$

where  $\epsilon_w$  and  $\epsilon_t$  are the true strains in the width and thickness directions,  $w_0$  and  $w_f$  are the initial and final widths and  $t_0$  and  $t_f$  are the initial and final thicknesses. Since the strengths in the plane of the sheet are different along different directions, an average strain ratio ( $\bar{r}$ ) can be determined by averaging the strains measured parallel ( $r_0$ ), transverse ( $r_{90}$ ) and at  $45^\circ$  ( $r_{45}$ ) to the rolling direction i.e.,

$$\bar{r} = \frac{r_0 + 2r_{45} + r_{90}}{4}$$

Generally  $r_0$ ,  $r_{45}$  and  $r_{90}$  have significantly different values for a given sheet material and thus 'ears' are formed in thin sheets. Another parameter  $r$  can be defined as:

$$r = \frac{r_0 + r_{90} - 2r_{45}}{2}$$

For fully isotropic sheet materials  $\bar{r} = 1$  and  $r = 0$ . When  $\bar{r} > 1$ , the average strength in the plane of the sheet is lower than that across the thickness and vice versa for  $\bar{r} < 1$ . Thus sheet steels with very high  $\bar{r}$  values are highly resistant to uniform thinning and desirable for deep-drawing purposes. According to Whiteley et al [57, 58], the higher the  $\bar{r}$  value of the material, the deeper is the draw.

Although the  $r$  value of 300M is excellent in dual-phase steels, the deep drawability tends to be less impressive due to the following reasons: (i) It is difficult to develop appropriate crystallographic texture necessary for a high normal anisotropy (high  $\bar{r}$  value) due to high alloy additions and fine carbide dispersions present. (ii) Even when the texture is

suitable, the hard martensitic phase decreases the  $\bar{I}$  value [59, 60]. The decrease in the  $\bar{I}$  value is dependent on the volume fraction and proximity of martensitic islands according to Murihara et al [61], and Hutchinson [84] showed that both normal and planar constituents are reduced by the presence of martensitic constituents. The reduction in the latter case is due to the superimposition of an isotropic hardening component on an anisotropic matrix.

### 3.5 Thermal Cycling of Dual-Phase Steels

The strength of plain low carbon steels can be increased effectively by increasing the carbon content. The two major disadvantages associated with this are inadequate ductility and weldability of the resulting material. In a ferrite-pearlite steel, it has been found that the most important factor controlling the strength and ductility is grain size. Ultrafine grains can be obtained by repeated thermal cycles of rapid austenitizing and cooling [4] as proposed by Grange [4].

Koo and Thomas [15] applied a non-standard heat treatment process consisting of alternate thermal cycling in the  $\gamma$ -range and the phase ( $\alpha + \gamma$ ) range with liquid quenching in order to produce a microstructure like a refined mixture of martensite and ferrite. The material was then subjected to mechanical working. These multiple heat treatments were found to give better uniform elongation, yield strength and uniform elongation than are achieved by conventional treatments on ferrite-pearlite steels and also a better grain size refinement as compared with that from conventional heat treatments. The beneficial effects

of initial grain size, dislocation substructure and retained austenite were ideally combined by this heat treatment and the ferrite grains were effectively strengthened by the ultrafine subgrains in addition.

L'yachenko and co-workers [62] found that repeated heating and cooling in the temperature range between  $AC_1$  and  $AC_3$  causes a change in the ratio of the amounts of the phases in steel quenched after thermal cycling as compared with heating and cooling only once. As the number of cycles is increased, the quantity of martensite decreases, the intent of this increasing with heating into the upper part of the intercritical temperature range. One of the reasons for the reduction in martensite content is a decrease in austenite stability. Fine grained steels with a small initial grain size therefore causes no marked refinement of the grain structure. Maximum grain refinement was obtained as a result of thermal cycling with the following schedule:

$$AC_3 - (10-20^\circ C \rightleftharpoons 20^\circ C.$$

## 2.6 Representation of Textures

Texture or preferred orientation with respect to some crystallographic planes and directions exists to some extent in many polycrystalline materials. The mechanical and physical properties in addition to others are affected by this texture. The usual representation of textures are by pole figures which are simple stereographic projections showing distribution of particular crystallographic directions in a group of grains constituting the metal. The reference directions in

20

pole figures are taken as some well-defined directions. The rolling direction (RD), transverse direction (TD) and normal direction (ND) are the three reference directions in case of rolled metals. The procedure for representing texture by pole-figures is illustrated in Figures 2.6(a) to (e). The sheet is made to sit at the centre of the stereographic sphere and the RD, TD and ND coincide with the X, Y and Z axes (Figure 2.6a). The orientation of a grain, say (100), can be then represented easily by plotting the three (100) poles in a pole-figure. All the poles concerned are normally projected on to the equatorial plane producing a stereographic projection (Figure 2.6b). When the poles are uniformly distributed over the area of projection then no texture is said to exist and the specimen is said to possess a 'random' texture. If the poles tend to cluster together in certain areas of the pole figure, they are said to produce a texture (Figure 2.6c). Usually the data is collected from many grains simultaneously and are represented in the form of density contours on the pole figure (Figure 2.6d-e).

In texture work the pole figures are measured by X-ray diffraction. Two methods, the transmission method due to Decker, Asp and Harker [63] and back reflection method by Schulz [64] are available. Quantitative measurements are not possible from pole figures as they specify only two independent variables while there are three degrees of freedom in the general orientation. The pole figures are thus only projections of the three-dimensional orientation distribution function (O.D.F.) which describes the orientation density in a three-

dimensional orientation space formed by the Euler angles  $\phi_1$ ,  $\phi$  and  $\phi_2$ , giving the rotation of the crystallographic axes into the specimen co-ordinate system. Figure 2.6 shows the transformation of the sample frame S to the crystallite frame C using Euler angles, by the following three steps:

- (i) A first rotation  $\phi_1$  around the RD transforms the TD and the RD into the new directions TD' and RD' respectively.  $\phi_1$  must have such a value that RD' is perpendicular to the plane formed by RD and [001].
- (ii) A second rotation  $\phi$  around the new direction RD' has such a value that it transforms RD into [001] (= RD') and TD' into TL'.
- (iii) A third rotation  $\phi_2$  around [001] (= RD') transforms RD' into [100] and TL' into [010].

The O.D.F. is then mostly plotted by contour lines in a series of sections through the Euler space. The selected area diffraction method of measuring O.D.F. by the transmission electron microscope using thin foils being very laborious, O.D.F.'s are reproduced nowadays from a series of pole-figures by the application of the series expansion method. In this method, the O.D.F. is expressed in a series of generalized spherical harmonics  $C_{\lambda}^{mn} \tau_{\lambda}^{mn}(\phi_1, \phi, \phi_2)$  and the  $C_{\lambda}^{mn}$  coefficients are obtained from the corresponding series expansion of the pole-figure distributions (pole-figures).

## 2.7 Textures in Dual-phase Steels

It was found[65] that when dual-phase steels are manufactured by reheating to the intercritical range followed by



accelerated cooling which transforms the austenite phase to martensite, texture components of the type  $\{111\} \langle 110 \rangle$ ,  $\{111\} \langle 112 \rangle$ ,  $\{337\} \langle 110 \rangle$  and  $\{337\} \langle 776 \rangle$  may be obtained. The intensity of the  $\{111\} \langle uvw \rangle$  components are quite moderate while  $\{337\} \langle uvw \rangle$  components have extremely low intensity. It was suggested that both  $\{111\}$  and  $\{337\}$  type fibre textures may be present in intercritically annealed dual-phase steels in addition to some minor components such as  $\{310\} \langle 001 \rangle$  and  $\{110\} \langle 001 \rangle$ . Moreover, it has also been reported [66] that the texture in hot-rolled dual-phase steels can be described as  $\{111\} \langle 011 \rangle + \{111\} \langle 112 \rangle$  for some and  $\{112\} \langle 110 \rangle$  for other compositions.

For developing dual-phase steels with a good formability, it is known that development of a strong  $\{111\}$  texture in the annealed sheet is necessary. Work by Ray [2] on a C-Mn-Si-V dual phase steel has shown that cold-deforming the intercritically annealed (at  $750^\circ\text{C}$ ) steel by 50%, 70% and 80% produces a texture consisting of a moderately strong  $\{111\} \langle 112 \rangle$  and a rather weak  $\{111\} \langle 110 \rangle$  texture. Further reports by Ray [2] on the same material shows that when intercritically annealed at a higher temperature of  $790^\circ\text{C}$ , 50% and 70% cold-deformed steel showed the same texture components as before, although of much lower intensity. Yet the pole-figure for the 80% cold-rolled material showed a nearly random texture, however.

Later by Ray [67, 68] using the quantitative texture measurement technique, on the same material as given above, indicated that although reasonably strong  $\{111\}$  and  $\{337\}$  fibre-textures could be developed easily in this steel, the value of the Lankford parameter ' $r$ ', was found to be rather low (around

unity). Another significant result showed that the material was found to be practically insensitive to variation of martensite volume fraction within the range of 25% to 41%, so far as the development of {111} fibre texture was concerned. From the results it was concluded that in order to get a high 'r'-value in this material, intercritical annealing to produce a much lower volume fraction of the martensitic phase ( $\ll 25\%$ ) may be beneficial. Researches carried out on a Si-P dual-phase steel indicated that it is possible to reach a  $\bar{r}$  value as high as 1.8 in such a dual-phase steel which contained only upto a maximum of nearly 4% martensite by volume. This amount of martensite was sufficient to eliminate yield point elongation and increase the initial strain-hardening rate. But it is apparent that such a material will not be strong enough though the deep-drawability characteristics will be very good. Thus this method is unsuitable for producing high-strength dual-phase steels with a good deep-drawability and hence, new methods have to be devised.

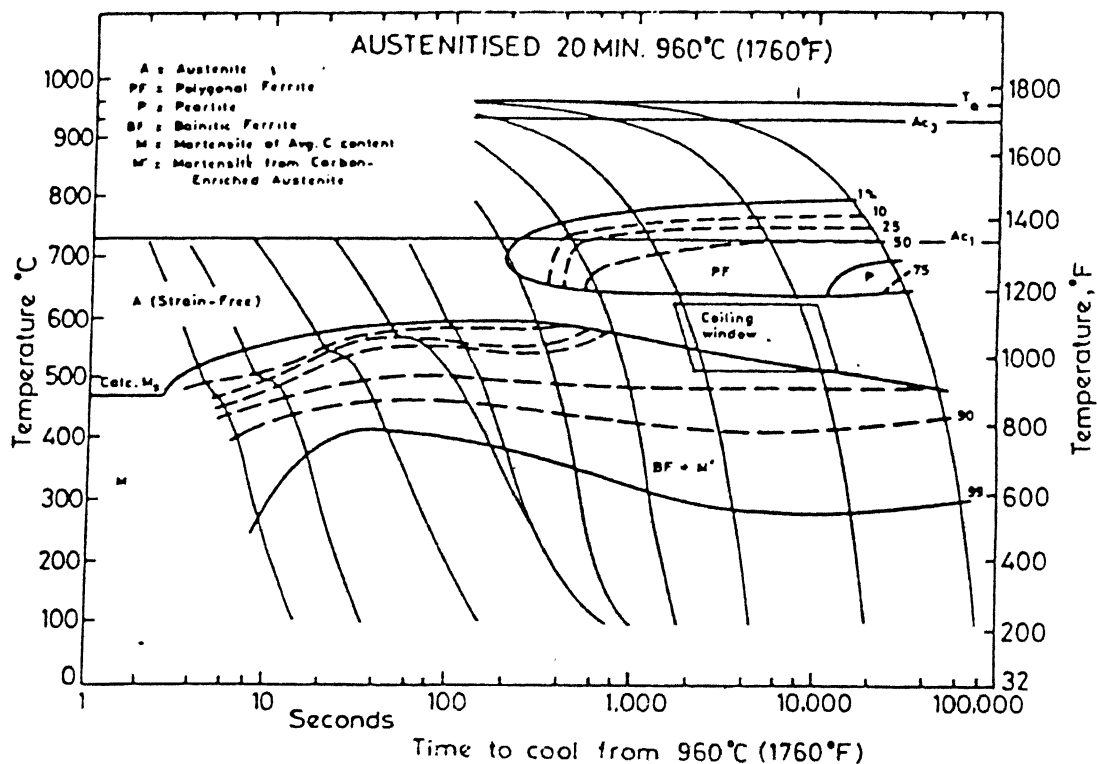


Fig.2.1 C.C.T. curves for a low carbon Mn-Si-Cr-Mo steel developed by Coldren and Tither.

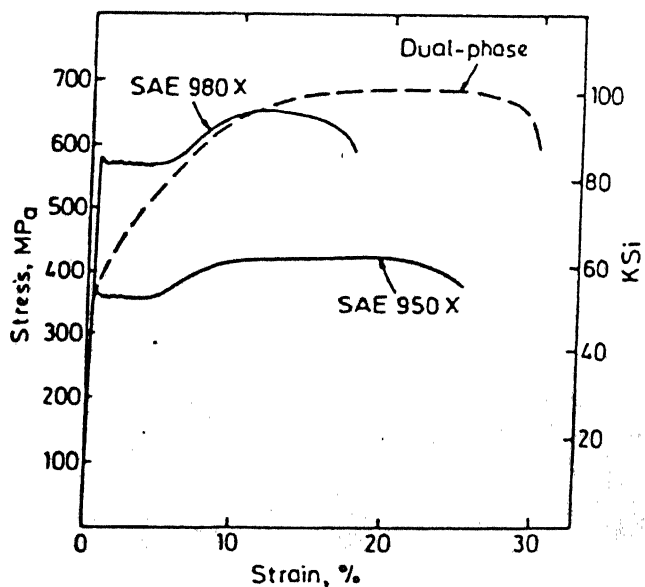


Fig.2.2 Typical stress-strain curves for SAE 950X and 980X steels and an intercritically annealed dual-phase steel.

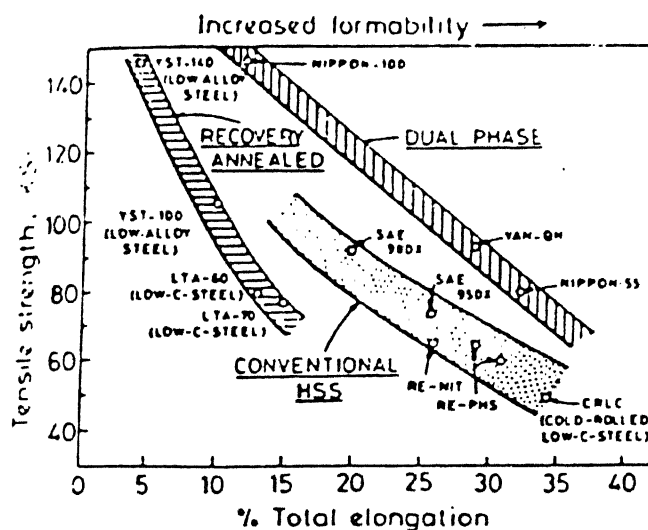


Fig. 2.3. Total elongation as a function of ultimate tensile strength for some of the commercially available high strength steels.

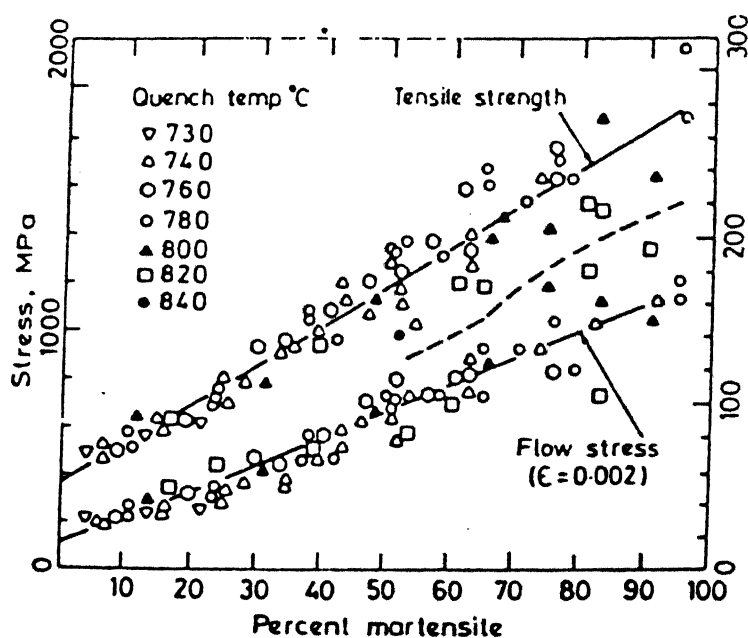


Fig. 2.4. The 0.2% flow stress and the tensile strength as a function of percent martensite for the Fe-Mn-C alloys.

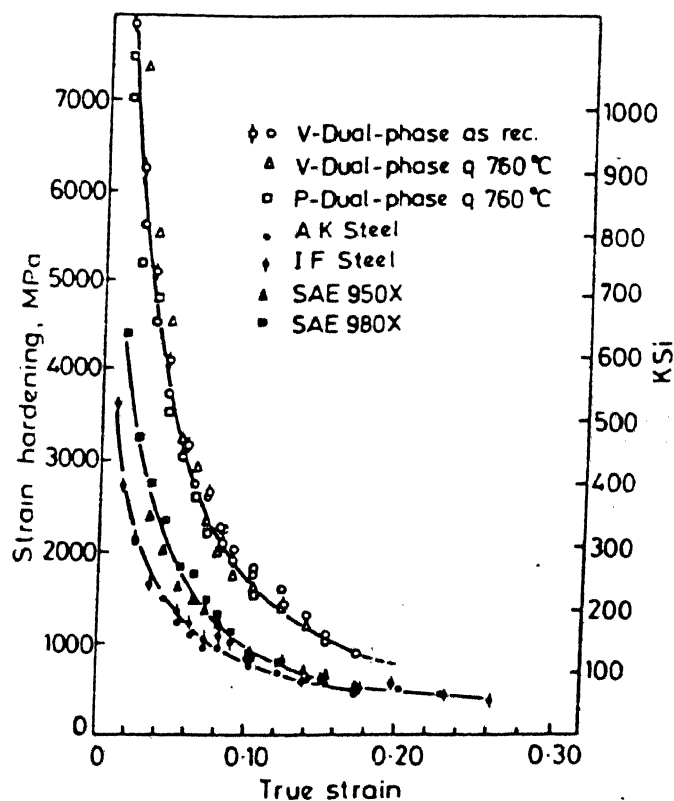


Fig. 2.5. Strain hardening as a function of strain for dual-phase, conventional high strength and low carbon steels.

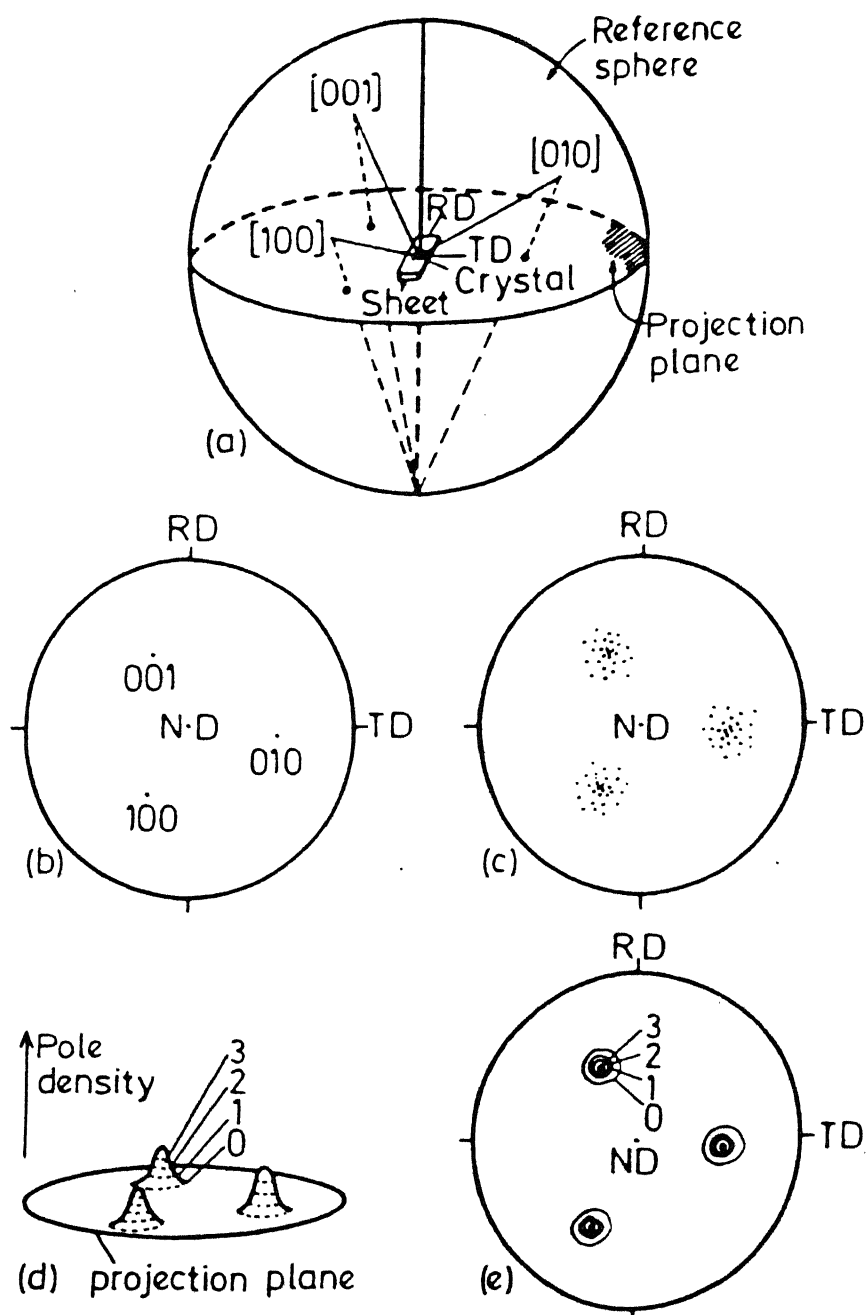


Fig.2.6 (a) Projection sphere and reference directions,  
 (b) Projection of poles for a single grain,  
 (c) Projection of poles from textured grains,  
 (d) Pole density distribution,  
 (e) Contour map of pole density.

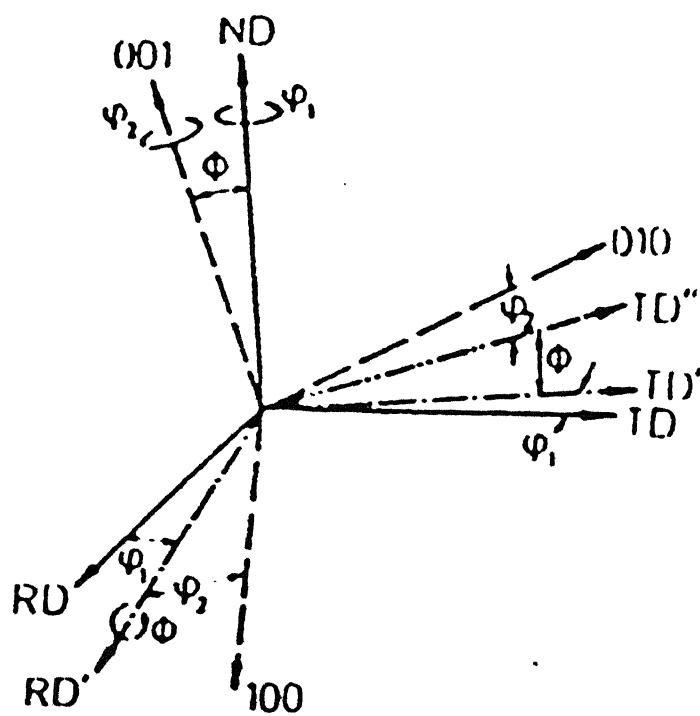


Fig. 2.7. Definition of the Euler angles  $\phi_1, \phi, \phi_2$ .

## CHAPTER III

### Experimental Procedure

#### 3.1 Materials and Their Preparation

The chemical composition of the steel used in the present investigation is given in Table 3.1.

Table 3.1  
Composition of the steel used

Alloy designation	Weight percentage of elements					
	C	Mn	Si	S	P	V
	0.11	1.46	0.47	0.014	0.013	0.09

The alloy was melted in the form of a 30 kg ingot in a high frequency induction furnace at TISCO, Jamshedpur and cast into preheated cast iron moulds. All the heats were deoxidized by Al shots and also treated with misch metal for inclusion control. The cross-sectional area of each ingot was 12 cm X 12 cm (approximately). These ingots were initially forged into bars of square cross-section ( 25 mm each side).

The alloy was received in the form of a forged bar of 90 cms length. For easier handling, this 90 cms bar was cut into six pieces of 15 cms each. Five out these six pieces were split through the centre into halves. These were used for subsequent heat-treatment, etc. A small piece of size ( 25 mm X

25 mm X 10 mm) was cut from the original forged bar to study the optical and electron microstructures of the as-received material.

### 3.2 Heat Treatment, Cold-Rolling and Production of the Dual-Phase Structure

In order to remove any inhomogeneities in the structure of the forged, as-received material, all the bars were homogenised at  $980^{\circ}\text{C}$  for a period of 30 minutes. The heat treatment was carried out in a high temperature muffle furnace whose temperature was maintained within an accuracy of  $\pm 5^{\circ}\text{C}$ . After the heat treatment the bars were air-cooled from the austenitizing temperature to room temperature.

The homogenised bars were subjected to surface grinding to remove scales, etc. and then given 60% deformation by rolling at room temperature. The amount of reduction was kept at around 60% on the basis of trial experiments which showed that the intensity of cold-rolled texture in this material does not increase significantly beyond 60% deformation. The cold-rolling operation was carried out in a two-high, laboratory rolling mill using paraffin oil as lubricant. In between any two successive passes the strips were dipped into a bucket of cold water to minimise temperature rise due to deformation, as far as practicable. The final thickness of the cold-rolled strips varied between 5.0 to 6.0 mm. These cold-rolled bars were then subjected to dual phase treatment.

In order to produce the dual-phase structure, six bars of the cold-rolled samples were sliced into smaller pieces of about 7 to 8 cms each. These were kept at the intercritical annealing temperature of  $810^{\circ}\text{C}$  for two different times of 5 minu



and 30 minutes (three bars for each time). They were then directly quenched in a big bucket of water. The above heat treatments were carried out in a vertical, electrical resistance tube furnace where the temperature was maintained within an accuracy of  $\pm 5^{\circ}\text{C}$ . In this way two different dual-phase structures were developed in the alloy.

The cold rolled material and materials in which dual-phase structures were produced, formed the starting materials for subsequent thermal cycling. The details of the initial thermal and mechanical treatments are listed in Table 3.2.

### 3.3 Thermal Cycling of the Cold-Rolled As Well As Dual-Phase Structures

Small samples (~5 cms) were cut out from the three initial materials and subjected to thermal cycling. The thermal cycling treatment was carried out in a molten salt bath using a commercial I.C.I. salt (Crescent) to maintain a constant temperature during the short time intervals used. The salt bath was contained in a stainless steel crucible of 5.0 cm internal diameter and about 12.0 cm in height. The container with the salt was heated in a vertical, electrical-resistance, tube furnace. The temperature of the melt was checked from time to time using a calibrated chromel-alumel thermocouple kept in a thin-walled stainless steel tube dipping below the surface of the melt. The samples were held in a constant temperature zone in the bath which was found out by carefully measuring the temperature at different regions over a length of time. After each heat treatment samples were quickly taken out from the bath and dropped in a large bucket of water, for quenching.

Table 3.2

Details of the initial thermal and mechanical treatments of the initial starting materials

Alloy	Designation of the starting materials	Initial thermal and mechanical treatments
A6	COO	Austenitized at 980°C for 30 minutes, air-cooled and then cold-rolled (60% deformation given). No dual-phase treatment was given.
A6	A05	Austenitized at 980°C for 30 minutes, air-cooled, cold-rolled (60% deformation), annealed intercritically at 810°C for 5 minutes and then water quenched.
A6	A30	Austenitized at 980°C for 30 minutes, air-cooled, cold-rolled (60% deformation), annealed intercritically at 810°C for 30 minutes and then water quenched.

Two different thermal cycle treatments were given to the dual-phase and cold-worked structures:

- (i) In the first type of cycle the samples were heated to  $800^{\circ}\text{C}$  (between the  $A_3$  and  $A_1$  line in the Fe-C equilibrium diagram), held at this temperature for 2 minutes and then quenched in water. A full cycle was considered to be composed of two such treatments followed in quick succession. The total duration per cycle was 4 minutes.
- (ii) The second cycle also consisted of two half cycles. In the first half cycle the samples were heated to  $925^{\circ}\text{C}$  (above the  $A_3$  line in the Fe-C equilibrium diagram), held at this temperature for 2 minutes and then quenched in water. In the second half cycle the samples were heated to  $800^{\circ}\text{C}$ , held at that temperature for 2 minutes and then quenched in water. Thus the duration of the second type of cycle was also 4 minutes.

Schematic diagrams of the above two types of thermal cycling treatments are given in Figure 3.1. The different types of samples generated by thermal cycling are listed in Table 3.3.

### 3.4 Tensile Testing

Flat tensile test specimens prepared from ten materials listed in Table 3.3 were used for tensile testing. The gauge length of the samples was 15 mm and they were prepared according to the ASTM specification for sheet specimens (ASTM specification:  $L_0/\sqrt{A_0} = 4.5$  where  $L_0$  = gauge length and  $A_0$  = original cross-sectional area). The tensile tests were performed at

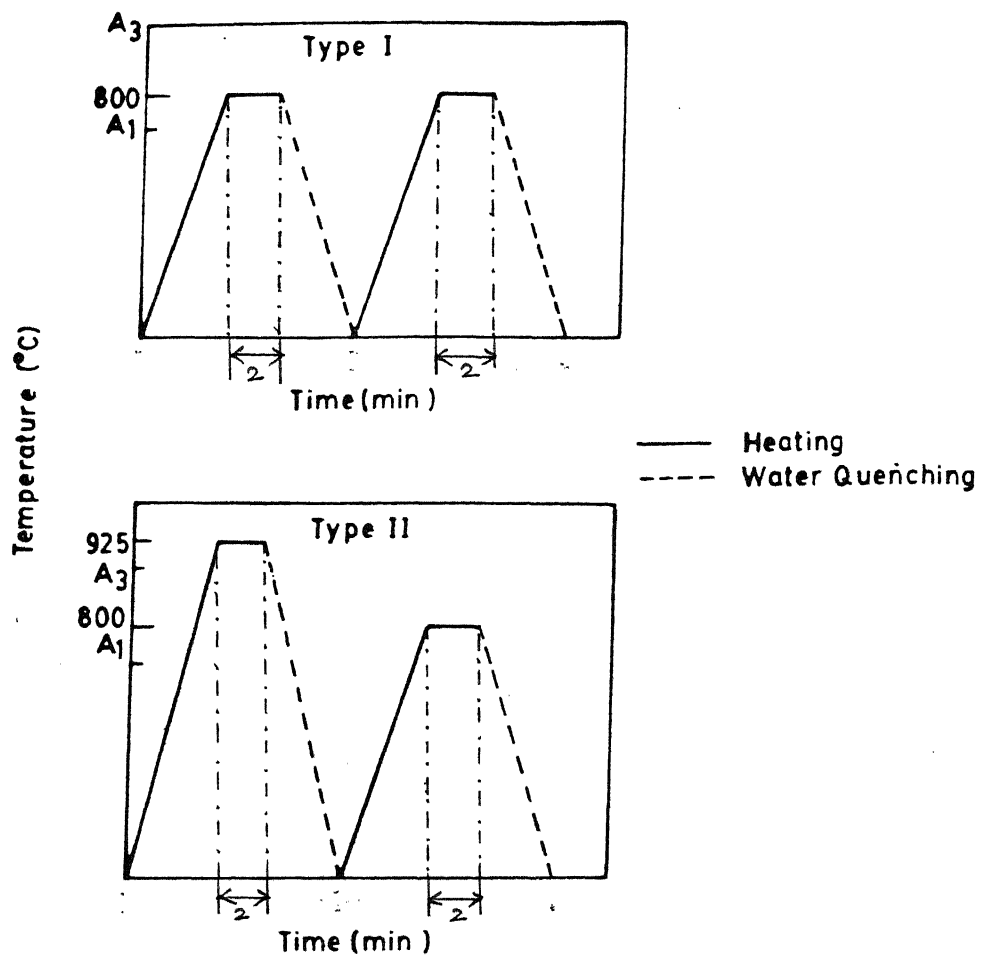


FIG.3-1 SCHEMATIC DIAGRAMS OF THE TWO SEPARATE TYPES OF THERMAL-CYCLING TREATMENTS

Table 3.3

Details of the different types of samples generated by thermal-cycling treatments

Initial material	Designation of thermally cycled structure	Details of heat-treatment for the production of thermal-cycled structures
C00	C0000	Kept as it is without subjecting it to any cyclic treatment
C00	C0005	Type of cycle : Type I Number of cycles given : 5
C00	C0010	Type of cycle : Type I Number of cycles given : 10
A05	A0501	Type of cycle : Type I Number of cycles given : 1
A05	A0510	Type of cycle : Type I Number of cycles given : 10
A30	A3001	Type of cycle : Type I Number of cycles given : 1
A30	A3010	Type of cycle : Type I Number of cycles given : 10
C00	2C0010	Type of cycle : Type II Number of cycles given : 10
A05	2A0510	Type of cycle : Type II Number of cycles given : 10
A30	2A3010	Type of cycle : Type II Number of cycles given : 10

room temperature using an Instron (Model 1195) machine. A cross-head speed of 0.5 mm/minute, a chart speed of 20 mm/minute and a full scale load of 50 KN were used during testing. From the recorded charts, 0.2% proof stress, 1.0% proof stress, ultimate tensile strength, fracture stress, strain at fracture and total elongation values were calculated. The load-elongation data read from the charts were first converted to engineering stress-engineering strain values. These were then converted to true plastic stress ( $\sigma$ ) and true plastic strain ( $\epsilon$ ). The strain hardening exponent 'n' was determined by plotting  $\ln \sigma$  values against  $\ln \epsilon$  values and finding the slope in each case. The work hardening rate  $\frac{d\sigma}{d\epsilon}$  was also calculated at different values of true plastic strain and plotted against  $\epsilon$ .

### 3.5 Optical Metallography

#### 3.5.1 Specimen Preparation and Examination

To study the optical microstructures of the as-received, the initial starting as well as the thermally cycled materials, transverse sections of small metallographic samples were properly ground and subsequently polished in the usual manner. Each sample was prepared with repeated polishing and etching treatments using 2% nital (for 20-21 seconds) to produce a scratch-free microstructure showing reasonably good contrast. But this etching treatment failed to reveal the martensite properly, though it could delineate the ferrite regions satisfactorily.

In order to highlight the sizes and shapes of martensitic regions an improved technique [69] was used to characterize the structures. The process involved conventional polishing and

etching with a 4% picral solution (4 g picric acid in 100 cc of methyl alcohol) for about a minute. This was followed by a short etching treatment using 2% nital with the intention of revealing the ferrite grain boundaries clearly. Finally, the samples were stained by holding them in boiling alkaline chromate solution (8-10 gm  $\text{CrO}_3$  in 75 cc of  $\text{H}_2\text{O}$  and 40 g NaOH) for different lengths of time depending on the samples. The different periods of staining were selected on the basis of trial and error. The staining time required varied between 30-35 seconds and led to martensitic regions etching dark and new ferrite regions (formed during cooling from intercritical annealing temperature) etching bright. The old (untransformed) ferrite appeared gray in contrast to other micro-constituents. After staining, the specimens were washed in running water and rinsed with methanol and dried. Photomicrographs were taken from these specially stained surfaces.

### 3.5.2 Quantitative Metallography

An Omnicon Alpha 500 Image Analyser was used to determine the volume percentages of martensite in the dual-phase structures as well as to make a quantitative measurement of ferrite grain size in different samples. The volume percentage of martensite was measured randomly over ten different areas of each sample and the data averaged out. The ferrite grain size distribution was noted at five random locations on the surface of each sample and the values obtained were then averaged out. Histograms were plotted to record the percentage of particles over different pre-determined size ranges.

### 3.6 Scanning Electron Microscopy

The thermally cycled materials, after conventional polishing, etching and staining, were examined in a Jeol JSM 840A Scanning Electron Microscope (S.E.M.) operated at 20 KV. The surface features of the heat treated samples as well as the fracture characteristics of tensile samples were studied using the secondary electron mode. The S.E.M. was also used to study the morphology of a few inclusions present in the experimental steel.

### 3.7 Hardness Measurements

#### 3.7.1 Macrohardness Measurements

Vickers' hardness measurements of the initial starting materials as well as the materials listed in Table 3.3 was done on standard Vickers' Hardness Testing machine using a load of 10 kg. Indentations were made at three different regions of the polished samples and the average value was reported.

#### 3.7.2 Microhardness Measurements

The microhardness values of the ferritic phase present in all the ten samples listed in Table 3.3 were determined on the polished and etched specimens already used for optical microscopic studies. The measurements were performed in a Leitz MINILOAD 2 microhardness tester. The etched specimens were focussed at 500X and the ferrite grain to be examined was located exactly under the cross-wire. The load used in each case was 25 gms.



### 3.8 Determination of Texture

Crystallographic textures were determined from the mid sections of the samples listed in Table 3.3. Specimens of size 24 mm X 14 mm were cut out from sheets of the different materials. The dimension along the rolling direction is 25 mm and that along the transverse direction is 14 mm.

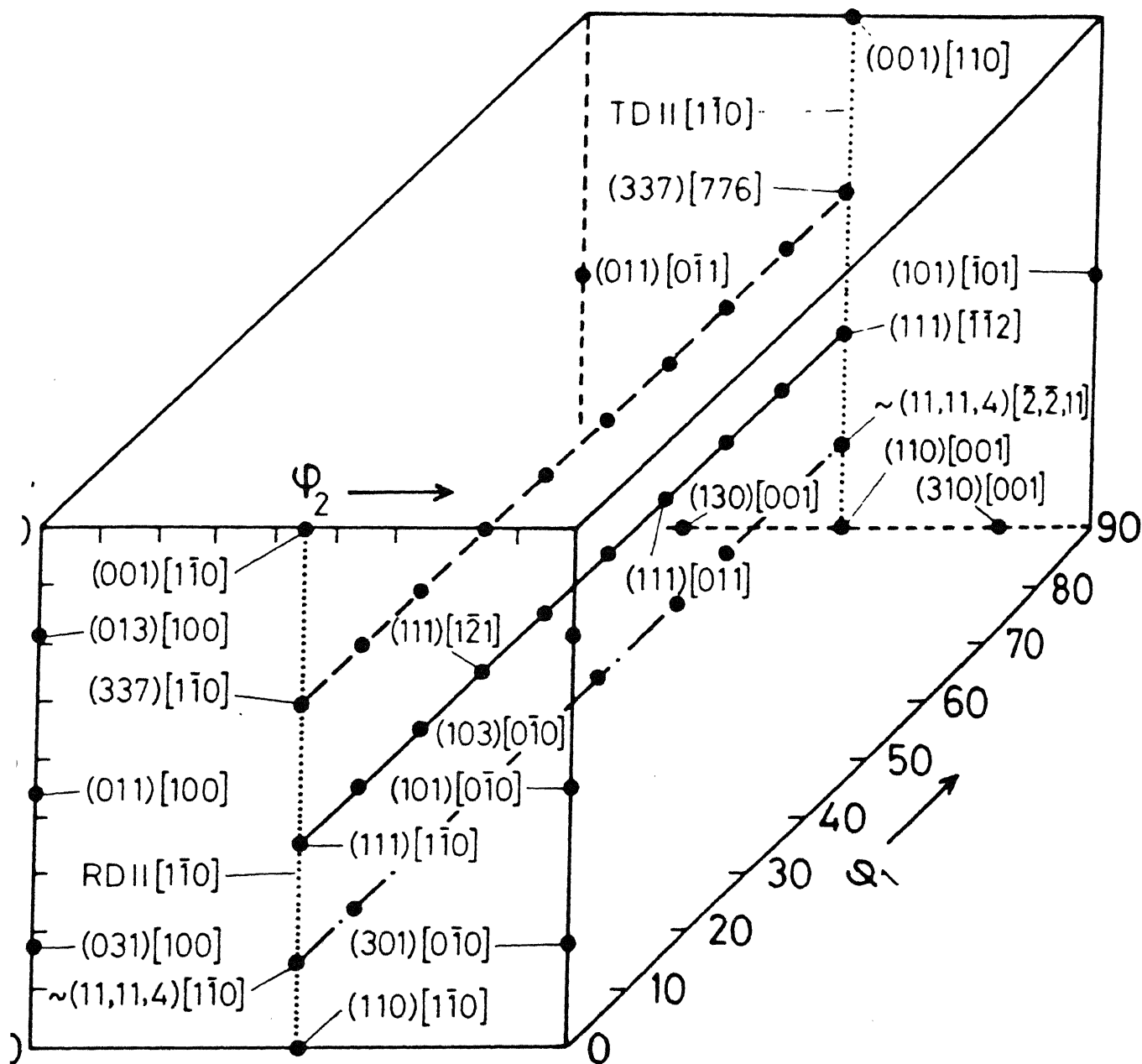
A little less than half of the total thickness was removed from one of the flat surfaces in all texture specimens by milling. The specimens were then ground and polished metallographically and then lightly etched to remove any disturbed layer.  $\{110\}$  pole-figures were determined from these texture samples by the Schulz reflection method [70] using  $\text{CoK}_\alpha$  radiation with an iron filter. Intensity levels on the pole-figures were determined by comparison with the intensity obtained from a solid specimen of pure iron which had been randomised by repeated deformation and annealing.

To have a better resolution of the texture components in the pole-figures and also to have a more complete idea regarding the textures of the different samples, O.D.F.'s were measured from each one of them. For this kind of analysis the method of incomplete pole-figures [64] was used. For this purpose incomplete pole-figure (within the range  $0-85^\circ$ ) intensity data were obtained for  $\{110\}$ ,  $\{200\}$  and  $\{112\}$  reflections using the Siemens automatic texture goniometer system [71, 72] with  $\text{CoK}_\alpha$  radiation.

In the present investigation, the O.D.F. analysis technique as developed by Roe [73, 74] and mainly by Bunge [75, 76]

has been followed. In this method the orientation of a crystallite in a polycrystalline specimen is specified with respect to the specimen co-ordinate system by the three Eulerian angles  $\phi_1$ ,  $\phi_2$  and  $\phi_3$ .

The Cartesian-Euler angle space, with the three dimensional orientation distribution function within, is normally represented, for B.C.C. materials, in the form of sections,  $\phi_1 = \text{constant}$  ( $\phi_1 = 0, 5, 10, \dots, 90 \text{ deg.}$ ). Most of the important crystallographic orientations for B.C.C. materials appear in these sections. Figure 3.2 represents an isometric view of the three dimensional Eulerian space with the positions of a few important ideal orientations marked therein. Some important ideal orientations for B.C.C. materials are also shown in a tabular form in Table 3.4.



- · —  $\phi = 75^\circ, \psi_2 = 45^\circ; [11,11,4] \parallel \text{ND FIBRE}$
- $\phi = 55^\circ, \psi_2 = 45^\circ; [111] \parallel \text{ND FIBRE}$
- $\phi = 30^\circ, \psi_2 = 45^\circ; [337] \parallel \text{ND FIBRE}$
- Ideal Positions

fig. 3.2 Three - dimensional Euler Space showing locations of ideal orientations.

Table 3.4

## Euler Angles for Ideal Orientations

Ideal orientations	Euler angles		
	$\phi_1$	$\phi$	$\phi_2$
(111) [0 $\bar{1}$ 1]	60	55	45
(111) [1 $\bar{1}$ 0]	0	55	45
(111) [1 $\bar{2}$ 1]	30	55	45
(111) [ $\bar{1}$ $\bar{1}$ 2]	90	55	45
(337) [1 $\bar{1}$ 0]	0	31	45
(733) [0 $\bar{1}$ 1]	49	68	67
(011) [100]	0	45	0
(110) [001]	90	90	45
(101) [0 $\bar{1}$ 0]	0	45	90
(012) [100]	0	18	0
(031) [100]	0	72	0
(103) [0 $\bar{1}$ 0]	0	18	90
(301) [0 $\bar{1}$ 0]	0	72	90
(130) [001]	90	90	18
(310) [001]	90	90	72
(010) [101]	45	90	0
(100) [0 $\bar{1}$ 1]	45	90	90
(001) [1 $\bar{1}$ 0]	$\phi_1 + \phi_2 = 45$	0	
(001) [ $\bar{1}$ $\bar{1}$ 0]	$\phi_1 + \phi_2 = 135$	0	
(110) [1 $\bar{1}$ 0]	0	90	45
(011) [0 $\bar{1}$ 1]	90	45	0
(101) [ $\bar{1}$ 01]	90	45	90
(112) [1 $\bar{1}$ 0]	0	35	45
(335) [1 $\bar{1}$ 0]	0	40	45
near (445) [1 $\bar{1}$ 0]	0	50	45
near (11, 11, 4) [1 $\bar{1}$ 0]	0	75	45
near (11, 11, 4) [ $\bar{2}$ , $\bar{2}$ , 11]	90	75	45

## CHAPTER IV

### Experimental Results

The effects of two different kinds of thermal cycling treatments on the following aspects of the experimental steel have been determined:

- (a) Microstructure
- (b) Mechanical properties
- (c) Crystallographic texture.

In this chapter, the relevant results obtained during the investigation in the areas mentioned above are enumerated.

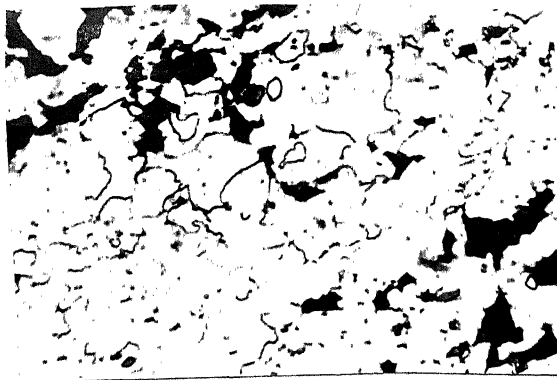
#### 4.1 Microstructure

##### 4.1.1 Microstructures of As-received and Homogenised Materials

The as-received and homogenised microstructures of the experimental material are shown in Figures 4.1(a) and (b) respectively. As expected, the structure of the as-received material reveals a ferrite-pearlite aggregate. On homogenisation the grains become more equiaxed than those visible in the as-received structure.

##### 4.1.2 Microstructures of Initial Starting Materials

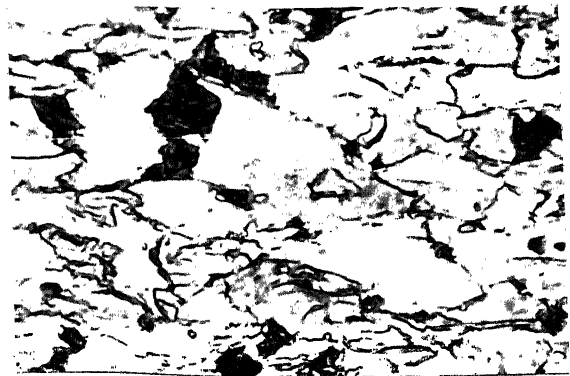
The microstructures of the initial starting materials are shown in Figures 4.1(c) to (e). In case of the cold-worked structure shown in Figure 4.1(c), the grains are found to be elongated in the direction of rolling. Staining has caused the ferrite to etch bright and the pearlite to etch dark. After the dual-phasing treatment the conventionally etched and subsequently



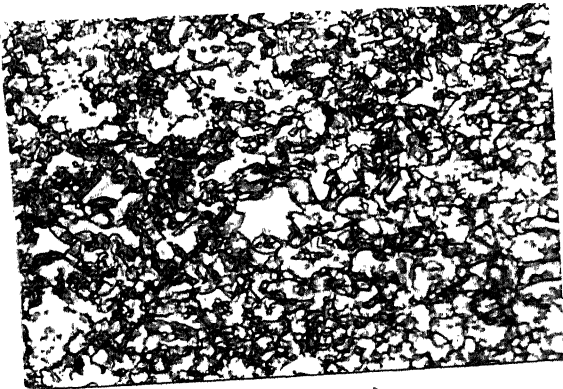
(a) (500X)



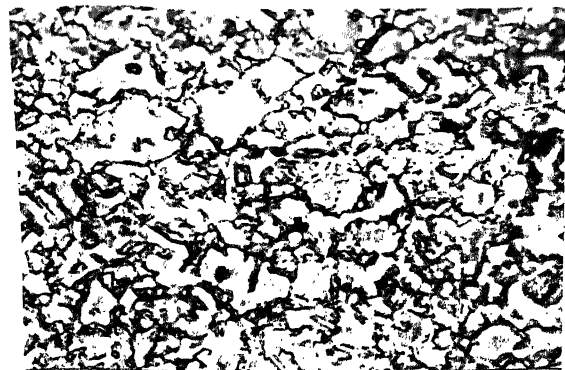
(b) (500X)



(c) (1000X)



(d) (1000X)



(e) (1000X)

**Fig. 4.1.** Optical microstructures of: (a) as-received material; (b) homogenised material; (c) 60% cold-rolled material (C00); (d) cold-rolled material dual-phase treated at 810°C for 5 minutes (A05) and (e) cold-rolled material dual-phase treated at 810°C for 30 minutes (A30).

stained microstructures show regions with three distinct contrasts [Figures 4.1(c) and (d)]. The old ferrite is etched grey, the new ferrite bright and the dark-etching phase is martensite. The grains of the cold-deformed material, dual-phase treated at  $810^{\circ}\text{C}$  for 5 minutes are finer than those treated at the same temperature for a longer period of time (30 minutes). The martensite is found to occur as islands along the ferrite grain boundaries.

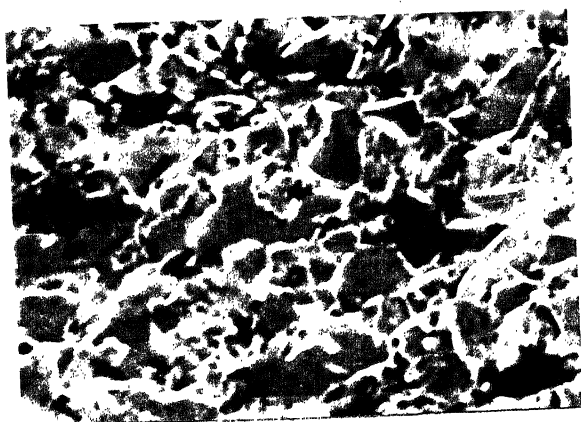
The scanning electron micrographs of the etched surfaces of the starting materials are shown in Figures 4.2(a) to (c). These micrographs also delineate the martensite, the old and the new ferrite areas distinctly and give a better idea of the distribution of phases as compared to the optical microstructures because of the high resolution of the S.E.M.

#### 4.1.3 Microstructures of Thermally Cycled Materials

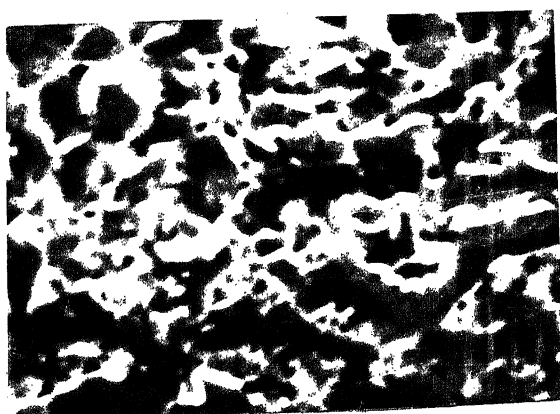
Optical microstructures of specimens subjected to Type-I thermal cycling treatment are shown in Figures 4.3(a) to (f). Figure 4.3(a) shows that even after five cycles are given to the cold-worked material the effect of cold-work persists as incomplete recrystallization takes place. After ten cycles, the structure shows strain-free grains of ferrite with strings of martensite islands on the ferrite grain boundaries (Figure 4.3(b)). The optical microstructures obtained for the dual-phase aggregate (produced by 5 minutes annealing at  $810^{\circ}\text{C}$ ) after one and ten numbers of thermal cycling are shown in Figures 4.3(c) and (d) respectively. Figure 4.3(c) shows more or less uniform ferrite grains with martensitic regions at the grain



(a) (1500X)



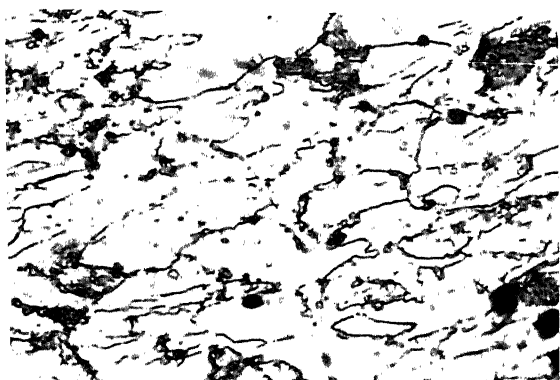
(b) (3000X)



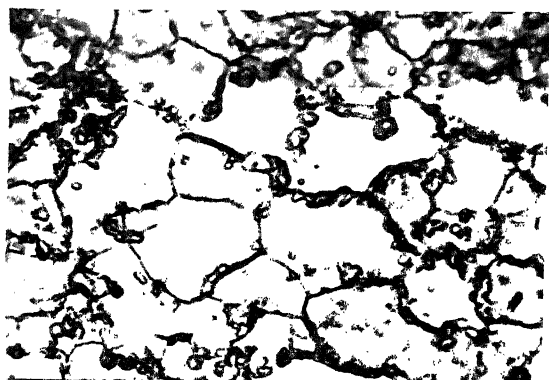
(c) (3000X)

Fig. 4.2. Scanning electron micrographs of: (a) 60% cold-rolled material (C00); (b) cold-rolled material dual-phase treated at 810°C for 5 minutes (A05) and (c) cold-rolled material dual-phase treated at 810°C for 30 minutes (A30).

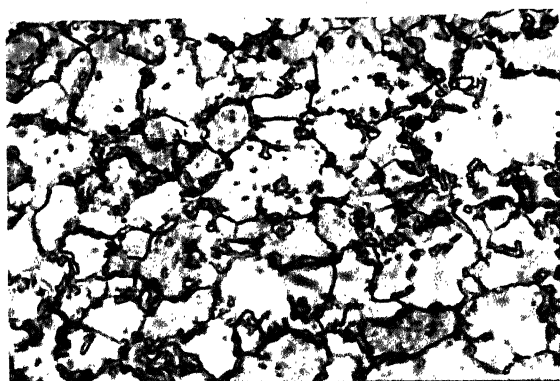




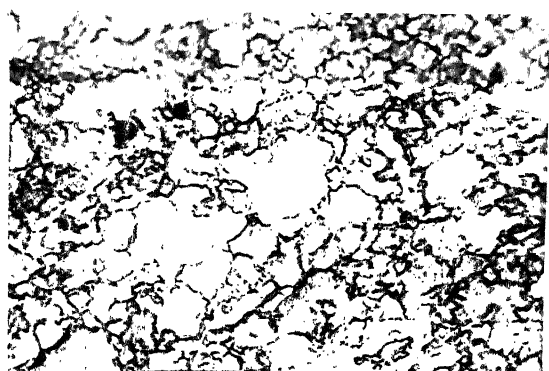
(a) (1000X)



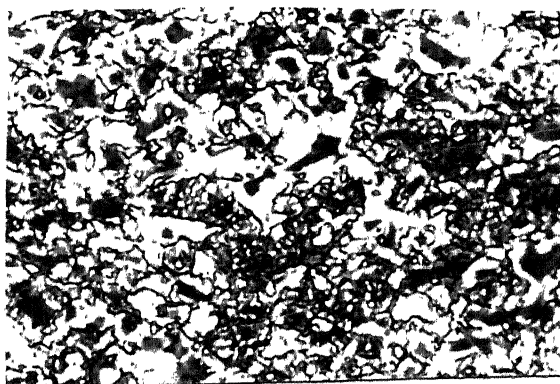
(b) (1000X)



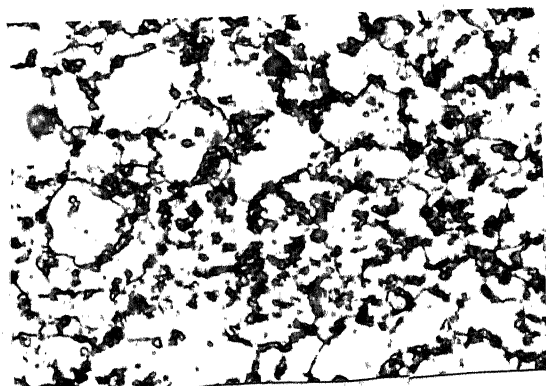
(c) (1000X)



(d) (1000X)



(e) (1000X)



(f) (1000X)

Fig. 4.3.

Optical microstructures obtained by subjecting the initial materials to Type-I thermal-cycling treatment: (a) C00 for 5 cycles (C0005); (b) C00 for 10 cycles (C0010); (c) A05 for 1 cycle (A0501); (d) A05 for 10 cycles (A0510); (e) A30 for 1 cycle (A3001); (f) A30 for 10 cycles (A3010).

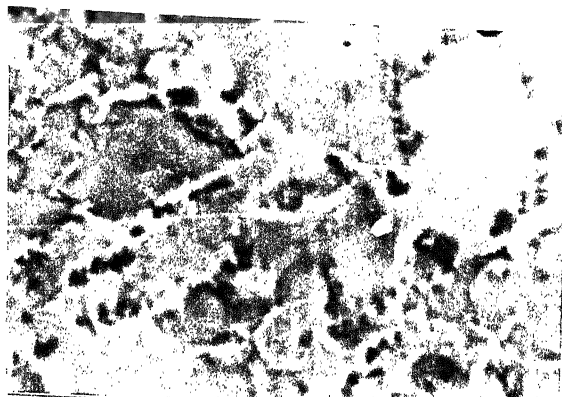
boundaries. An aggregate of rather fine grains of ferrite are obtained after ten cycles (Figure 4.3(d)) together with a few rather large-size grains. Microstructures similar to the above have also been obtained after thermal cycling of the dual-phase structure produced by 30 minutes annealing at  $810^{\circ}\text{C}$  [Figure 4.3(e) and (f)]. Clearly, a larger number of cycles leads to a perceptible decrement of the ferrite grain size.

Figures 4.4(a) to (c) represent the scanning electron micrographs obtained from the etched and stained surfaces of all the three starting materials after Type-I thermal-cycling (ten cycles). It is at once clear that the maximum ferrite-grain-refinement due to thermal-cycling has taken place for the dual-phase structure produced by 5 minutes annealing at  $810^{\circ}\text{C}$ .

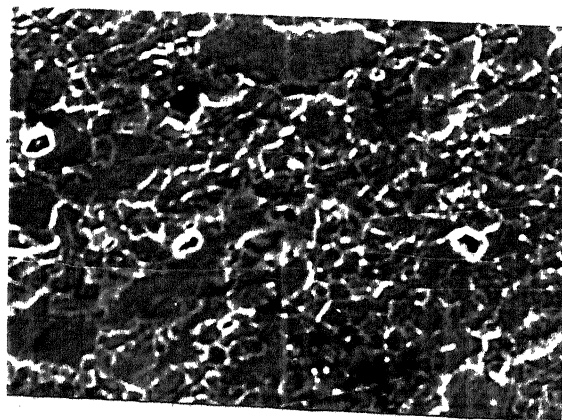
Figures 4.5(a) to (c) reveal optical microstructures of the initial starting materials subjected to the Type-II thermal-cycling treatment. In all these microstructures martensitic areas are found to be present along the grain boundaries of ferrite. There is not much difference in the ferrite grain sizes in these samples. However, in the original cold-worked sample, after ten cycles of thermal-cycling, the martensitic and ferritic areas are distributed in a rather uniform manner. Similar features can also be seen in the corresponding scanning electron micrographs [Figures 4.6(a) to (c)].

The volume percent martensite present in the various thermally cycled specimens are given in Table 4.1.

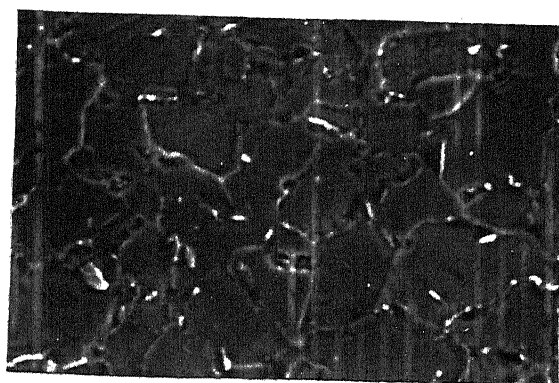
It is quite clear from this table that, for Type-I thermal-cycling treatment, higher number of cycles results in



(a) (2500X)

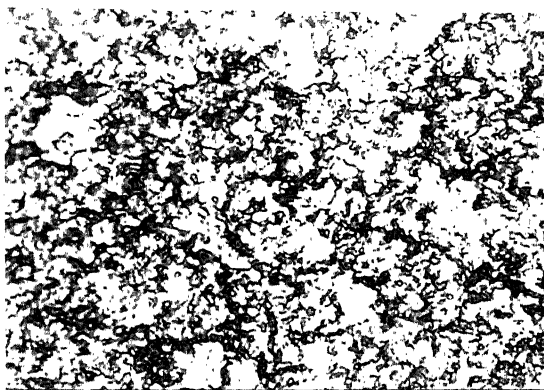


(b) (1500X)

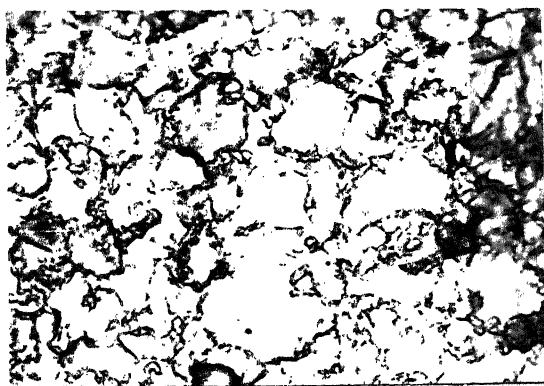


(c) (3000X)

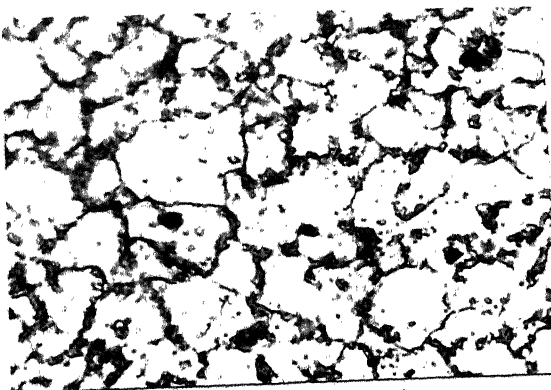
Fig. 4.4. Scanning electron micrographs obtained by subjecting the initial materials to Type-I thermal-cycling treatment: (a) C00 for 10 cycles (C0010); (b) A05 for 10 cycles (A0510); and (c) A30 for 10 cycles (A3010).



(a) (1000 X)

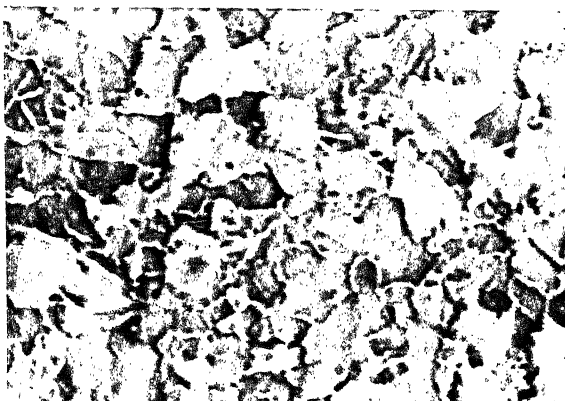


(b) (1000 X)

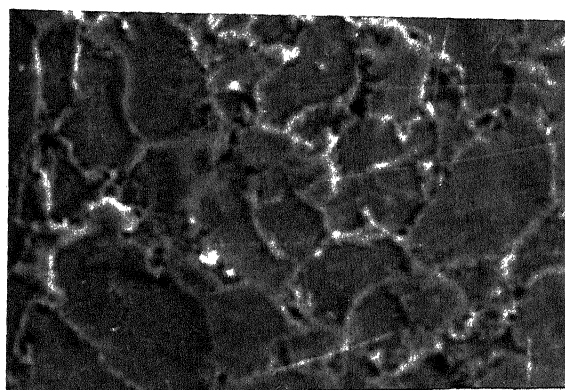


(c) (1000 X)

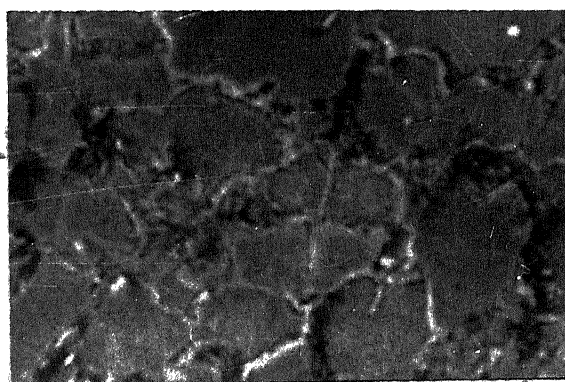
Fig. 4.5. Optical microstructures obtained by subjecting the initial starting materials to Type-II thermal-cycling treatment: (a) C00 for 10 cycles (2C0010); (b) A05 for 10 cycles (2A0510); and (c) A30 for 10 cycles (2A3010).



(a) (1500x)



(b) (3000x)



(c) (3000x)

Fig. 4.6. Scanning electron micrographs obtained by subjecting the initial starting materials to Type-II thermal-cycling treatment: (a) C00 for 10 cycles (2C0010); (b) A05 for 10 cycles (2A0510); and (c) A30 for 10 cycles (2A3010).

Table 4.1

Volume percent martensite in thermally-cycled samples

Sample	Average volume percent martensite present
C0005	7
C0010	16
A0501	20
A0510	16
A3001	25
A3010	20
2C0010	16
2A0510	22
2A3010	26

an increase in the volume fraction of martensite for the initially cold-rolled material. However, this behaviour is totally opposite in case of the materials which were given a dual-phasing treatment subsequent to cold-rolling. In general, for the same number of cycles, Type-II treatment seems to produce a larger volume fraction of martensite.

#### 4.1.4 Results of Grain-size Measurements

The ferrite grain size distributions in the thermally cycled (Type-I) samples are shown in the form of histograms in Figures 4.7 to 4.9. Figure 4.7 clearly indicates that thermal-

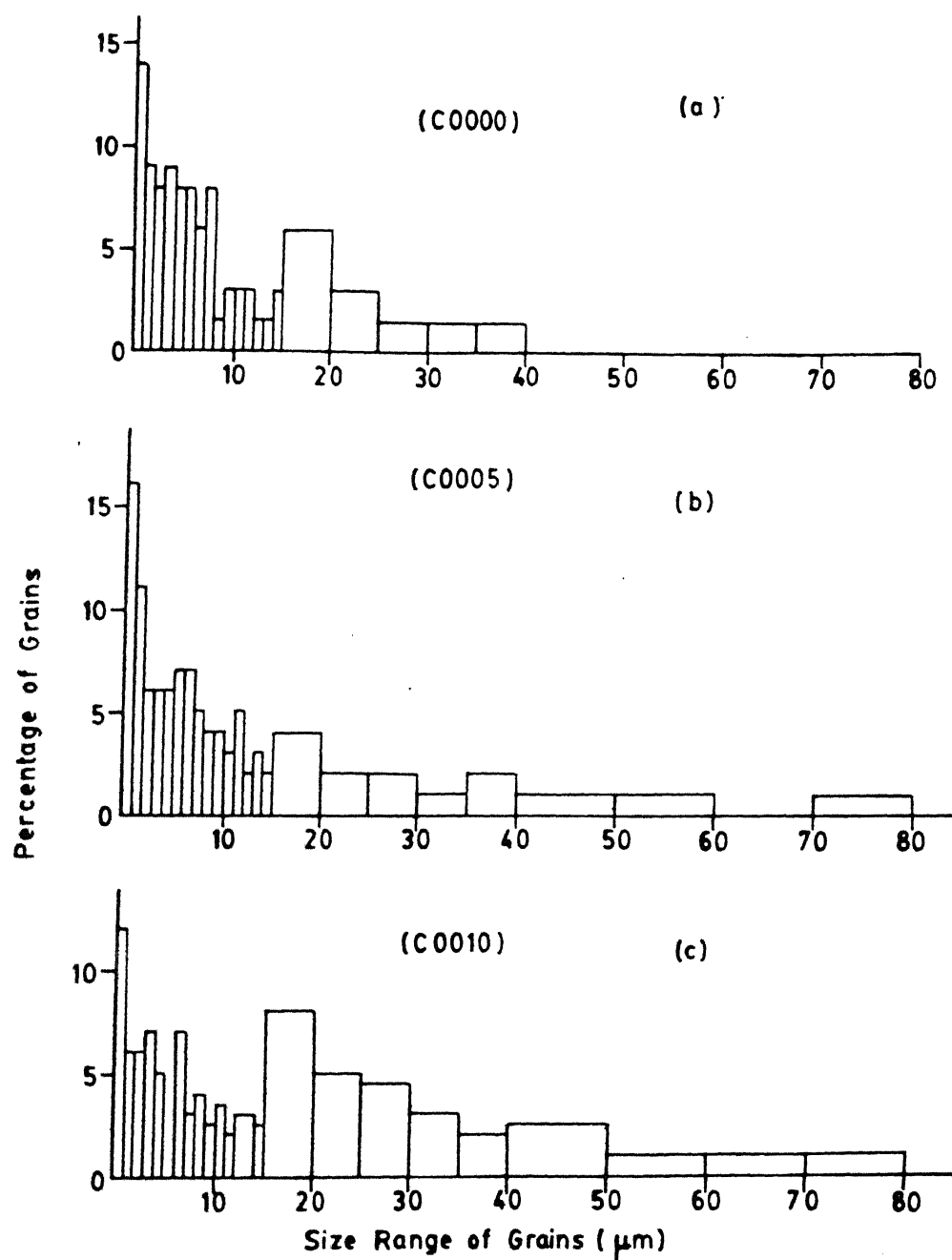


FIG. 4.7 GRAIN SIZE DISTRIBUTION IN THERMALLYCYCLED STEELS

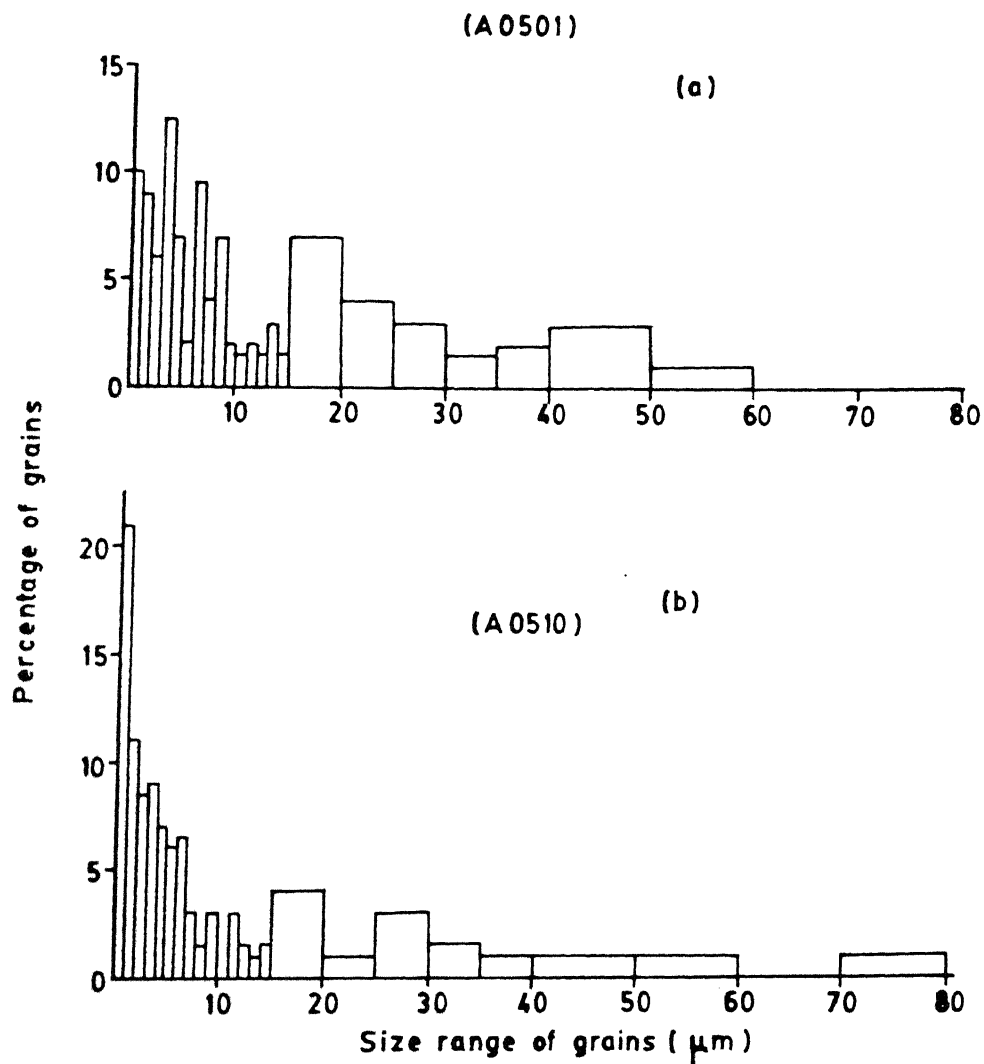


FIG. 4-8 GRAIN SIZE DISTRIBUTION IN THERMALLY CYCLED STEELS



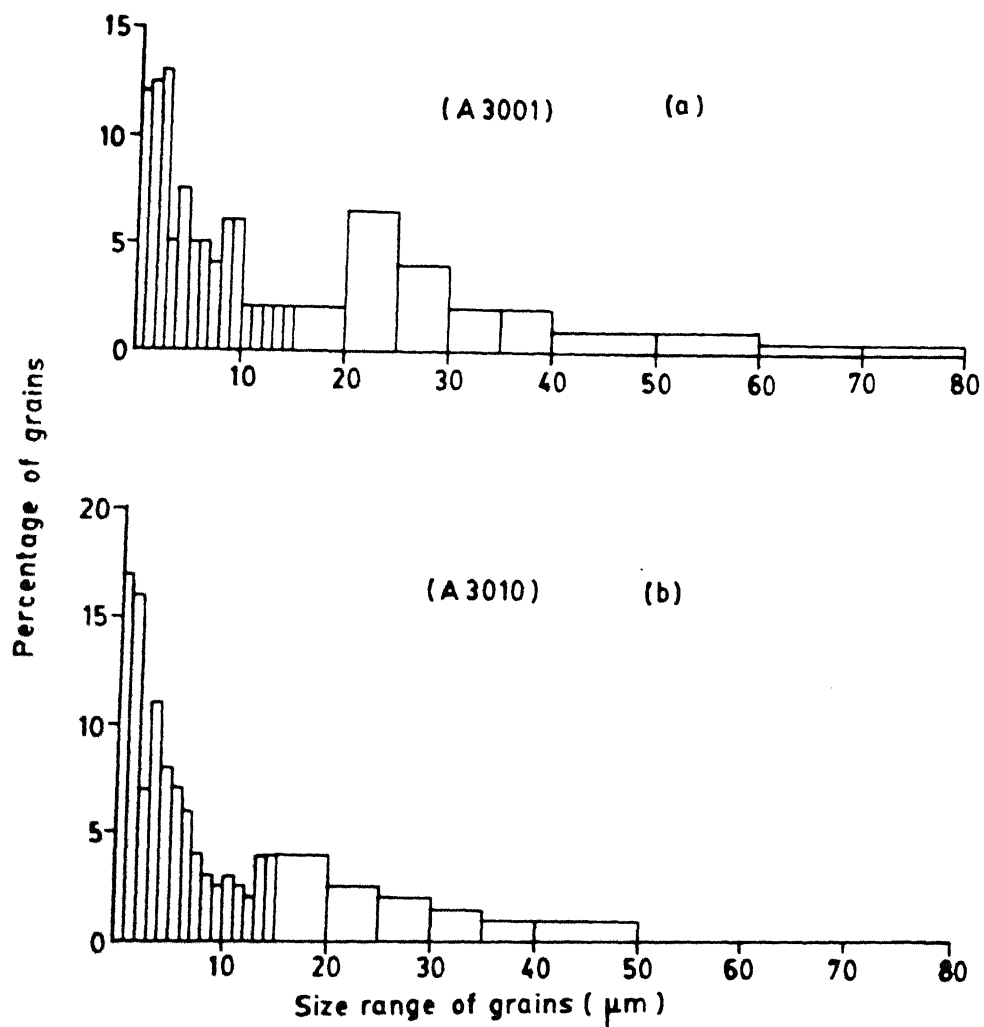


FIG. 4-9 GRAIN SIZE DISTRIBUTION IN THERMALLY CYCLED STEELS

cycling upto a total of ten cycles does not produce any appreciable ferrite grain refinement. In contrast, for the initial dual-phase structure produced by intercritical annealing at  $810^{\circ}\text{C}$  for 5 minutes, thermal cycling upto a total of ten cycles has definitely led to significant refinement of the ferrite grains (Figure 4.8). The samples where the initial dual-phase structure was produced by annealing for 30 minutes at  $810^{\circ}\text{C}$ , on the other hand, did not respond in any meaningful way towards thermal-cycling, so far as grain-refinement is concerned (Figure 4.9).

Figure 4.10 shows the effect of Type-II thermal-cycling treatment on the three initial starting materials. As can be seen in this figure, thermal-cycling upto a total of ten cycles seems to produce a comparable ferrite-grain size distribution in all the three samples.

## 4.2 Mechanical Properties

### 4.2.1 Hardness and Microhardness

Macroscopic hardness values were measured on the polished and etched surfaces of the thermally-cycled materials. It was observed that for the same sample, the hardness values showed a wide difference from place to place. This was nothing unusual since the samples examined had an essentially duplex structure containing soft ferrite and hard martensite. The hardness value measured, will naturally depend on the property of the exact location where the indentations are made.

It was, therefore, decided to determine the microhardness values on the ferritic phase alone in the different samples.

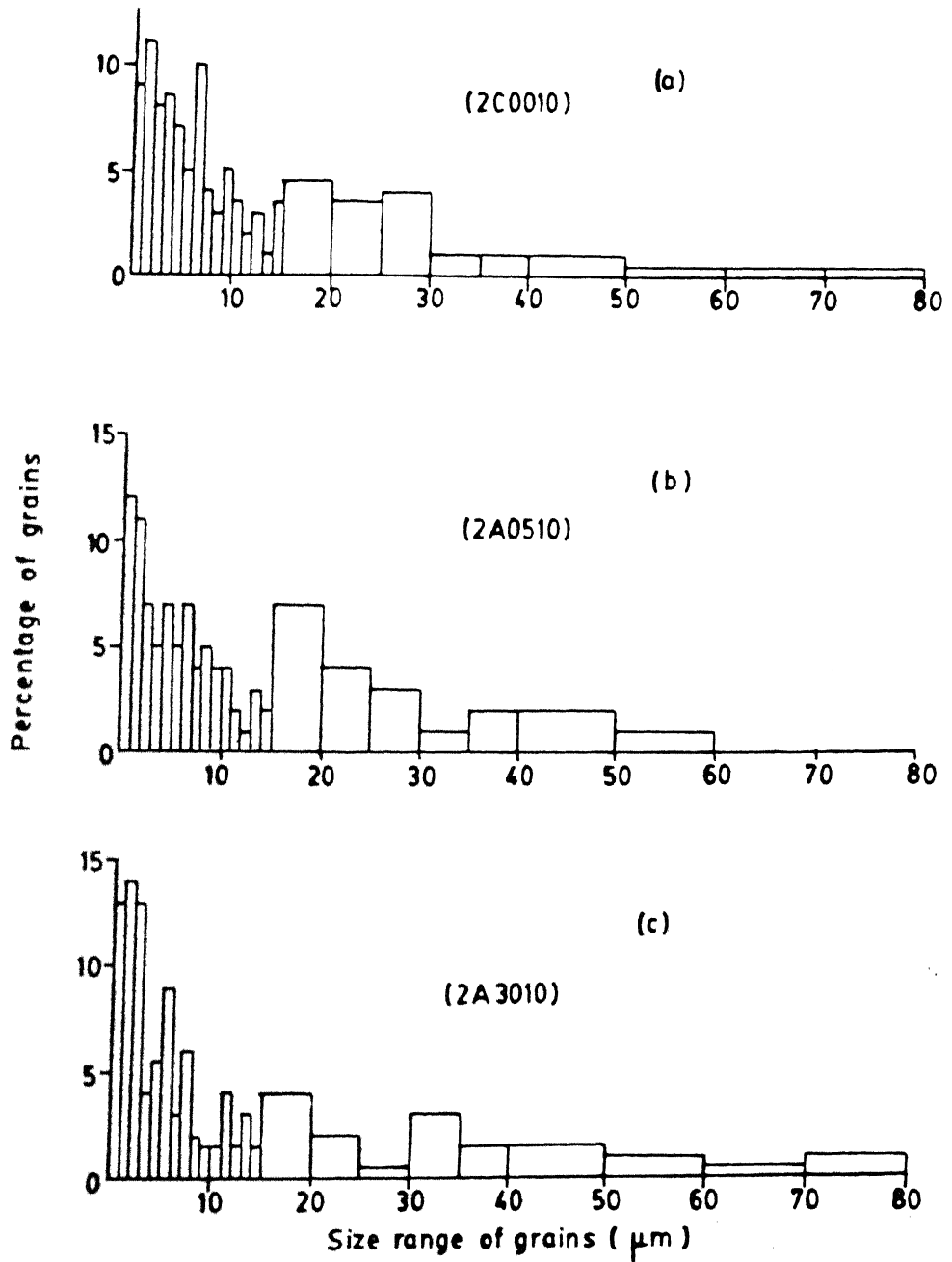


FIG. 4-10 GRAIN SIZE DISTRIBUTION IN THERMALLY CYCLED STEELS

This was done with an idea of finding out the hardness changes in ferrite due to the various thermal-cycling treatments. The relevant microhardnesses of the ferrite phase in the different samples are presented in Table 4.2.

Table 4.2

Microhardness of ferrite phase for the thermally-cycled samples

Sample	Microhardness (VPN)
C0005	272
C0010	174
A0501	222
A0510	248
A3001	263
A3010	225
2C0010	219
2A0510	224
2A3010	235

Table 4.2 shows that, on an average, the ferrite phase hardness does not vary significantly for most of the samples. The microhardness for the C0005 sample is the highest, which is presumably due to the fact that the ferrite at this stage is not fully recrystallised [see Figure 4.3(a)]. After ten cycles, however, the microhardness of ferrite goes down drastically.

#### 4.2.2 Tensile Properties

A few tensile properties of the thermally cycled materials, such as 0.2% proof stress, 1.0% proof stress, U.T.S., total elongation percent and the strain-hardening exponent 'n', are shown in a tabular form in Table 4.3.

Table 4.3

Tensile test results of the thermally cycled materials

Sample	0.2% proof stress (MPa)	1% Proof stress (MPa)	U.T.S. (MPa)	Total elongation %	Strain hardening exponent 'n'
C0005	355	410	573	39.3	0.186
C0010	225	324	618	32.5	0.271
A0501	384	477	569	38.0	0.134
A0510	274	373	553	39.4	0.260
A3001	291	458	538	34.0	0.134
A3010	320	353	546	38.7	0.265
2C0010	337	417	566	29.3	0.178
2A0510	403	473	628	31.8	0.172
2A3010	327	399	563	25.2	0.179

Table 4.3 indicates clearly that, for the Type-I thermal-cycling treatment there is generally a decrease of the 0.2% and 1% proof stress with increase in the total number of cycles. There is a lone exception of this behaviour for the samples A3001 and A3010 (0.2% proof stress). The U.T.S. values for all

the thermally cycled samples do not show very significant differences and, in fact, lie within a range of 550-630 MPa. The percentage elongation in all the samples is reasonably high, all greater than 30%. The value of the strain-hardening exponent, 'n' has been found to be consistently low ( $n = 0.134$  to  $0.186$ ) for lower number of cycles (one or five). The value of 'n' however increases significantly when the number of cycles increase to ten ( $n = 0.26$  to  $0.27$ ).

A comparison of the effect of Type-II thermal-cycling treatment (a total of ten cycles) on the mechanical properties of the three starting materials are also included in Table 4.3. The U.T.S. values obtained in this case are not significantly different from the previous set. However, the ductility, as measured by percentage elongation values, is decidedly poorer here than in case of Type-I treatment. In addition, the 'n' values are also found to be much inferior (around 0.17) as compared to that of the corresponding starting materials which were subjected to the Type-I thermal-cycling treatment.

Figures 4.11 and 4.12 show the plots of true plastic stress ( $\sigma$ ) versus true plastic strain ( $\epsilon$ ) for all the thermally-cycled materials. The  $\ln \sigma$  and  $\ln \epsilon$  values were calculated at different points along these curves and these were plotted, one against the other, as shown in Figures 4.13 and 4.14. In all cases a single straight line could be seen to pass through most of the experimental data points. The slopes of these straight lines were carefully measured and the corresponding 'n' values noted down. These values are shown at appropriate places in Figures 4.13 and 4.14 and are also given in Table 4.3.

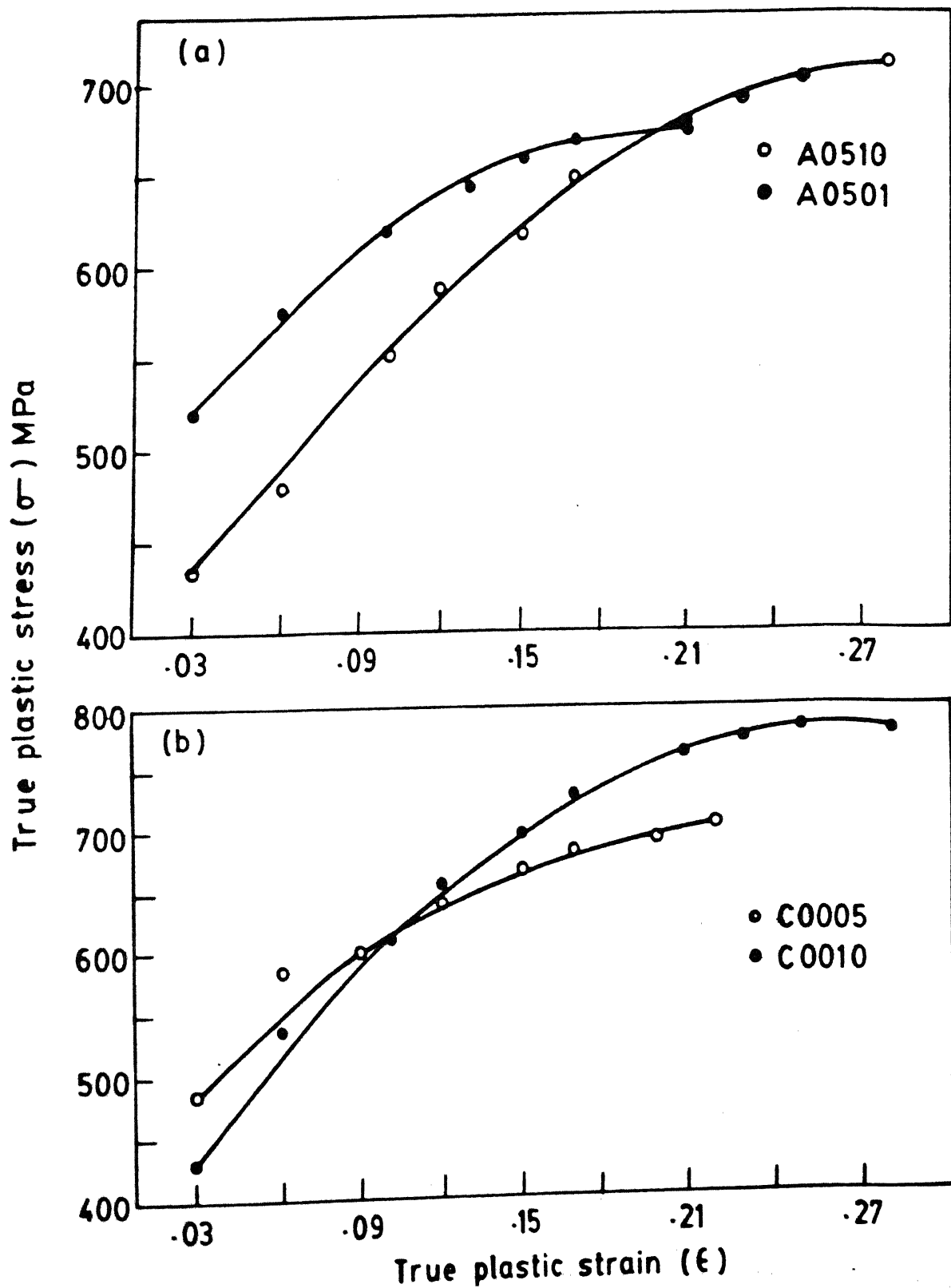


FIG. 4.11 PLOTS OF TRUE PLASTIC STRESS Vs. STRAIN

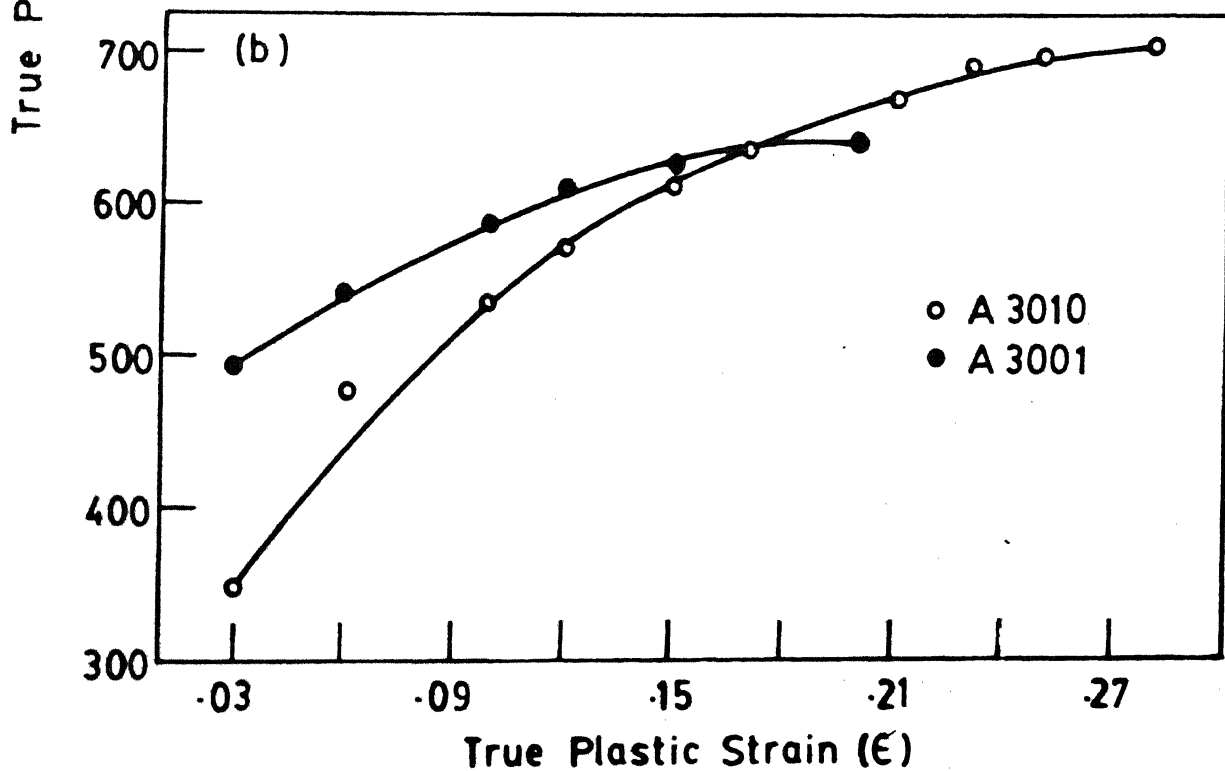
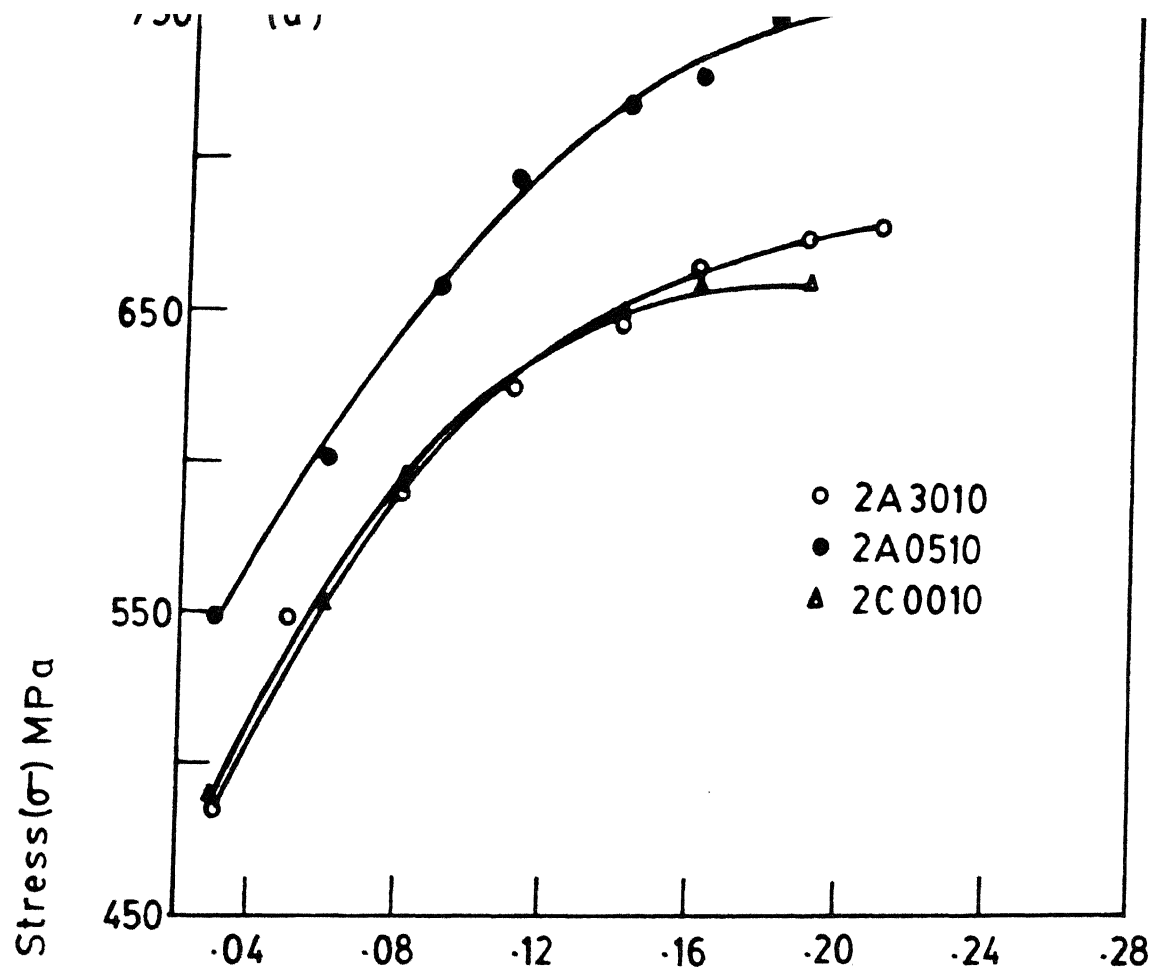


FIG. 4.12 PLOTS OF TRUE PLASTIC STRESS ( $\sigma$ ) Vs. STRAIN ( $\epsilon$ )



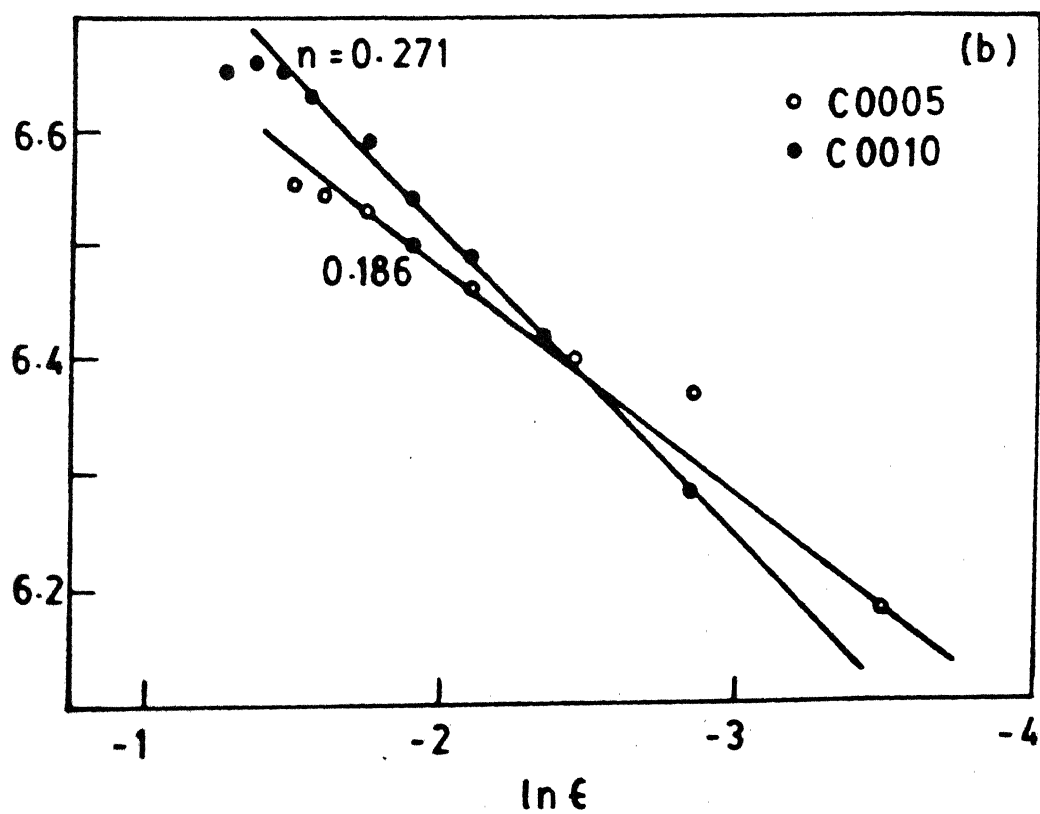
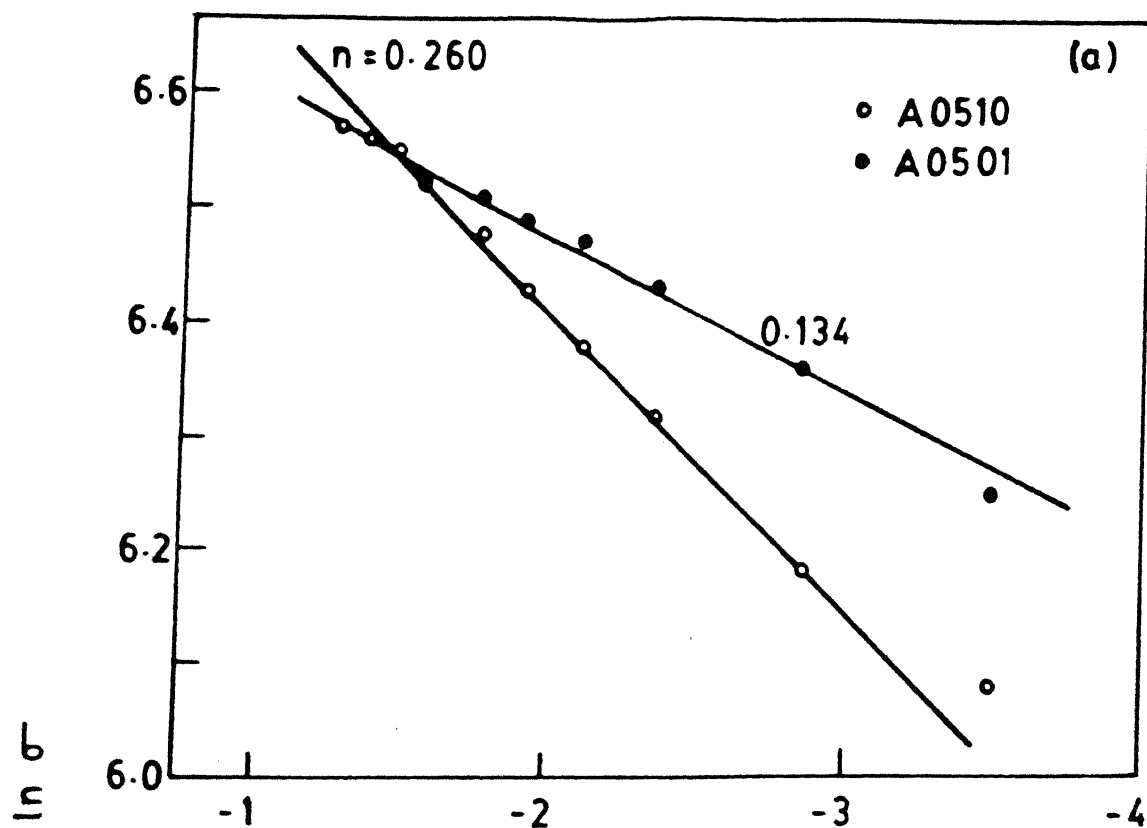


FIG. 4.13 PLOTS OF  $\ln \sigma$  Vs.  $\ln \epsilon$

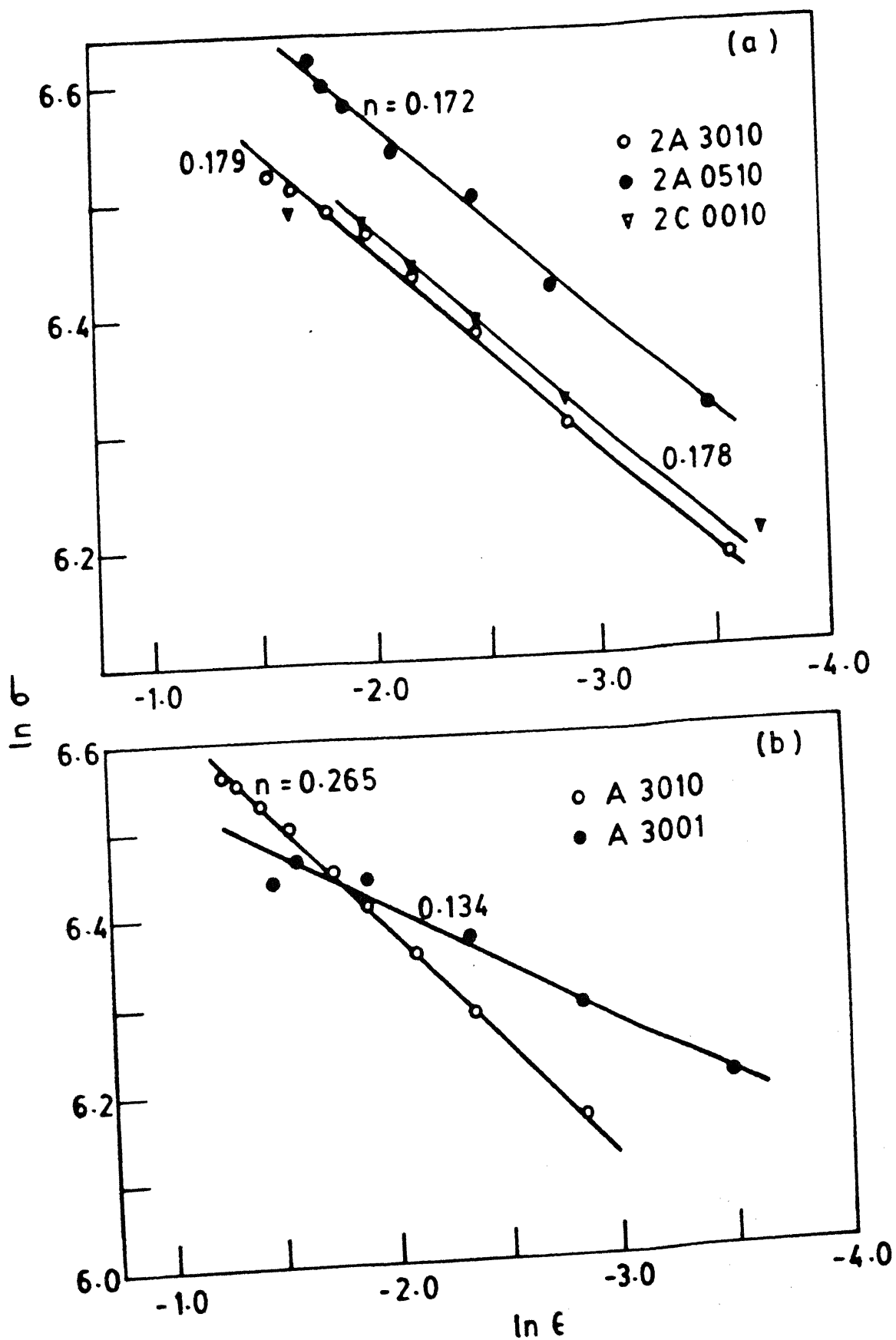


FIG. 4.14 PLOTS OF  $\ln \sigma$  vs.  $\ln \epsilon$

The  $\frac{d\sigma}{d\varepsilon}$  versus  $\varepsilon$  plots for the thermally cycled materials are given in Figures 4.15 and 4.16. A look at these figures immediately show that there is a common general feature in all the plots for the three starting materials subjected to the Type-I thermal-cycling treatment. For example, the plots for samples given the highest number of cycles (ten) always lie above the corresponding plots for lower number of cycles (one or five). Not only that, the former also starts at a much larger value of  $\frac{d\sigma}{d\varepsilon}$  indicating that the strain-hardening rate is much higher in them to start with. This higher rate is maintained all throughout with increasing value of  $\varepsilon$ .

Figure 4.16(b) shows that the  $\frac{d\sigma}{d\varepsilon}$  versus  $\varepsilon$  plots for all the three starting materials subjected to ten cycles of Type-II thermal-cycling treatment do not vary significantly one from the other. The rates of strain-hardening at any particular  $\varepsilon$ -value in this case are much lower than in case of the Type-I treatment.

#### 4.2.3 Study of Fractured Surfaces

Figures 4.17(a) to (f) show the S.E.M. fractographs taken from the fractured surfaces of tensile tested samples which were previously subjected to Type-I thermal-cycling treatment. Essentially ductile fracture, characterised by a profusion of dimples, are obtained for the initially cold-worked as well as the sample given dual-phasing treatment at 810°C for 5 minutes (Figures 4.19(a) to (d)). For both these materials, higher number of thermal-cycles produce a much finer and uniform distribution of the dimples than the corresponding ones given

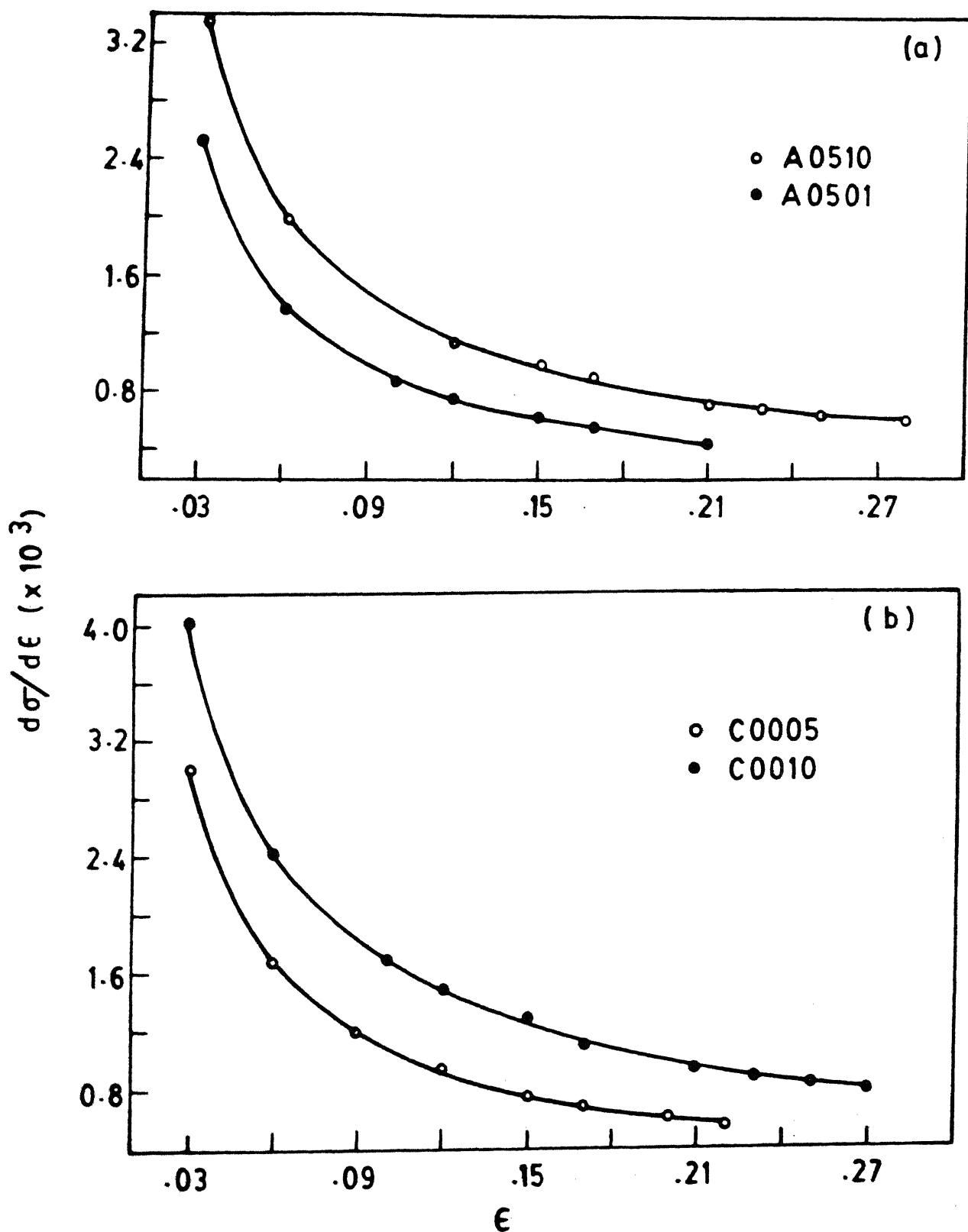


FIG. 4.15 RATE OF STRAIN HARDENING AS A FUNCTION OF TRUE STRAIN

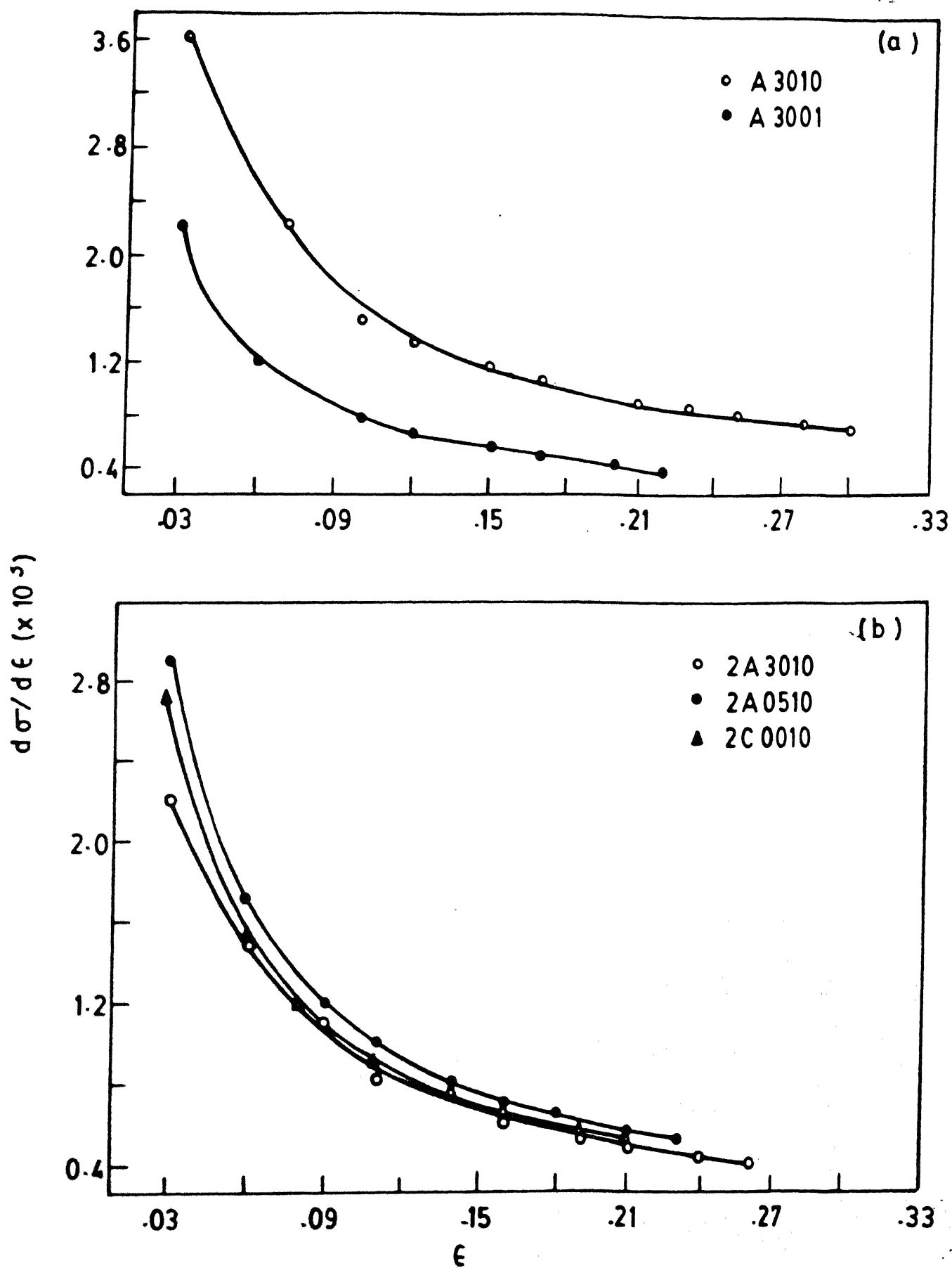
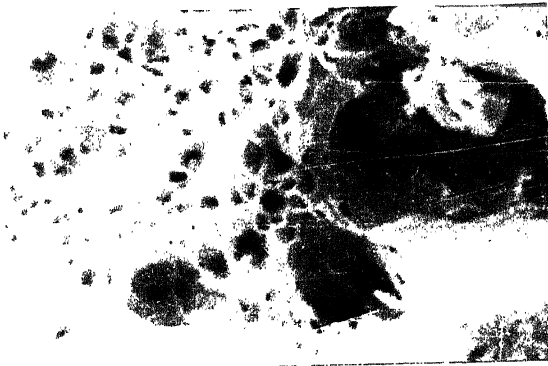
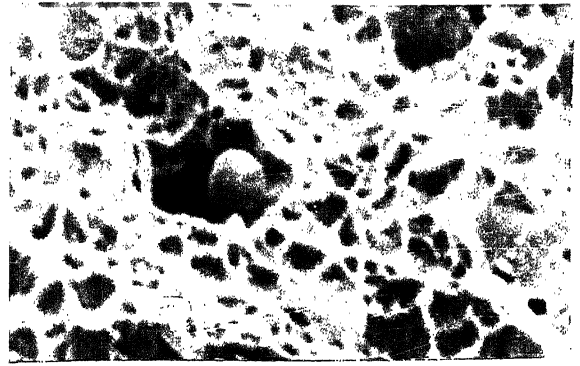


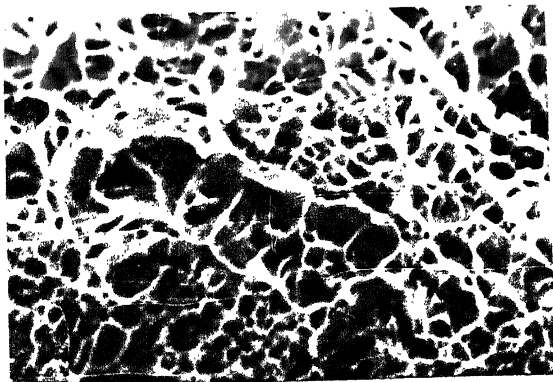
FIG. 4.16 RATE OF STRAIN HARDENING AS A FUNCTION OF



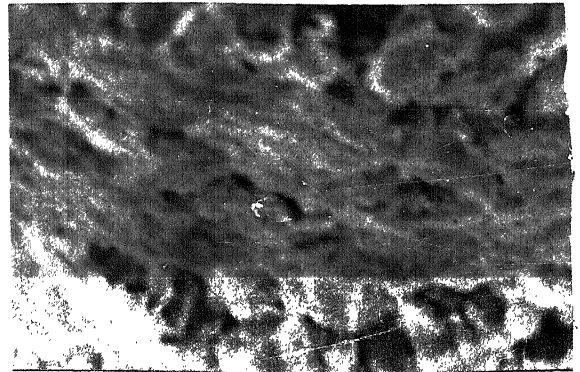
(a) (2000X)



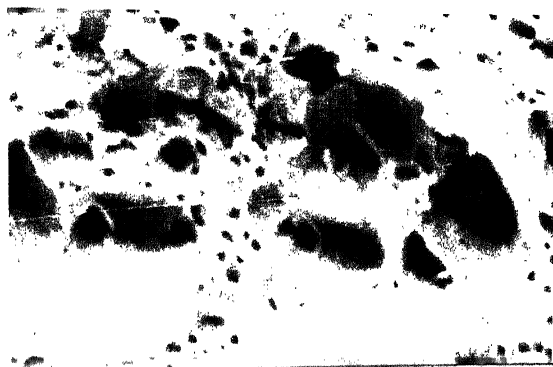
(b) (3000X)



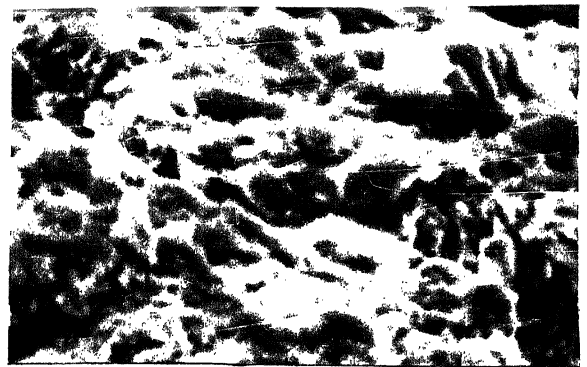
(c) (3000X)



(d) (4000X)

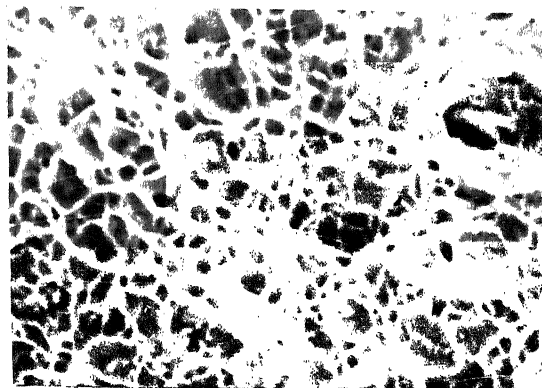


(e) (2500X)

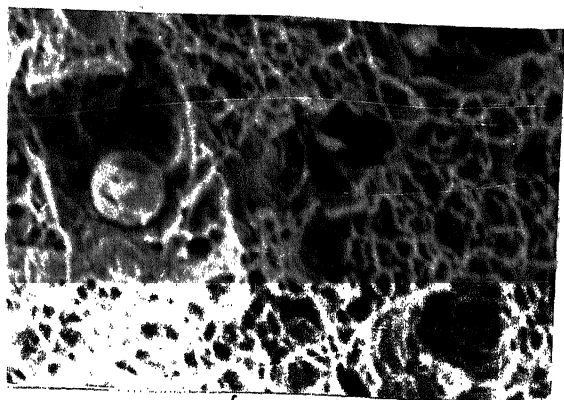


(f) (4000X)

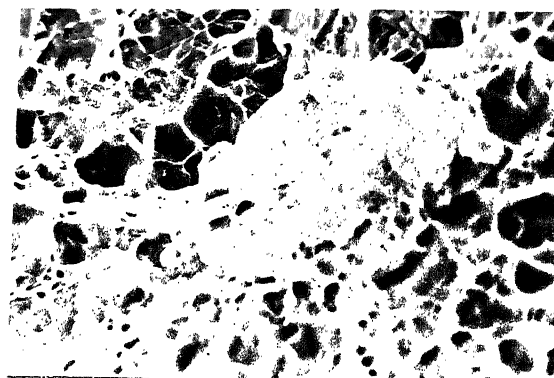
Fig. 4.17. S.E.M. fractographs of tensile samples prepared from Type-I thermally cycled materials: (a) C00 for 5 cycles (C0005); (b) C00 for 10 cycles (C0010); (c) A05 for 1 cycle (A0501); (d) A05 for 10 cycles (A0510); (e) A05 for 1 cycle (A0501); and (f) A30 for 10 cycles (A3010).



(a) (2000x)

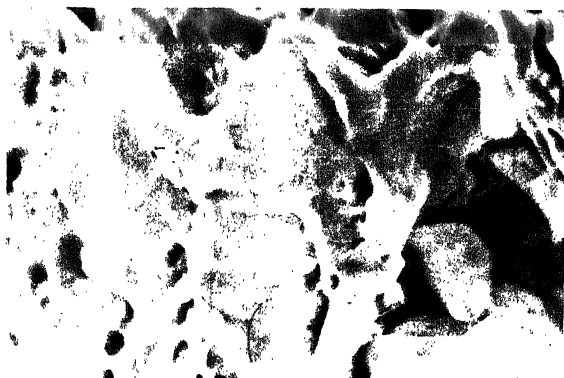


(b) (2000x)



(c) (4000x)

Fig. 4.18. S.E.M. fractographs of tensile samples prepared from Type-II thermally cycled materials: (a) 000 for 10 cycles (2C0010); (b) A05 for 10 cycles (2A0510); and (c) A30 for 10 cycles (2A3010).



(d) (5000x)

Fig. 4.18(d). S.E.M. fractograph showing a typical inclusion.

lower number of cycles. This indicates more refinement of the structural units as the number of cycles increase. Compared to the above, the fractographs of the thermally-cycled samples, with initial dual-phasing treatment at  $810^{\circ}\text{C}$  for 30 minutes, show a rather mixed fracture mode, characterised by fine dimples as well as cleavages (Figures 4.17(e) and (f)).

The S.E.M. fractographs from the fractured surfaces of samples subjected to Type-II thermal-cycling treatment (ten cycles) are presented in (Figures 4.18(a) to (c)). For the initial cold-worked sample, as well as the one subjected to dual-phasing treatment at  $810^{\circ}\text{C}$  for 5 minutes, the fracture surfaces are characterised by dimples of very fine size plus just a few cleavage facets (Figures 4.18(a) and (b)). The proportion of cleavage surfaces is much higher in the fractograph for the sample which was given dual-phasing treatment at  $810^{\circ}\text{C}$  for 30 minutes (Figure 4.18(c)). A fractured martensitic area can be seen lying at the centre of this photograph. Evidently, some amount of plastic deformation must have taken place before this martensitic area fractured.

In many of the fractographs, a number of inclusions could be observed. An attempt was made to identify these as far as practicable. A typical inclusion is shown in Figure 4.18(c) and the corresponding EDAX plot is presented in Figure 4.19. It is clear from this figure that the major constituent of this inclusion is vanadium. In all likelihood it is a carbide of vanadium since vanadium has a very strong affinity for carbon. Unfortunately, no carbon can be detected in the EDAX system.



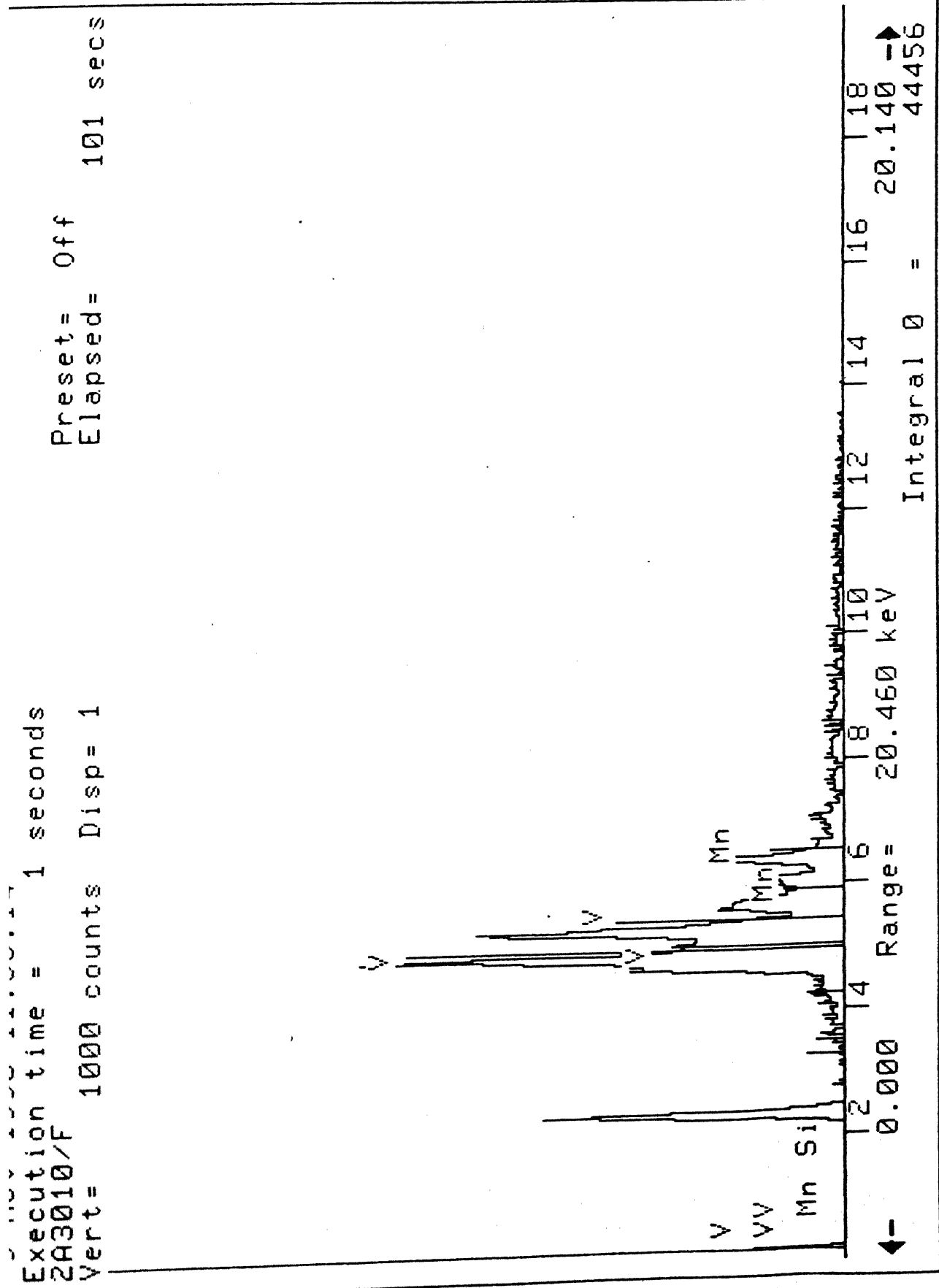


Fig. 4.19. EDAX plot of the inclusion shown in Fig. 4.18(e).

Mn and Si which are also present along with vanadium, may be occurring as substitutional solutes in the vanadium carbide.

### 4.3 Results of Texture Analysis

Figures 4.20(a) to (g) represent the (200) pole-figures from the texture of the various cold-worked and thermally-cycled materials. It is interesting to note that the textures of all these samples are remarkably similar.

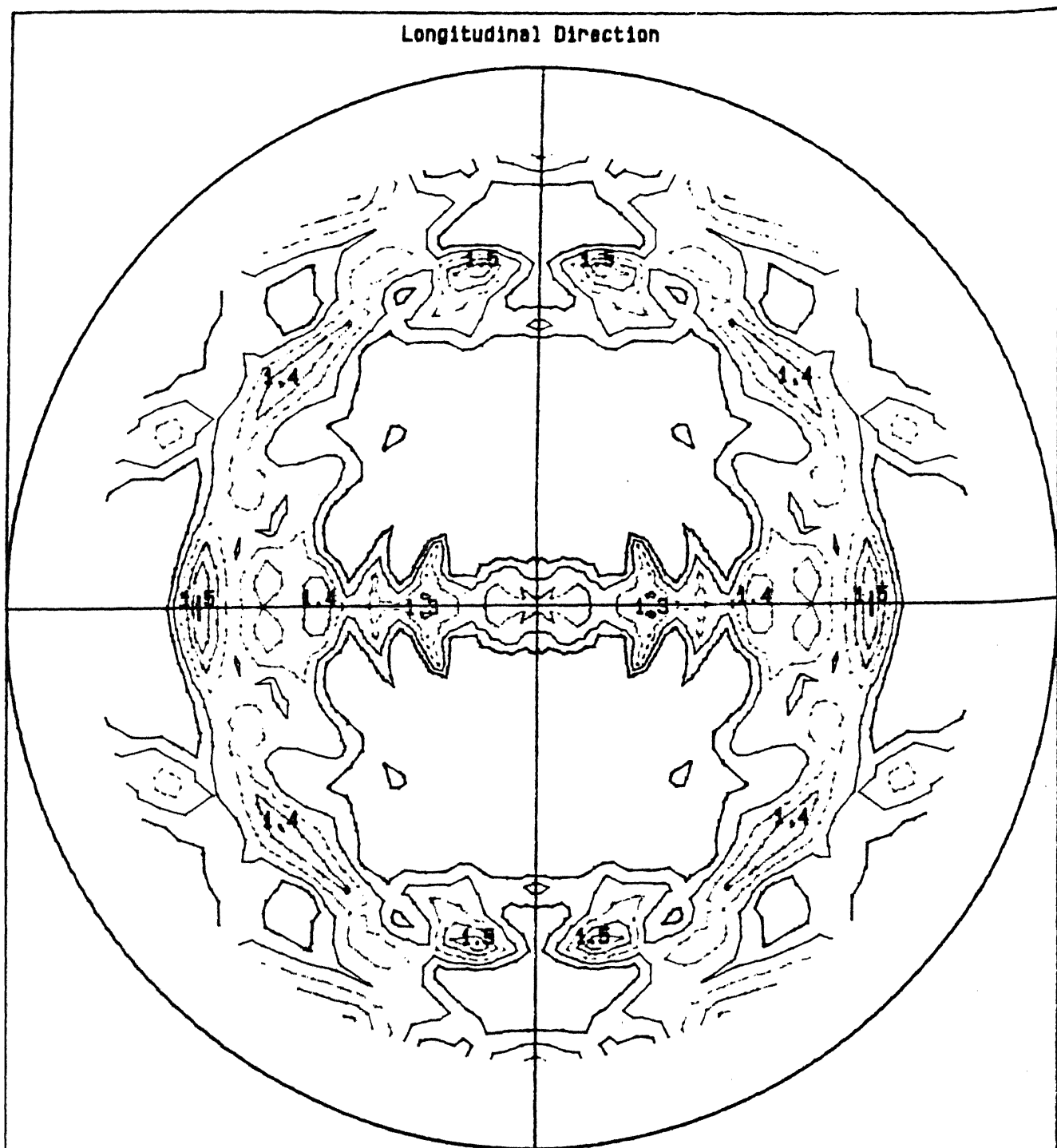
Figure 4.20(a) shows the (200) pole-figure from the 60% cold-rolled material. The texture is found to be rather weak here and consists of weak  $\{111\} \langle 112 \rangle$  and  $\{111\} \langle 110 \rangle$  components. In fact, the angular spread around the orientations is quite large, so that the components may also be described as consisting of  $\{112\} \langle 110 \rangle$  and  $\{113\} \langle 110 \rangle$ . In addition, few other components are also discernable. Overall, the texture in this sample is not very different from a random texture, the maximum intensity attained being only 1.6 times random.

Figure 4.21 shows a few ideal orientations plotted in a (200) pole-figure for identification of the components in the experimental samples.

A study of all the (200) plots clearly indicate that there has been practically no change in texture either on giving the dual-phase treatments to the samples or by thermal-cycling them subsequently.

Since O.D.F.'s offer a better resolution than pole-figures, a few O.D.F.'s were calculated from a number of experimental materials. These are shown in Figures 4.22(a) to (g).

Longitudinal Direction



200 Pole figure (Symmetrised x 4)

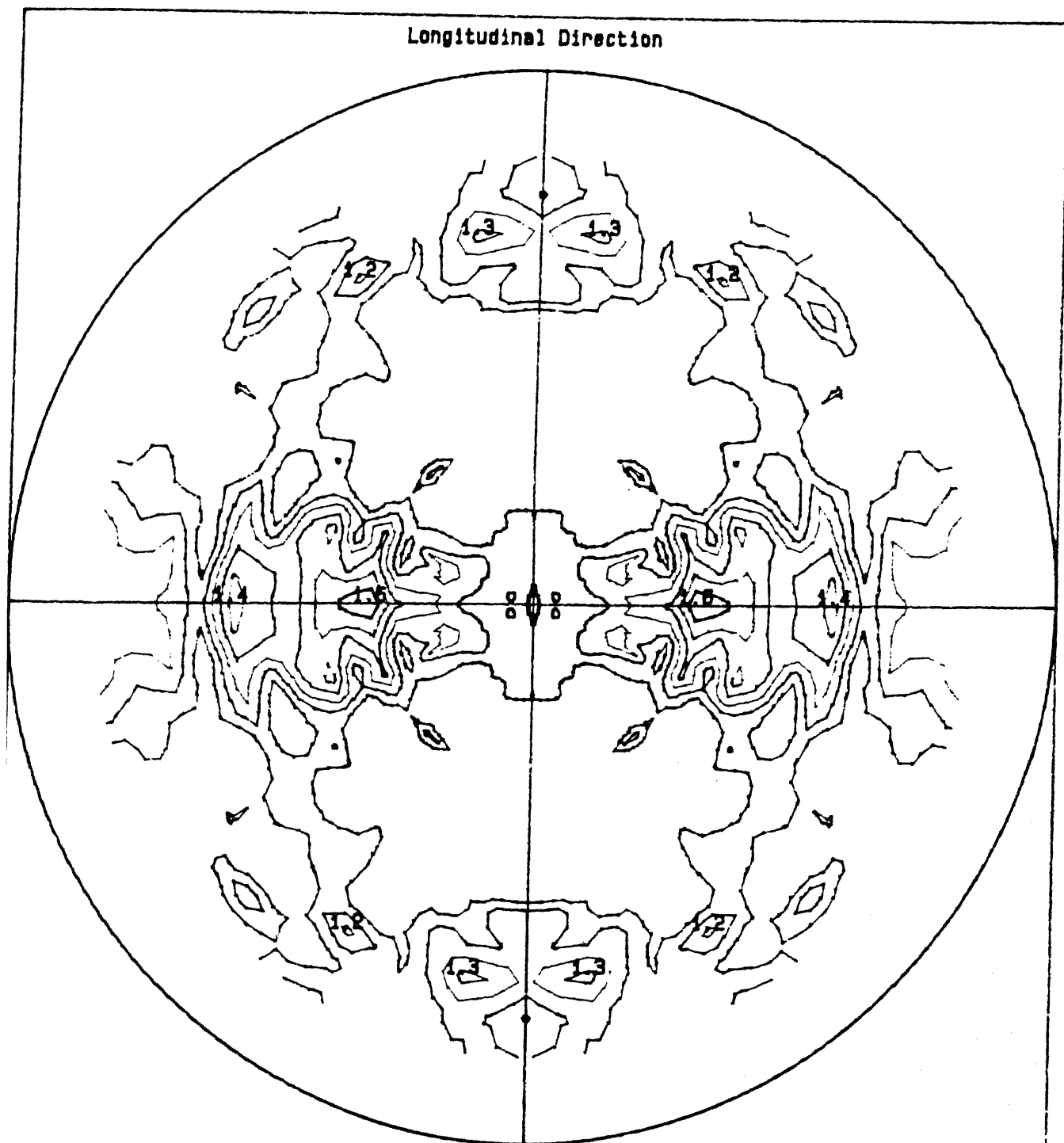
Fig. 4.20(a). (200) pole-figure of sample C0000.

SAMPLE: C0000  
IDENT.: RANJIT K.RAY.

DATE: 06-JUN-90 15:48

Contour levels: 1.00 1.10 1.20 1.30 1.40 1.50 1.60

SIEMENS \*TEX11\*



200 Pole figure (Symmetrised x 4)

Fig. 4.20(b). (200) pole-figure of sample C0010.

SAMPLE: C0010

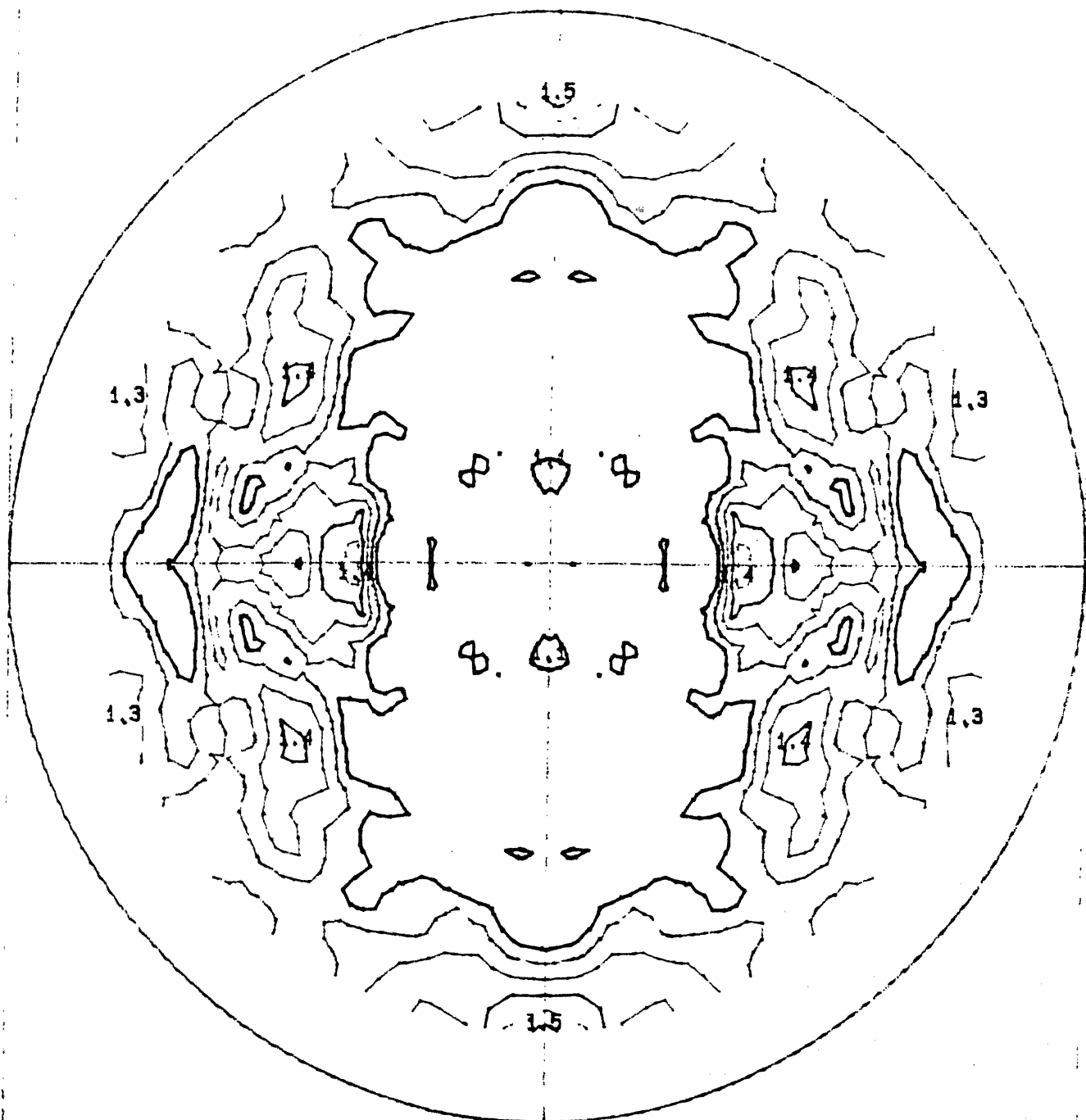
DATE: 10-AUG-90 11:01

IDENT.: RANJIT. K.RAY

Contour levels: 1.00 1.10 1.20 1.30 1.40 1.50 1.60

SIEMENS \*TEX11\*

Longitudinal Direction



200 Pole figure (Symmetrised x 4)

Fig. 4.20(c). (200) pole-figure of sample A0510.

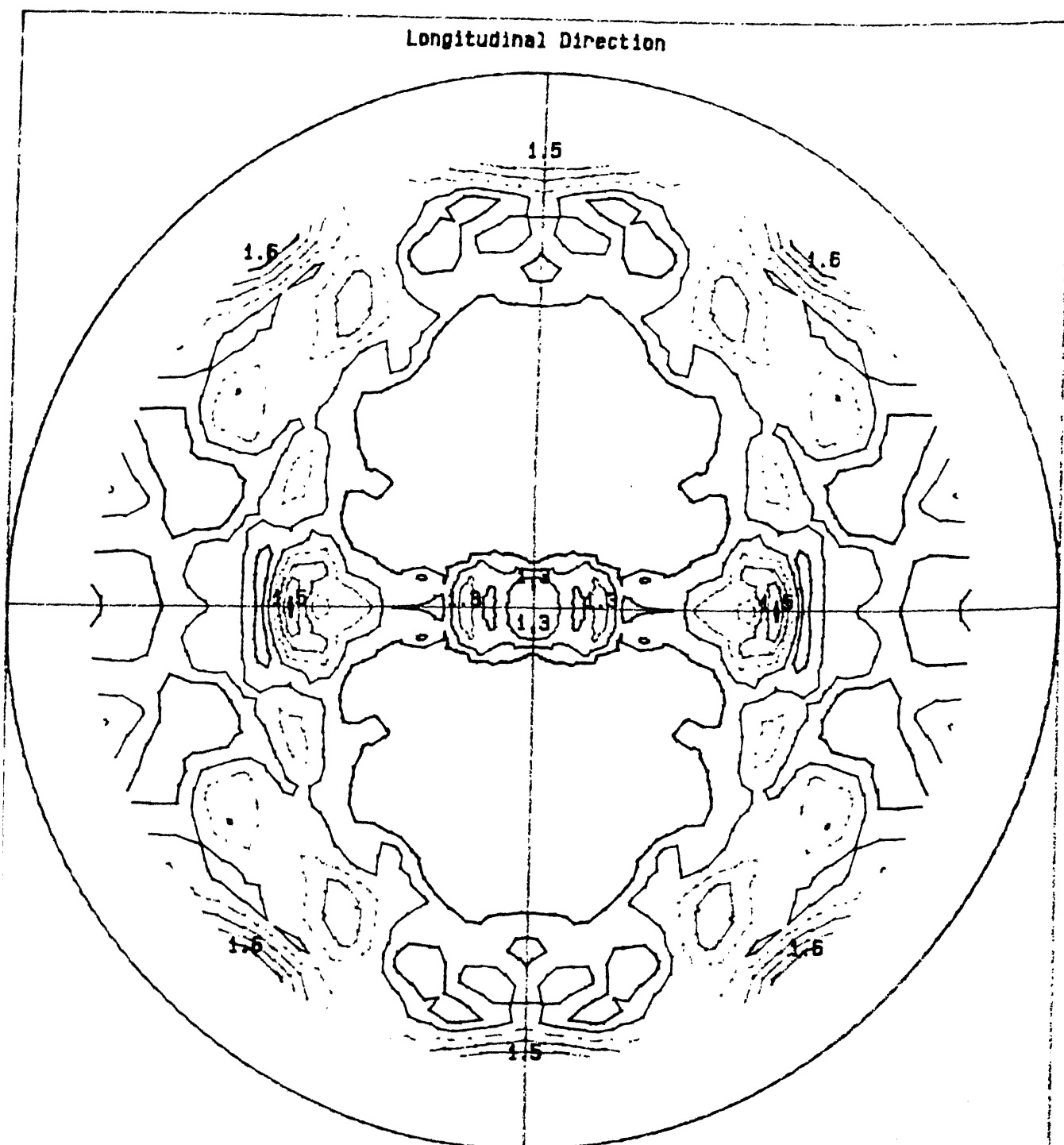
SAMPLE: A0510

DATE: 23-AUG-90 11:44

IDENT.: RANJIT. K.RAY

Contour levels: 1.00 1.10 1.20 1.30 1.40 1.50 1.60

SIEMENS \*TEX11\*



200 Pole figure (Symmetrised x 4)

Fig. 4.20(d). (200) pole-figure of sample A3010.

SAMPLE: A3010

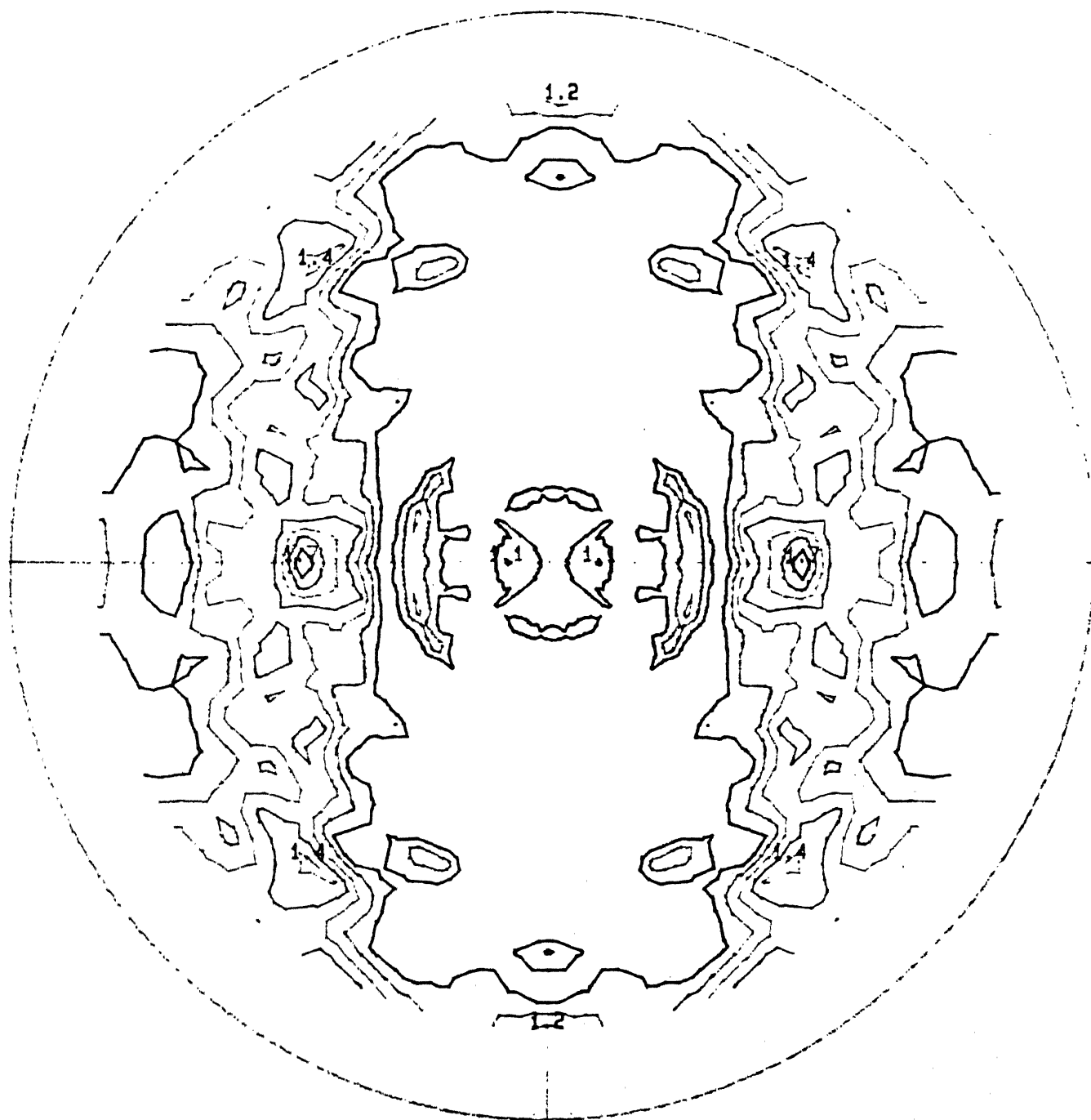
DATE: 13-JUN-90 09:56

IDENT.: RANJIT K.RAY.

Contour levels: 1.00 1.10 1.20 1.30 1.40 1.50 1.60

SIEMENS \*TEX11\*

Longitudinal Direction



200 Pole figure (Symmetrised x 4) Fig. 4.20(e). (200) pole-figure of sample 2C0010.

SAMPLE: 2C0010

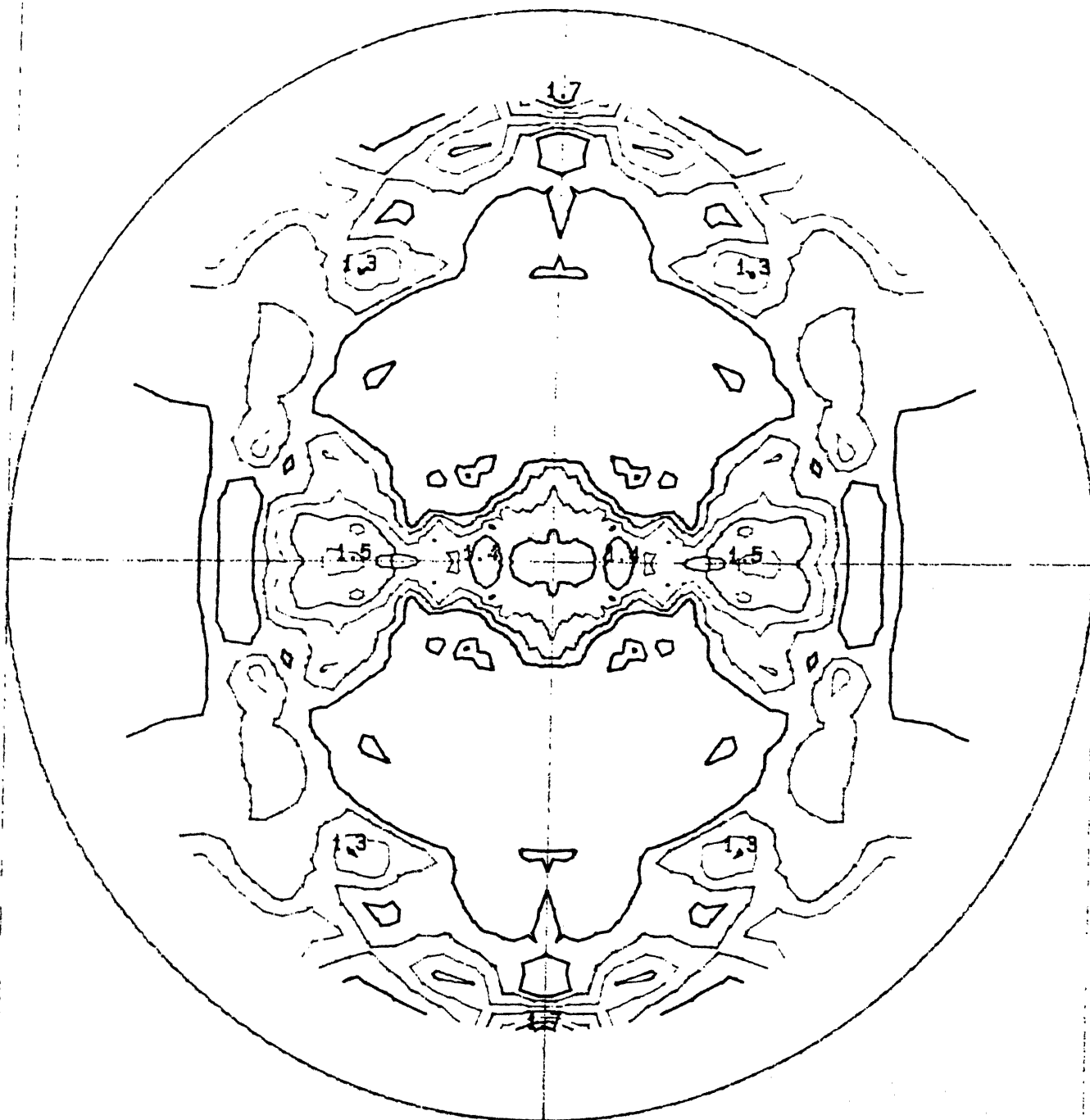
DATE: 20-AUG-90 12:15

IDENT.: RANJIT. K.RAY

Contour levels: 1.00 1.10 1.20 1.30 1.40 1.50 1.60

SIEMENS \*TEX11\*

Longitudinal Direction



200 Pole figure (Symmetrised x 4) Fig. 4.20(f). (200) pole-figure of sample 2A0510.

SAMPLE: 2A0510

DATE: 17-AUG-90 16:15

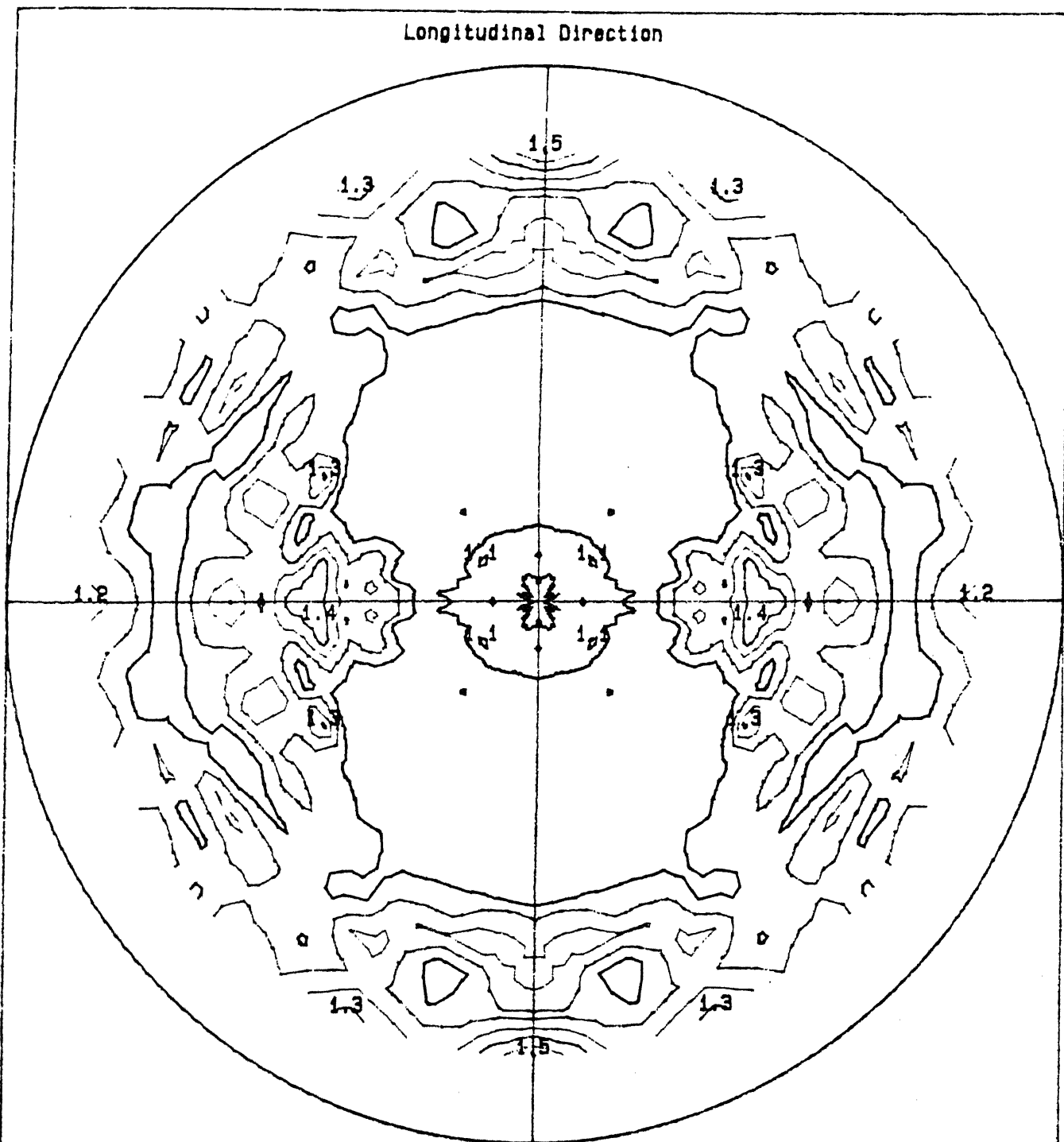
IDENT.: RANJIT. K.RAY

Contour levels: 1.00 1.10 1.20 1.30 1.40 1.50 1.60



SIEMENS \*TEX11\*

Longitudinal Direction



200 Pole figure (Symmetrised x 4) Fig. 4.20(g). (200) pole-figure of sample 2A3010.

SAMPLE: 2A3010

DATE: 14-AUG-90 17:22

IDENT.: RANJIT. K.RAY

Contour levels: 1.00 1.10 1.20 1.30 1.40 1.50 1.60

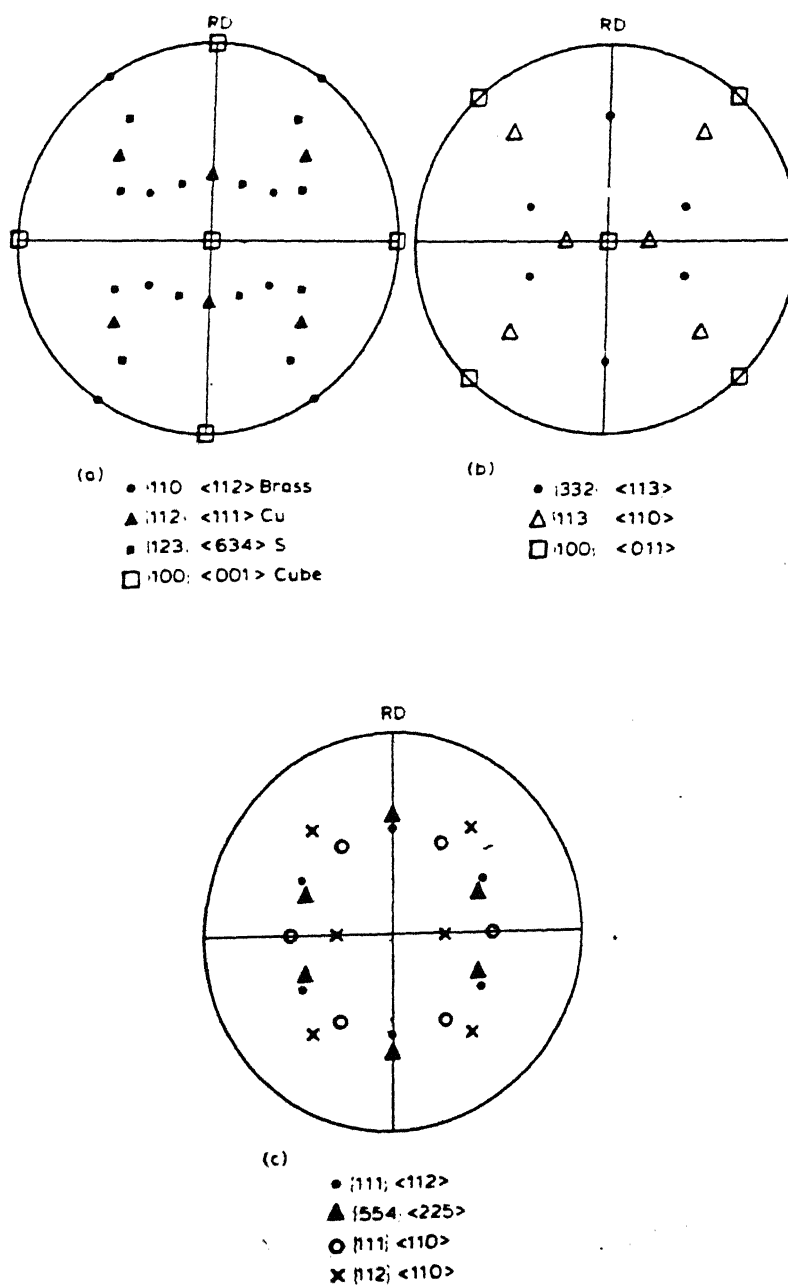


Fig. 4.21. (200) pole-figures showing some ideal orientations in steels.

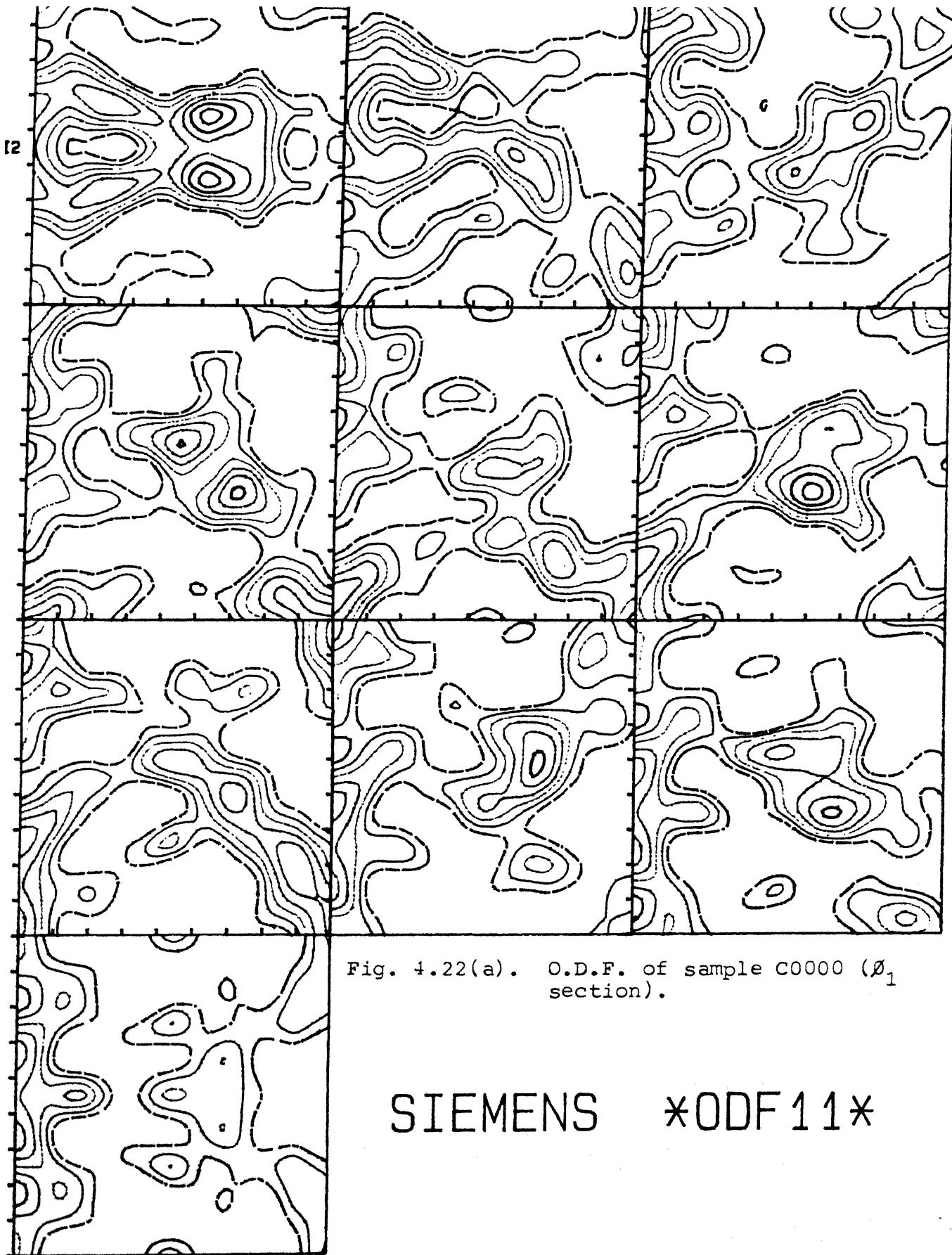


Fig. 4.22(a). O.D.F. of sample C0000 ( $\emptyset_1$  section).

SIEMENS \*ODF11\*

SAMPLE: C0000

CONST. ANGLE: PHI1 = 00, 90, 10

LMAX = 22; MAX FN HT = 3.61; TSP = 0.76; J INDEX = 1.29

CONTINUED 1 0 1 1 1 0 2 2 2 6 3 0 3 1

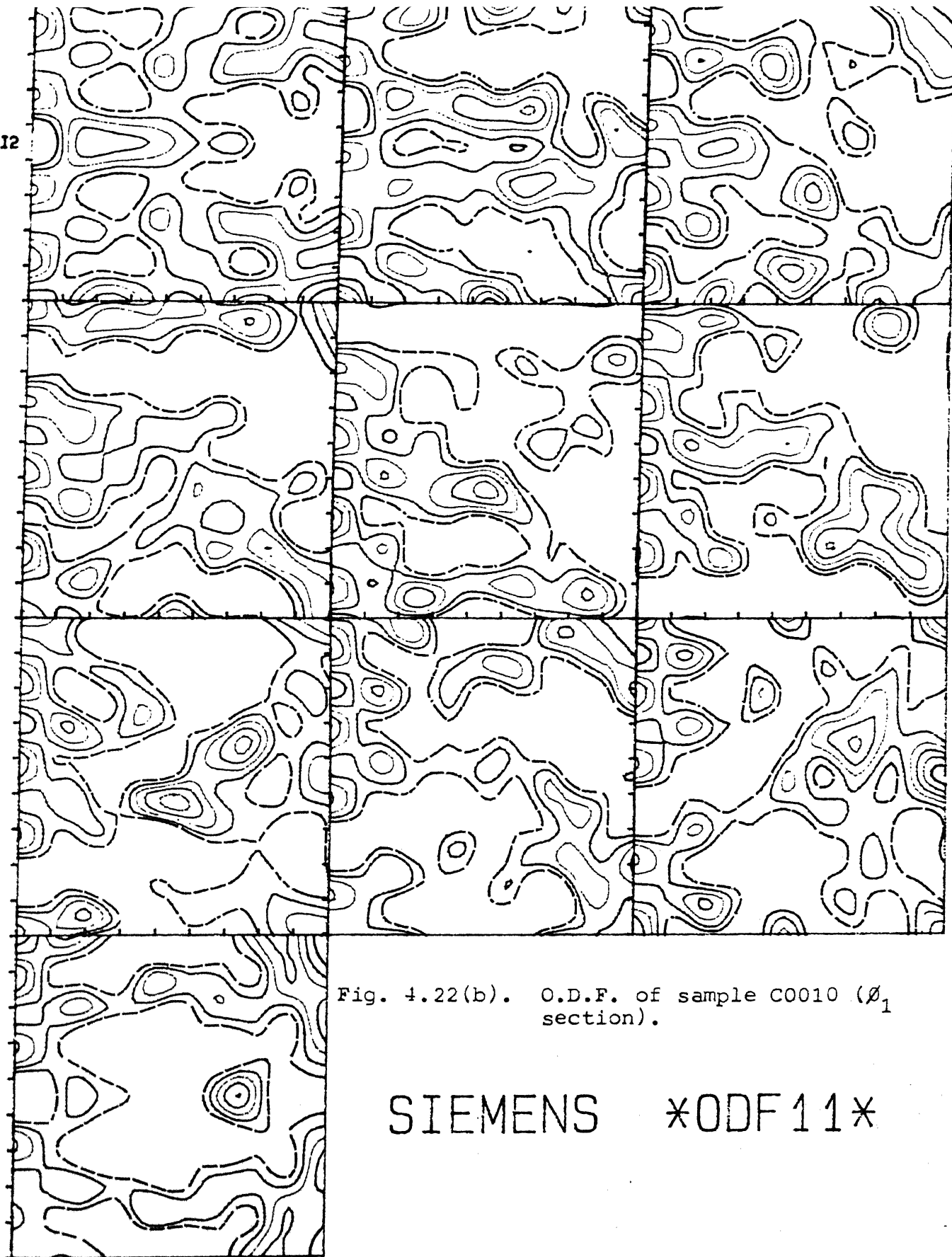


Fig. 4.22(b). O.D.F. of sample C0010 ( $\emptyset_1$  section).

SIEMENS \*ODF11\*

SAMPLE: C0010

CONST. ANGLE: PHI1 = 00, 90, 10

LMAX = 22; MAX FN HT = 2.71; TSP = 0.51; J INDEX = 1.14

CONTOURS: 1.0 1.3 1.6 1.9 2.2 2.5.

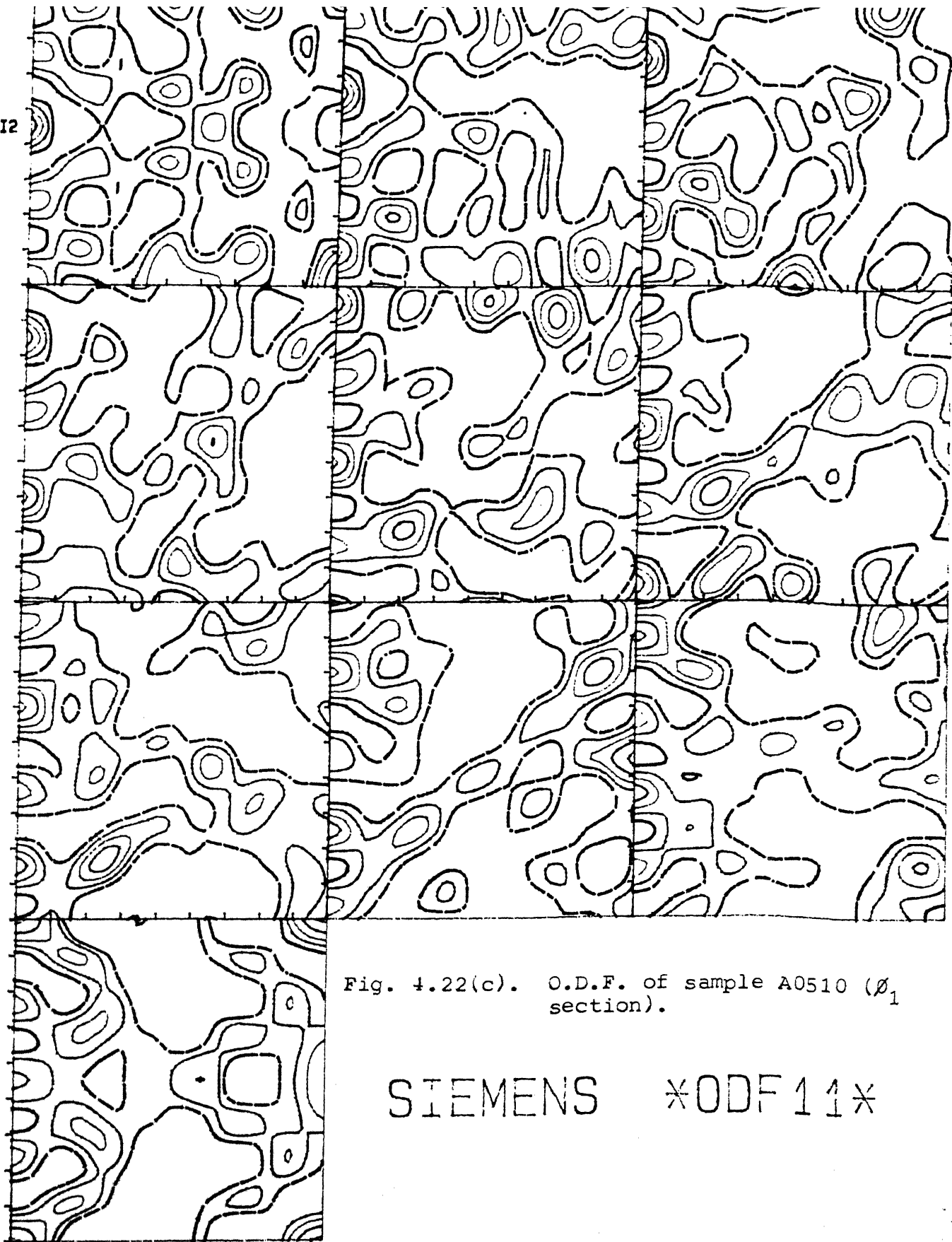


Fig. 4.22(c). O.D.F. of sample A0510 ( $\phi_1$  section).

SIEMENS \*ODF11\*

SAMPLE: A0510      CONST. ANGLE: PHI1 = 00, 90, 10  
LMAX = 22; MAX FN HT = 2.29; TSP = 0.38; J INDEX = 1.08  
CONTOURS: 1.0, 1.3, 1.6, 1.9, 2.2.

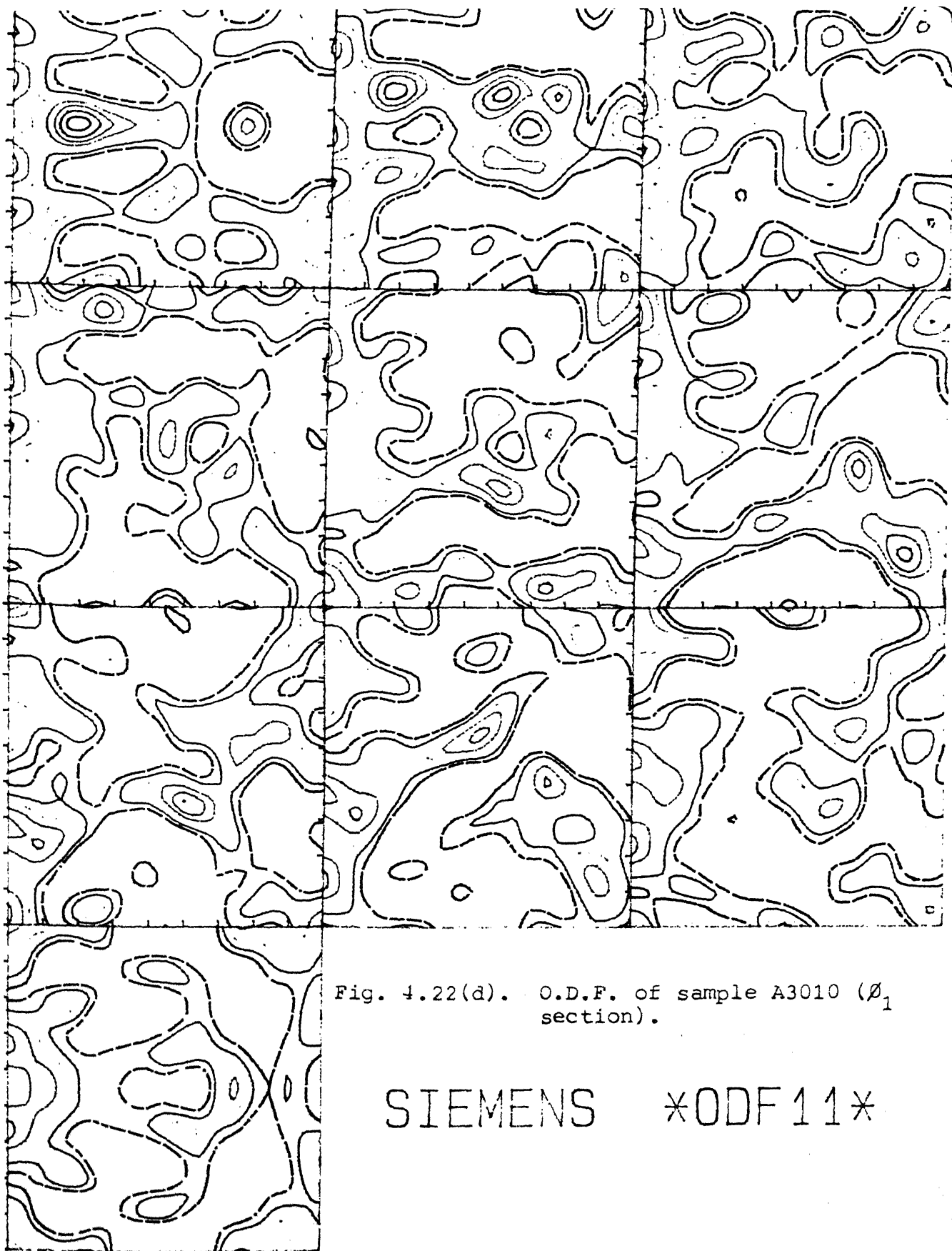


Fig. 4.22(d). O.D.F. of sample A3010 ( $\phi_1$  section).

SIEMENS \*ODF11\*

SAMPLE: A3010

CONST. ANGLE: PHI1 = 00, 90, 10

LMAX = 22; MAX FN HT = 3.58; TSP = 0.71; J INDEX = 1.25

CONTOURS: 1.0, 1.4, 1.8, 2.2, 2.6, 3.0, 3.4,

Fig. 4.22(e). O.D.F. of sample 2C0010  
( $\theta_1$  section).

SIEMENS \*ODF11\*

SAMPLE: 2C0010

CONST. ANGLE: PHI1 = 00, 90, 10

LMAX = 22; MAX FN HT = 2.47; TSP = 0.50; J INDEX = 1.13

CONTOURS: 1.0, 1.3, 1.6, 1.9, 2.2,

PHI2

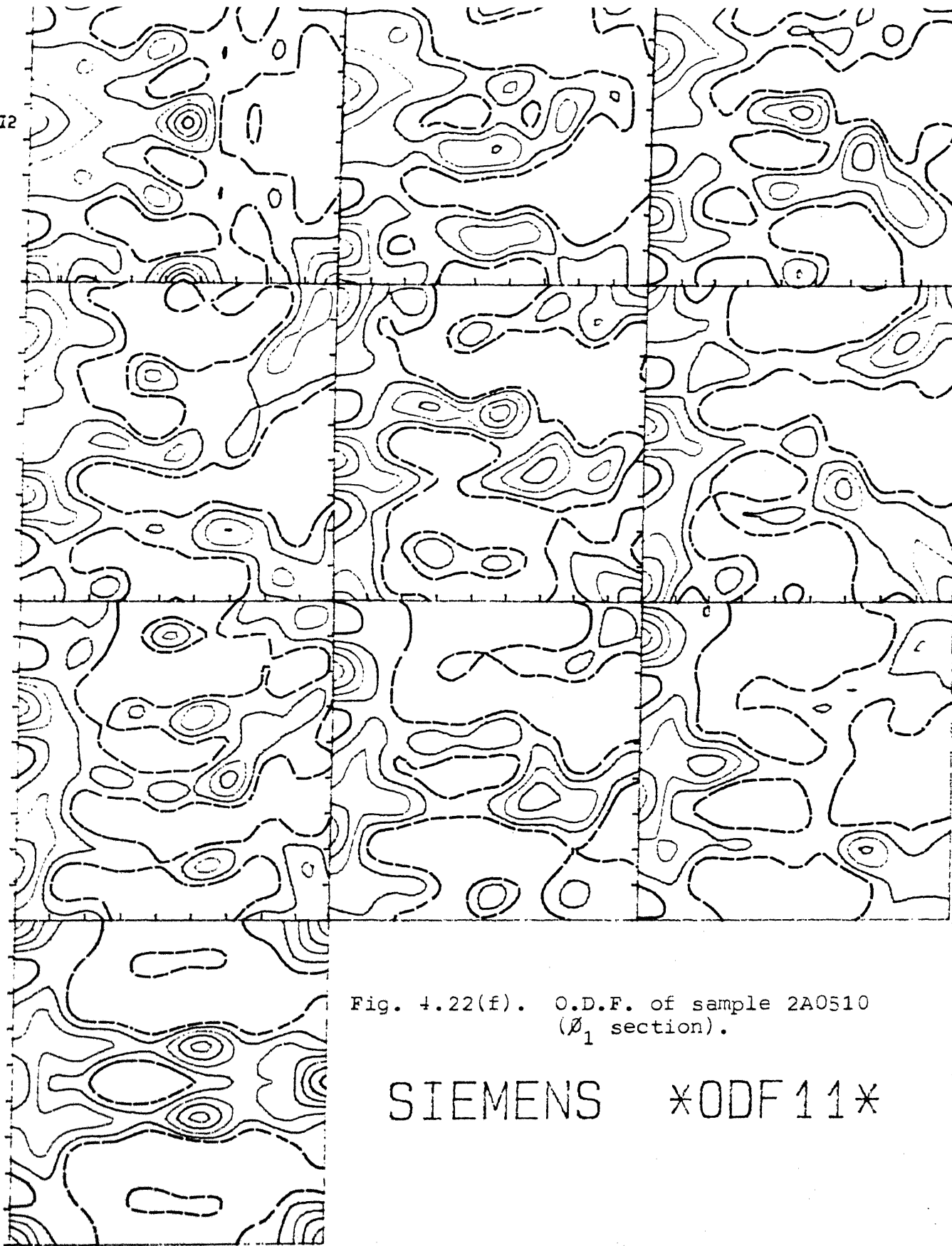


Fig. 4.22(f). O.D.F. of sample 2A0510  
( $\varnothing_1$  section).

SIEMENS \*ODF11\*

SAMPLE: 2A0510

CONST. ANGLE: PHI1 = 00, 90, 10

LMAX = 22; MAX FN HT = 3.56; TSP = 0.60; J INDEX = 1.18

CONTOURS: 1.0, 1.4, 1.8, 2.2, 2.6, 3.0, 3.4.



PHI2

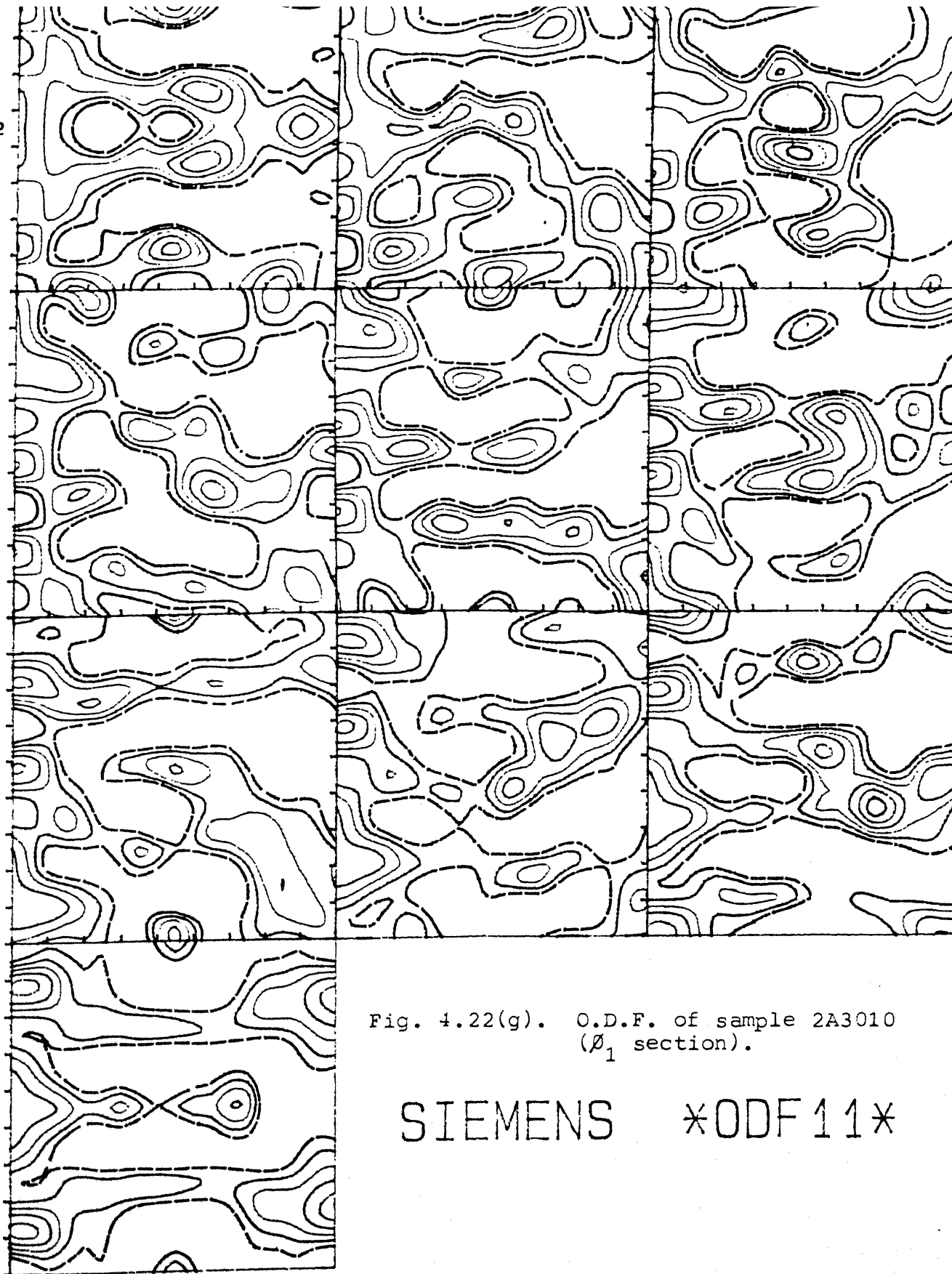


Fig. 4.22(g). O.D.F. of sample 2A3010  
( $\phi_1$  section).

SIEMENS \*ODF11\*

SAMPLE: 2A3010

CONST. ANGLE: PHI1 = 00, 90, 10

LMAX = 22; MAX FN HT = 2.68; TSP = 0.59; J INDEX = 1.17

CONTOURS: 1.0, 1.3, 1.6, 1.9, 2.2, 2.5,

The  $\{hkl\} \langle uvw \rangle$  values corresponding to the  $\phi_1$ ,  $\phi$ ,  $\phi_2$  values for the maxima in all these O.D.F.'s were found out [82]. These orientations are shown typically for the cold-worked material in Table 4.4.

Some ideal orientations along with the corresponding  $\phi_1$ ,  $\phi$ ,  $\phi_2$  values are also shown in Table 3.4 for ready reference.

Although there are variations in the type and nature of orientations present in the O.D.F.'s of the different samples, the differences are only minor since the intensity values of most of them are rather low. In addition to peak type components no fibre components could be observed in any of the above.

There is essentially no difference in texture as a function of the type of thermal-cycling performed.

Table 4.4

Orientation maxima in the O.D.F. of the cold-worked material

SAMPLE : C0000									
$\phi_1$	$\phi$	$\phi_2$	h	k	l	u	v	w	Ideal $\phi_1, \phi, \phi_2$
0	2	18	-	-	-	-	-	-	-
0	2	58	-	-	-	-	-	-	-
0	21	33	2	3	10	3	$\bar{2}$	0	(0, 20, 34)
0	2	33	-	-	-	-	-	-	-
0	21	58	3	2	10	2	$\bar{3}$	0	(0, 20, 56)
0	51	37	3	4	4	4	$\bar{3}$	0	(0, 51, 37)
0	51	53	9	7	9	7	$\bar{9}$	0	(0, 52, 52)
10	2	47	-	-	-	-	-	-	-
10	13	18	1	3	9	12	$\bar{7}$	1	(13, 19, 18)
10	51	47	6	5	6	4	$\bar{6}$	1	(10, 52, 50)
10	86	80	9	1	1	1	$\bar{11}$	2	(10, 84, 84)
20	2	37	-	-	-	-	-	-	-
20	5	10	0	1	6	12	$\bar{6}$	1	(2, 7, 90)
20	15	37	2	3	12	6	$\bar{8}$	1	(20, 17, 34)
20	45	50	4	3	6	3	$\bar{8}$	2	(21, 40, 53)
20	65	37	4	5	3	10	$\bar{11}$	5	(21, 65, 39)
30	21	26	0	0	1	7	$\bar{12}$	0	(30, 0, 30)
30	8	88	1	0	7	$\bar{7}$	$\bar{12}$	1	(31, 8, 90)
30	45	40	8	9	12	6	$\bar{12}$	5	(30, 45, 42)
30	62	54	9	6	5	4	$\bar{11}$	6	(30, 65, 56)
30	86	2	1	11	1	7	$\bar{1}$	4	(30, 85, 5)
30	80	86	11	2	1	1	$\bar{8}$	5	(32, 85, 80)

contd...

Table 4.4 (continued)

$\phi_1$	$\phi$	$\phi_2$	h	k	l	u	v	w	Ideal $\phi_1, \phi, \phi_2$
40	2	16	-	-	-	-	-	-	-
40	3	82	1	0	10	$\overline{10}$	$\overline{12}$	1	(40, 6, 90)
40	50	45	6	6	7	3	$\overline{10}$	6	(40, 50, 45)
40	68	62	9	5	4	1	$\overline{5}$	4	(41, 69, 61)
40	90	90	1	0	0	0	$\overline{6}$	5	(40, 90, 90)
40	90	0	0	1	0	6	0	5	(40, 90, 0)
50	1	6	0	1	12	10	$\overline{12}$	1	(50, 5, 0)
50	3	73	-	-	-	-	-	-	-
50	10	30	2	3	11	1	$\overline{8}$	2	(51, 18, 34)
50	51	53	4	3	4	0	$\overline{4}$	3	(50, 51, 53)
50	57	35	7	10	8	4	$\overline{10}$	9	(50, 59, 35)
50	90	0	0	1	0	5	0	6	(50, 90, 0)
50	90	90	1	0	0	0	$\overline{5}$	6	(50, 90, 90)
60	0	0	0	1	12	7	$\overline{12}$	1	(60, 5, 0)
60	2	63	0	0	1	$\overline{7}$	$\overline{11}$	0	(61, 0, 61)
60	2	87	1	0	12	$\overline{12}$	$\overline{7}$	1	(60, 5, 90)
60	12	20	1	2	10	0	$\overline{5}$	1	(64, 13, 27)
60	62	51	6	5	4	0	$\overline{4}$	5	(61, 63, 50)
60	80	71	9	3	1	1	$\overline{7}$	12	(60, 84, 72)
60	90	3	0	1	0	7	0	12	(60, 90, 0)
70	2	53	1	1	12	$\overline{4}$	$\overline{8}$	1	(72, 7, 45)
70	2	46	0	0	1	$\overline{3}$	$\overline{2}$	0	(73, 0, 73)
70	62	40	4	4	3	$\overline{1}$	$\overline{8}$	12	(70, 62, 45)
80	2	43	1	1	12	$\overline{5}$	$\overline{7}$	1	(81, 7, 45)
80	2	67	-	-	-	-	-	-	-
80	43	38	5	7	9	$\overline{2}$	$\overline{5}$	5	(80, 44, 36)
80	59	56	11	7	8	$\overline{4}$	$\overline{4}$	9	(83, 58, 58)
80	82	86	9	1	1	$\overline{1}$	$\overline{2}$	11	(80, 84, 84)
90	2	33	1	1	11	$\overline{11}$	$\overline{11}$	2	(90, 7, 45)
90	2	56	-	-	-	-	-	-	-

## CHAPTER V

### Discussions

The optical microstructures generated by subjecting the initial starting materials to Type-II thermal-cyclic treatment [see Figures 4.5(a) to (c)] and their corresponding grain size distributions [Figure 4.10] reveal no difference in grain size even after ten cycles were given. When Figure 4.10 is studied it is obvious that the behaviour of the three initial starting materials remain essentially the same. The optical microstructures [Figures 4.3(a), (b), (e) and (f)] produced by subjecting the cold-worked material and the dual-phase aggregate (got by 30 minutes annealing at  $810^{\circ}\text{C}$ ) to Type-I thermal-cycling treatment show no significant grain refinement with the increase in the number of cycles. This fact is also supported by Figures 4.7 and 4.9. But significant refining in grain size with the increase in the number of cycles from one to ten is visible in case of structures produced by treating the initial dual-phase material (got by annealing at  $810^{\circ}\text{C}$  for 5 minutes) to the Type-I thermal-cyclic treatment [Figure 4.8]. The optical microstructures of the just-mentioned thermal-cycled materials shown in Figures 4.3(c) and (d) also show this marked refinement.

Thus, while studying the effect of thermal-cycling on the grain refinements as obtained by Type-I and Type-II thermal-cycling treatments, it is noticed that there is no significant

difference between the two types of cycles excepting in the case of the initial dual-phase aggregate got by annealing the cold-worked material at  $810^{\circ}\text{C}$  for 5 minutes. From the results got, it can be said that the best thermal-cycling treatment for grain refinement is the Type-I thermal-cyclic treatment. This gives the best grain refinement when applied to the initial dual-phase material got by subjecting the 60% cold-deformed material to 5 minutes annealing in the intercritical temperature range ( $810^{\circ}\text{C}$ ). The optimum grain refinement as obtained with the above specifications is achieved by ten numbers of cycles.

According to S.S. D'yachenko and co-workers [62], repeated heating and cooling in the temperature range between  $A_{e1}$  and  $A_{e3}$  causes a change in the ratio of phases in steel quenched after thermal-cycling as compared with heating and cooling only once. Also, as the number of cycles is increased, the quantity of martensite diminishes, the extent of this increasing with heating into the upper part of the intercritical temperature range. One of the reasons for this reduction as stated by them is a decrease in austenite stability. From Table 4.1 it is seen that this trend is followed by the initial dual-phase structures subjected to Type-I thermal-cyclic treatment but not the initial cold-worked material. The martensite volume fraction of the thermally cycled structures generated by Type-II thermal-cyclic treatment are seen to be on the higher side for all the initial starting materials. Actually, the nature of evolution of the microstructure during thermal-

cycling is not very clear and needs further systematic study. The problem becomes all the more difficult when the starting material has a duplex microstructure. This is specially true when the microconstituents are not totally independent of one another, but interdependent as in case of the dual-phase steels.

The deformation behaviour of the thermally cycled materials have been studied and the results tabulated in Table 4.3. After thermal-cycling, the steels are essentially having a dual-phase structure - soft ferrite and hard martensite. During tensile deformation of such a material, the initial load is taken up by the soft phase which plastically deforms, after some initial strain the load gets transferred to the hard phase which then starts deforming. A point is reached when the hard phase, whose deformability is less than the soft phase, can no longer sustain the load and fails. The overall stress at that stage is sufficiently high. So when the particles of the hard phase breakdown, the surrounding soft phase can no longer sustain this load and therefore there is a catastrophic failure of the material after that [56].

On the basis of the above deformation model, it is not difficult to realise that the initial work-hardening rate for such a material will essentially depend on the characteristics of the soft ferrite phase, specially its strength. It is known that when a steel sample is kept within the  $(\alpha + \gamma)$  intercritical temperature range, there is partitioning of some of the elements to the  $\alpha$  and some to the  $\gamma$  phase. The present steel contains about 0.5% Si. Now, Si is a known ferrite stabiliser

and partitions to the ferrite phase when kept in the  $(\alpha + \gamma)$  range [28]. The Type-I thermal-cycling treatment essentially consists of heating in the  $(\alpha + \gamma)$  range, quenching, heating again to the same temperature in the  $(\alpha + \gamma)$  range. Therefore, more number of cycles in the  $(\alpha + \gamma)$  range will lead to a greater chance for the Si and other elements to partition into the ferrite and austenite (martensite) phases. So, amount of Si present in the ferrite will increase as the number of cycles increases. As a result, the ferrite will be stronger and therefore the strain-hardening will be more in this case than in case of ferrite with a lower amount of the substitutional solute Si, obtained after a lower number of cycles. This is reflected in the higher 'n'-values obtained for the materials subjected to the larger number of cycles (Table 4.3).

The 'n'-values obtained in materials subjected to the Type-II thermal-cycling treatment (same number of cycles) are quite low as compared to the corresponding materials given by the Type-I thermal-cycling treatment. This is not surprising since in Type-II treatment the first half of any cycle consists of austenitizing. Therefore, even if there has been a partitioning of Si amongst  $\alpha$  and  $\gamma$  in the second half of the previous cycle (due to heating in the intercritical range), that effect gets removed during the first half of the next cycle. As a result of this the ferrite does not get the chance of accumulating sufficient amount of Si at any stage to provide sufficient strengthening. This results in a poor value of 'n'.



The above reasoning also explains the behaviour of the  $\frac{d\sigma}{d\varepsilon}$  versus  $\varepsilon$  plots as a function of type and cycle of thermal-cycling treatment.

The U.T.S. (Table 4.3) is found to be not much different in the thermally cycled materials. According to the law of mixtures [20, 78, 79, 80, 81], the total strength of dual-phase steels can be given as:

$$\text{Total strength} = V_f S_f + V_m S_m$$

where  $V_f$  = volume percent ferrite  
 $V_m$  = volume percent martensite  
 $S_f$  = strength of ferrite  
 and  $S_m$  = strength of martensite.

From Table 4.3 it is seen that with higher number of cycles,  $V_m$  becomes lower. The strength of martensite is dependent mostly on the carbon content, not anything else. So the strength of martensite ( $S_m$ ) remains practically unchanged. With increase in the number of cycles, in case of Type-I thermal-cyclic treatment, the volume fraction of martensite ( $V_m$ ) (Table 4.3) decreases while the strength of ferrite increases.

So increase in  $V_f S_f$  components is compensated by the decrease in  $V_m S_m$  components. But as stated earlier, in case of materials obtained by Type-II thermal-cyclic treatment the increase in the number of cycles makes the ferrite weaker. Also, the martensite volume percent in this case is found to be high (Table 4.1). Hence, in this case also, the decrease in  $V_f S_f$  components is compensated by the increase in  $V_m S_m$  components.

Thus not much change is seen in case of the U.T.S. values of the thermally cycled structures.

The volume percent of martensite in all the thermally cycled samples is within a maximum of ~25%. The remaining amount (i.e. >75%) is the soft ferrite constituent. Moreover, the martensite is arranged in the form of small globules. Not only that, the interface between the martensite and ferrite is coherent [50, 77]. Therefore, it is easy to understand that such a material should have a sufficiently high elongation since both the soft and the hard constituents can deform in a continuous manner giving rise to a high elongation value.

The reasonably high ductility of these thermally cycled materials is also reflected in their corresponding fractographs which are typical of ductile materials.

Texture results show clearly that the thermal-cycling process does not lead to any special crystallographic arrangement of the grains. Rather, it can be safely said that the texture remains almost unchanged from that of the initial cold-rolled material and, overall, it's intensity is low. The very fact that even after a large number of cycles the texture does not change, may mean that there is some kind of a texture memory effect in this material. That is, the material seems to remember it's original texture and retains the same even after repeated number of cycles. Such texture memory effects have also been found in other steels. The similarity in the textures of the thermally cycled (and therefore, recrystallized) materials

and the cold-deformed initial material also suggests that recrystallization of the structures takes place essentially by an in-situ mechanism whereby strain-free grains form from deformed regions of the same or nearly the same orientations.

## CHAPTER VI

### Conclusions

1. Among the Type-I and Type-II thermal-cycling treatments given, Type-I thermal-cycling treatment leads to a better refining of the grain size.
2. The initial starting material obtained by subjecting the 60% cold-deformed material to intercritical annealing at  $810^{\circ}\text{C}$  for 5 minutes responds most favourably towards grain refinement.
3. A total of ten cycles of the Type-I treatment gives the best results of grain refinement.
4. U.T.S. and percentage elongation are seen to be more or less same for all the thermally cycled materials irrespective of the nature of initial starting material, the type of cycle and the number of cycles.
5. Increasing number of cycles lead to a higher 'n'-value in materials subjected to Type-I thermal-cycling treatment.
6. The fracture of the thermally cycled materials is found to be mainly ductile in nature.
7. The texture of the cold-worked materials is found to possess the two weak components  $\{111\} \langle 112 \rangle$  and  $\{111\} \langle 110 \rangle$ . However, the general intensity of the texture is rather low.
8. There is essentially no difference in texture as a function of the type of thermal-cycling performed.

9. Similarity of textures of the thermally cycled and cold-deformed initial materials also suggest that recrystallization of the structures takes place essentially by an in-situ mechanism whereby strain-free grains form from deformed regions of the same or nearly same orientations.
10. The material, on thermal-cycling by either of the cycles, seem to possess some kind of texture memory.

## References

1. S. Hayami and T. Furukawa: Microalloying '75, 1, 78 (1977) New York, Union Carbide Corp.
2. R.K. Ray: J. Mat. Sci. Lett., 4 (1985) 67.
3. D.K. Mondal: Ph.D. Thesis, Dept. of Metallurgical Engg., I.I.T., Kanpur, India, 1987.
4. R.A. Grange: Trans. Am. Soc. Metals, 59 (1966) 26.
5. F.B. Pickering: Microalloying '75, 1 (1977) 3.
6. T. Gladman, O. David and I.D. McIvor: Microalloying '75, 1 (1977) 25.
7. D.J. Bailey and R. Stevenson: Metall. Trans. A, 10A (1979) 47.
8. R. Stevenson, D.J. Bailey and G. Thomas: *ibid*, 57.
9. M.S. Radhid: SAE Preprint 770211 (1977).
10. J.W. Morrow, A.P. Coldren and G. Tither: Climax Molybdenum Co., Reports L-176-165, L-176-166 (1976).
11. M.S. Rashid: SAE Paper 760206 (1976) and General Motors Research Publications Nos. GMR 2044, 2326, 2413, 2647.
12. J.W. Morrow and G. Tither: J. Met., 12 (1978) 20.
13. T. Matsouka and K. Yamamori: Metall. Trans., 6A (1975) 1613.
14. R.A. Grange: Metall. Trans., 2 (1971) 65.
15. J.Y. Koo and G. Thomas: Mat. Sci. and Engg., 24 (1976) 187.
16. J.Y. Koo and G. Thomas: Metall. Trans. A, 8A (1977) 525.
17. J.Y. Koo and G. Thomas: Scripta Met., 13 (1979) 1141.
18. R.G. Davies: Metall. Trans. A, 9A (1978) 41.
19. R.G. Davies: Metall. Trans. A, 9A (1978) 451.
20. R.G. Davies: Metall. Trans. A, 9A (1978) 671.
21. R.G. Davies: Metall. Trans. A, 10A (1979) 113.

22. R.G. Davies: Metall. Trans. A, 10A (1979) 1549.
23. A.P. Coldren and G. Tither: J. Met., 4 (1978) 6.
24. T. Furukawa, H. Morikawa, H. Takechi and Koyama: 'Process Factors for Highly Ductile Dual-Phase Sheet Steels', Report from Research Lab., Nippon Steel Corp., Kawasaki, Japan.
25. E.C. Bain and H.W. Panton: 'Alloying Elements in Steels', 2nd Ed., ASM, Ohio (1966).
26. P.R. Mould and C.C. Skena: 'Formable HSLA and Dual-Phase Steels' (A.T. Davenport, Ed.), AIME, New York (1977) 181.
27. R.G. Davies: *ibid*, 25.
28. G.F. Bolling and R.H. Richman: Canadian J. Phys., 45 (1967) 541.
29. H. Masui and H. Takechi: Trans. ISIJ, 16 (1976) 69.
30. P.M. Kelly and J. Nutting: JISI, 197 (1961) 199.
31. G.R. Speich and R.C. Miller: 'Structure and Properties of Dual-Phase Steels' (R.A. Kot and J.W. Morris, Eds.), AIME, New York (1979) 145.
32. J.H. Bucher and E.G. Hamburg: SAE Paper 770164 (1977).
33. T. Tanaka, M. Nishida, K. Hashiguchi and T. Kato: 'Structure and Properties of Dual-Phase Steels' (R.A. Kot and J.W. Morris, Eds.), AIME, New York (1979) 221.
34. W.C. Leslie: Metall: Trans. A, 3 (1973) 5.
35. S. Takeuchi, T. Taoka and H. Yoshida: Trans. ISIJ, 9 (1969) 105.
36. A.P. Coldren, G. Tither, A. Conford and J.R. Hiam: 'Formable HSLA and Dual-Phase Steels' (A.T. Davenport, Ed.), AIME, New York (1977) 205.
37. K.W. Andrews: J. Iron Steel Inst., London, 203 (1965) 721.
38. N.J. Kim and G. Thomas: Metall. Trans. A, 12A (1981) 483.
39. J.M. Rigsbee and P.J. Van der Arend: 'Formable HSLA and Dual-Phase Steels' (A.T. Davenport, Ed.), AIME, New York (1977) 56.
40. A.R. Marder: Same as Ref. 36, 87.

41. M.S. Rashid: 'Formable HSLA and Dual-Phase Steels' (A.T. Davenport, Ed.), AIME, New York (1977) 1.
42. J.H. Hollomon: Trans. AIME, 162 (1945) 268.
43. I.L. Dillamore, K.I. Nam and M.B.O.O. Shitta: 3rd Congresso Brasileiro de Engenharia e Ciéneia dos Materials, Dec. (1978).
44. D.A. Kozakwa, R.D. Lawson, D.K. Matlock and G. Krauss: Scripta Met., 14 (1980) 1023.
45. C. Crussard: Rev. Met., Paris, France, 10 (1953) 697.
46. B. Jaoult: J. Mech. and Phys. Solids, 5 (1957) 95.
47. P. Ludwik: Elements der Technologischem Mechanik, Julius Springer, Berlin (1909) 32.
48. R.G. Davies and C.L. Magee: 'Structure and Properties of Dual-Phase Steels' (R.A. Kot and J.W. Morris, Eds.), AIME, New York (1979) 1.
49. R.G. Davies and C.L. Magee: Vanitec Seminar on Vanadium Cold Pressing and Dual-Phase Steels, Oct. (1978), W. Berlin, Germany.
50. S.T. Mileiko: J. Mat. Sci., 4 (1969) 974.
51. P. Öström and I. Lindgren: Swedish Inst. for Metals Research, IM-1308, Aug. (1978).
52. P. Öström: Metall. Trans. A, 12A (1981) 355.
53. H. Fischmeister and B. Karlsson: Z. Metllk., 68 (1977) 311.
54. P. Uggowitzer and H.P. Stuwe: Mat. Sci. and Engg., 55 (1982) 181.
55. Y. Tomota, H. Yoshino and K. Kuroki: Scripta Met., 11 (1977) 853.
56. R.K. Ray: Scripta Met., 18 (1984) 1205.
57. R.L. Whiteley: Trans. ASM, 52 (1960) 154.
58. R.L. Whiteley, D.E. Wise and D.J. Blickwede: Sheet Met. Ind., 38 (1961) 349.
59. M.B.O.O. Shitta: Ph.D. Thesis, Univ. of Aston, Birmingham (1981).
60. H. Hu: Metall. Trans. A, 13A (1982) 1257.



61. K. Kwi-hara, Y. Hosoya and K. Nakaoka: Proc. 6th Int. Conf. 'Texture of Materials', Tokyo (1981).
62. S.S. D'yachenko, A.A. Movlyan and A.I. Polyonichka: Steel USSR, 9 (1987) 433.
63. B.F. Decker, E.T. Asp and D. Harker: J. Appl. Phys., 19 (1948) 388.
64. L.G. Schulz: J. Appl. Phys., 20 (1949) 1030.
65. R.K. Ray: Scripta Met., 11 (1984) 1211.
66. H.J. Bunge, C.M. Vlad and H. Kopp: Archiv für Eisenhüttenwesen, 55 (1984) 163.
67. R.K. Ray: Proc. 13th Biennial Cong. of I.D.D.R.G., Melbourne (1984) 263.
68. R.K. Ray: Proc. 14th Biennial Cong. of I.D.D.R.G., Köln (1986) 383.
69. R.L. Lawson, D.K. Matlock and C. Krauss: Metallography, 13 (1980) 71.
70. B.D. Cullity: 'Elements of X-ray Diffraction', 2nd Ed., Addison-Wesley Pub. Co., Inc. (1978) 308.
71. R. Alam, H.D. Mengelberg and K. Lücke: Z. Metallk., 58 (1967) 867.
72. U. Kobbe and H. Schuon: Siemens Z., 47 (1973) 119.
73. R.J. Roe: J. Appl. Phys., 6 (1965) 2024.
74. R.J. Roe: J. Appl. Phys., 37 (1966) 2069.
75. H.J. Bunge: Mathematische Methoden der Texturanalyse, Akademieverlag, Berlin (1969).
76. H.J. Bunge: Z. Metallk., 56 (1965) 872.
77. G. Garmon and R.B. Thompson: Metall. Trans. A, 4A (1973) 863.
78. G.R. Speich and R.L. Miller: 'Structure and Properties of Dual-Phase Steels' (R.A. Kot and J.W. Morris, Eds.), AIME, New York (1979) 145.
79. W.R. Cribb and J.M. Rigsbee: ibid, 91.
80. R. Priestner and C.L. Aw: Scripta Met., 18 (1984) 133.

81. A.R. Marder: Metall. Trans. A, 13A (1982) 85.
82. J. Hansen, J. Pospiech and K. Lücke: 'Tables for Texture Analysis of Cubic Crystals', Springer-Verlag, Berlin-Heidelberg (Germany) 1978.

**A**110760

ME-1881-M-KAR-EFF